Deformation bands in porous sandstones

their microstructure and petrophysical properties

Anita Torabi

Dissertation for the degree Philosophiae Doctor (PhD)

Department of Earth Science

University of Bergen

2008

Contents

Preface

The work presented in this dissertation was carried out in my PhD project. The project started in April 2005 at the Centre for Integrated Petroleum Research (CIPR), Department of Earth Science; University of Bergen (UiB). My PhD project has been a part of the "Fault Facies" project at CIPR. The Fault Facies project is a multi-disciplinary petroleum research project which aims to improve the implementation of faults in 3D geological reservoir models. The project has several different themes, one of which is focused on the micro-scale deformation structures known as deformation bands, which form during the process of fault initiation and also damage-zone development. This theme was developed in my PhD project, where the main concern was to increase our understanding of the microstructure and petrophysical properties of deformation bands and to investigate their effect on petrophysical characteristics of sandstone reservoirs.

This dissertation comprises four separate and complementary parts:

Part one (Introduction): This part describes the "state of the art" for deformation bands and their development, states the objectives of the research I conducted , and describes the relation between the four scientific papers that make up the main body of the thesis.

Part two (papers): The second part, which is the main outcome of my study, is a collection of four research papers, of which the first has already been published, and the second has been accepted for publication and the third is in review in an international journal. The fourth paper will soon be submitted.

The four papers included are:

Paper 1: Torabi A., Braathen, A., Cuisiat, F., and Fossen, H., 2007. Shear zones in porous sand: Insights from ring-shear experiments and naturally deformed sandstones. Tectonophysics, 437, 37-50.

This paper presents an analysis of analogue experimental modeling of shear zones based on original ring-shear experiments. It includes microscopic study of both experimental shear zones and natural deformation bands. The result of this study was also presented in Petroleum Geoscience Collaboration Conference, 24th -25th October 2006, The Geological Society, Burlington House, London.

Paper 2: Rotevatn, A., Torabi, A., Fossen, H., and Braathen, A., 2007. Slipped deformation bands: a new type of cataclastic deformation bands in Western Sinai, Suez Rift, Egypt. Accepted, Journal of Structural Geology.
The second paper describes a new type of cataclastic deformation band. This study reports original field outcrop study, optical microscopy and laboratory measurements.

Paper 3: Torabi, A., Fossen, H., and Alaei, B., 2007. Application of spatial correlation functions in permeability estimation of small-scale deformation bands in porous rocks. In review, Journal of Geophysical Research (Solid Earth).

Paper 4: Torabi, A., and Fossen, H., 2007. Spatial variation of microstructure and petrophysical properties of deformation bands. To be submitted to Journal of Structural Geology.
The third and the fourth papers comprise a detailed study of the microstructure of all types of deformation bands and an estimation of their petrophysical properties using an image processing method developed through this study. These works were presented in Winter Conference, 8^{th} -10^{th} January 2007, Stavanger, Organized by Geological Society of Norway, and also in StatoilHydro International Student Conference, 9^{th} – 13^{th} October 2007, StatoilHydro Research Center, Trondheim, Norway.

Part three (Synthesis): This part provides a synthesis of the results obtained at different parts of the study. It includes a brief discussion, and also addresses limitations of the different approaches applied in the conducted research. Some suggestions for future work are also included in this part.

Part four (Appendix): The last part contains the MATLAB program that was written to calculate the one- and two-point spatial correlation functions and specific surface area of the pore-grain interface from backscatter images of faulted sandstones.

Anita Torabi
December, 2007

Acknowledgements

My PhD project was a part of a larger CIPR research initiative called “Fault Facies” which was financed by the Norwegian Research Council (NRC), Statoil (now StatoilHydro) and Conoco-Philips. I would like to express my gratitude to all of my supervisors: Alvar Braathen for his encouragement and scientific discussions, and Arne Skauge, William Helland-Hansen and Fabrice Cuisiat for their support and useful comments. I would especially like to thank Haakon Fossen for his continuous guidance and generosity. His motivating comments and inspiration was crucial during my PhD project. I would also like to thank Egil Sev. Erichsen for his assistance with the Scanning Electrone Microscope. Jan Tveranger is acknowledged for sharing his knowledge and experience. I would like to thank Tore Skar for good collaboration during working at CIPR and also for his encouragement. Walter Wheeler is also appreciated for reviewing the introduction and synthesis parts of this dissertation. I would like to take the opportunity to express my appreciation to the administrations at the Earth Science Department and CIPR. Special thanks to Irene Huse who was always helpful when, in several crucial moments in my study, I was beset with computer-related problems. I am grateful to many friends and colleagues. I am indebted to my husband Behzad Alaei who has always been supportive and sympathetic and to my two lovely and intelligent children, my son Armin and my daughter Arezo, who were supportive and patient enough to tolerate the hard life of having a PhD student as mother. They sometimes participated in the scientific discussions at home and now after almost 3 years, they know these tiny, neat phenomena known as deformation bands very well. I would like to dedicate my thesis to my family for their love and support.

Abstract

Deformation bands are commonly thin tabular zones of crushed or reorganized grains that form in highly porous rocks and sediments. Unlike a fault, typically the slip is negligible in deformation bands. In this dissertation the microstructure and petrophysical properties of deformation bands have been investigated through microscopy and numerical analysis of experimental and natural examples. The experimental work consists of a series of ring-shear experiments performed on porous sand at 5 and 20 MPa normal stresses and followed by microscopic examination of thin sections from the sheared samples. The results of the ring-shear experiments and comparison of them to natural deformation bands reveals that burial depth (level of normal stress in the experiments) and the amount of shear displacement during deformation are the two significant factors influencing the mode in which grains break and the type of shear zone that forms. Two end-member types of experimental shear zones were identified: (a) Shear zones with diffuse boundaries, which formed at low levels of normal stress and/or shear displacement; and (b) Shear zones with sharp boundaries, which formed at higher levels of normal stress and/or shear displacement. Our interpretation is that with increasing burial depth (approximately more than one kilometer, simulated in the experiments by higher levels of normal stress), the predominant mode of grain fracturing changes from flaking to splitting; which facilitates the formation of sharp-boundary shear zones. This change to grain splitting increases the power law dimension of the grain size distribution (D is about 1.5 in sharp boundary shear zones). Based on our observations, initial grain size has no influence in the deformation behavior of the sand at 5 MPa normal stresses.

A new type of cataclastic deformation band is described through outcrop and microscopic studies; here termed a "slipped deformation band". Whereas previously-reported cataclastic deformation bands are characterized by strain hardening, these new bands feature a central slip surface, which indicates late strain softening. They lack the characteristic compaction envelop, and are typified by higher porosity and lower permeability than previously-described cataclastic deformation bands. Intense background fracturing of the host rock and significant initial porosity are considered to be important in creating these newly-discovered deformation bands.

In a related study, we investigate, for millimeter- wide deformation bands, the scale limitation inherent in laboratory measurements of porosity and permeability. The scale

limitations imposed by the deformation band relative to the physical sample size motivated us to develop a new method for determining porosity and permeability based on image processing. While plug measurements measure the effective permeability across a 25.4 mm (1 inch) long sample, which includes both host rock and deformation band, the method presented here provides a means to estimate porosity and permeability of deformation band on microscale. This method utilizes low-order (one- and two-orders) spatial correlation functions to analyze high-resolution, high-magnification backscatter images, to estimate the porosity and specific surface area of the pore-grain interface in the deformed sandstones. Further, this work demonstrates the use of a modified version of the Kozeny-Carmen relation to calculate permeability by using porosity and specific surface area obtained through the image processing. The result shows that permeability difference between the band and the host rock is up to four orders of magnitude. Moreover, the porosities and permeabilities estimated from image processing are lower than those obtained from their plug measurements; hence the traditional laboratory measurements have been overestimating permeability because of the previously-unrecognized scale problem. In addition, the image processing results clearly show that, as a result of microstructural variation, both porosity and permeability vary along the length of individual deformation bands, with permeability variations of up to two orders of magnitude. Such petrophysical variations are found in several types of deformation bands (disaggregation, cataclastic and dissolution bands), but the range depends on the deformation mechanisms, in particular on the degree of (i) cataclasis, (ii) dissolution in cataclastic and dissolution bands, and (iii) on the phyllosilicate content in disaggregation bands. This microscopic anisotropy in the petrophysical properties of deformation bands opens up a new and fruitful area for further research. Our results show that for phyllosilicate bands the band thickness is related to the phyllosilicate content, whereas for cataclastic bands no apparent correlation was found between thickness and intensity of cataclasis.

Introduction

Sedimentary rocks, whether they are water aquifer or petroleum reservoirs are characterized by features which affect the fluid flow. The faulting of clastic rocks can induce large- and small-scale heterogeneities in the spatial distribution of petrophysical characteristics, particularly porosity and permeability. Enhanced understanding of the structure and the petrophysical properties of fault zones in comparison to the surrounding undeformed host rock is essential when efforts are made to predict fluid flow through faulted reservoirs.

Many workers have provided a theoretical foundation for understanding the movement of fluids, especially hydrocarbons, in the subsurface (e.g. Hubbert, 1953; Berg, 1975; Schowalter, 1979; England, 1987; Watts, 1987). However, applying such studies to the movement of hydrocarbons within faulted reservoirs has been limited by the absence of detailed data on the petrophysical properties of fault rocks (e.g. porosity and permeability), as well as the distribution of fault-related deformation structures (e.g. Fisher et al., 2001). Recent publications have provided quantitative data on the petrophysical properties of faults and their associated localized microstructures, known as deformation bands (e.g. Antonellini and Aydin, 1994; Fisher and Knipe, 1998; Gibson, 1998, Fisher and Knipe, 2001; Hesthammer and Fossen, 2001; Ogilvie and Glover, 2001; Shipton, et al., 2002), the distribution of fault related structures (e.g. Allan, 1989; Knipe, 1997; Yielding et al., 1997; Shipton et al., 2001), as well as the fault zone structures in both macro- and microscale (e.g. Cowie and Scholz, 1992; Gibson, 1994; Peacock and Sanderson, 1994; McGrath and Davison, 1995; Knipe et al., 1997; Fossen et al., 2007).

Although such data are required as input to reservoir simulators, large uncertainties exist in the detail of the associated structures in the fault zones and absolute values of properties; these uncertainties ultimately have large influence on the predicted fluid flow. The main aim of the studies in this dissertation is to improve our knowledge of deformation bands and their petrophysical properties such as porosity and permeability. As a complete review of the existing literature is provided through the enclosed papers, the following section is a brief overview of the state of the art for the studied topic.

Deformation bands and their petrophysical properties

Deformation bands are tabular, thin structures, which form at the onset of strain localization in porous rocks (e.g. Rudnicki and Rice, 1975, Bésuelle, 2001a; Klein et al., 2001; Rudnicki, 2002; Olsson et al., 2002, Rudnicki, 2004; Schultz and Siddharthan, 2005, Aydin et al., 2006; Fossen et al., 2007, Holcomb et al., 2007, Fig. 1) . They are preferentially oriented with respect to the stress field (Bésuelle, 2001). Deformation bands are different from faults and fractures in that they do not feature a discrete fracture or slip surface (e.g. Fossen et al., 2007).

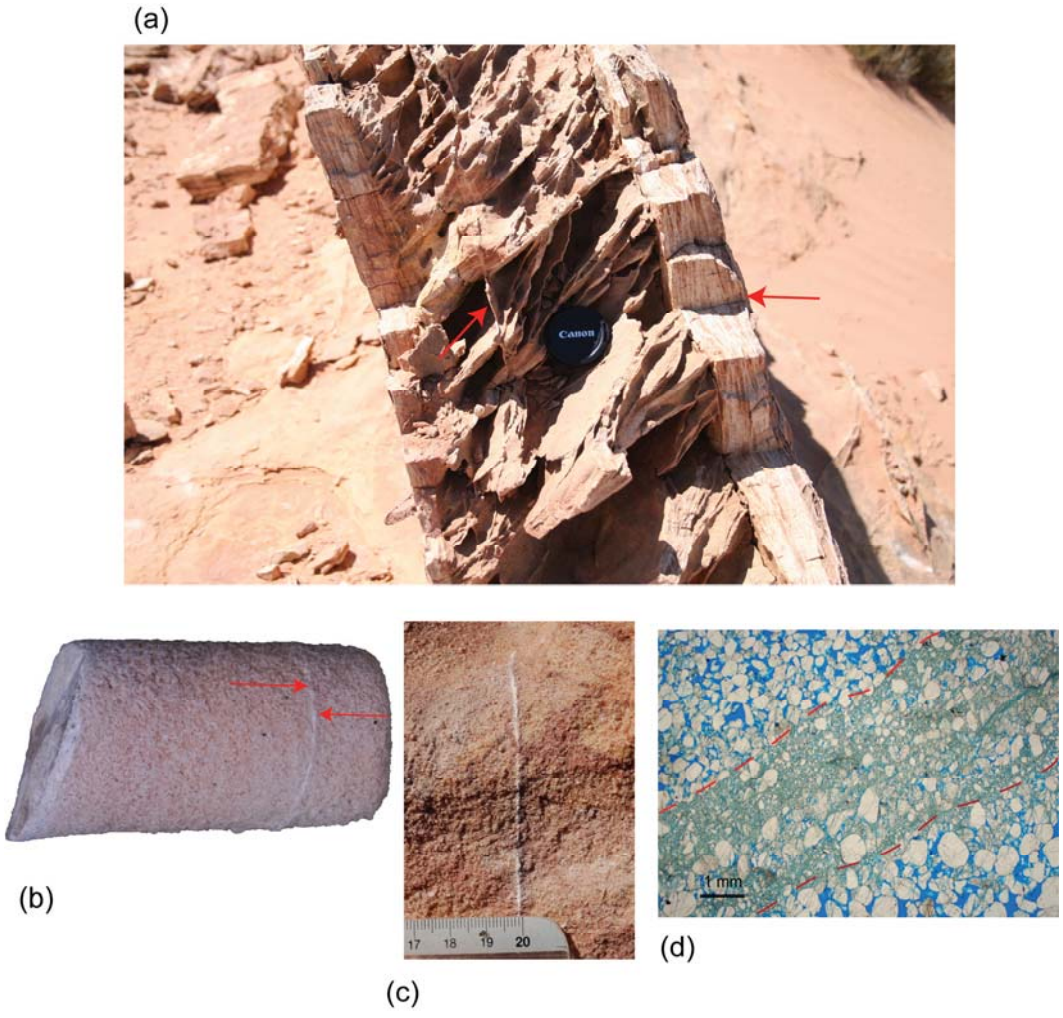

Fig.1. Deformation bands at different scales: (a) Deformation bands(marked by the arrows), outcrop photo (lens-cap for scale) ; (b) A millimeter wide deformation band (marked by the arrows) in a cylindrical plug of sandstone (length of the plug is 25.4 mm/ 1 inch); (c) A millimeter wide deformation band in a hand sample, the scale bar is in centimeters (d) photomicrograph of a deformation band outlined with red dashed lines, quartz grains are white, epoxy saturating the pore space is blue.

Field and laboratory observation show that they are not necessarily associated with a dilational strain. Very often they show porosity reduction (Bésuelle, 2001). Deformation bands range from compactional through simple shear to dilational (e.g. Anttonellini and Aydin, 1994; Antonelli et al., 1994; Mollema and Antonellini, 1996, Cashman and Cashman, 2000; Du Bernard et al., 2002) and involve different deformation mechanisms including particulate (granular) flow, cataclasis and dissolution (e.g. Gibson, 1994; Rawling and Goodwin, 2003; Fossen et al, 2007, Fig. 2). Disaggregation bands form as result of granular flow and involve rolling, sliding and reorganization of the sand grains in sand or sandstones at shallow depth or low effective stress (e. g. Rawling and Goodwin, 2003). Disaggregation bands (Fig. 2a) do not affect the petrophysical properties of the deformed sandstone significantly. Cataclastic deformation bands (Fig. 2c) are characterized by grain abrasion, crushing or cataclasis and can reduce porosity and permeability of deformed sandstones significantly (Antonellini and Aydin, 1994). Dissolution and cementation bands form where dissolution or cementation is dominant (Fig. 2d). Dissolution and quartz cementation have been suggested as an explanation for poor reservoir performance in North Sea reservoirs located at >3 km depth (Hesthammer et al., 2002).

Typical deformation bands such as those first reported by Aydin (1978) in Utah, are about a millimeter thick, several meters to hundreds of meters in length and have maximum displacements in the range of several millimeters to several centimeters. These bands consist of two zones, namely inner zone and outer zone. The inner zone comprises a zone of fractured and crushed grains, whereas the deformation in outer zone was restricted to reorganization of the grains and pore collapse (Aydin, 1978; Aydin and Johnson, 1978).

The Localization and development of deformation bands and the evolution of their permeability structure have been investigated through experimental work (e.g. Mair et al., 2000; Main et al., 2001; Lothe et al., 2002; Ngwenya, et al., 2003). In the course of deformation mechanism in porous sand and sandstone, controlling factors have been conveniently isolated and studied in the laboratory. Such studies have attracted significant attention from geologists, rock- and soil-mechanics engineers, and geophysicists (Mandl et al., 1977; Zhu and Wong, 1997; Zhang and Tullis, 1998; Main et al., 2001; Mair et al., 2000; 2002; Sperrevik et al., 2002; Lothe et al., 2002; Garga and Sendano, 2002; Clausen and Gabrielsen, 2002; Kjelstad et al., 2002; Ngwenya et al., 2003; Agung et al., 2004; Sassa et al., 2004). Numerical modeling of deformation bands

has also provided valuable insights (e.g. Antonellini et al., 1995; Wang et al., 2001; Borja, 2003; Narteau and Main, 2003; Schultz & Balasko, 2003; Okubo and Schultz, 2005).

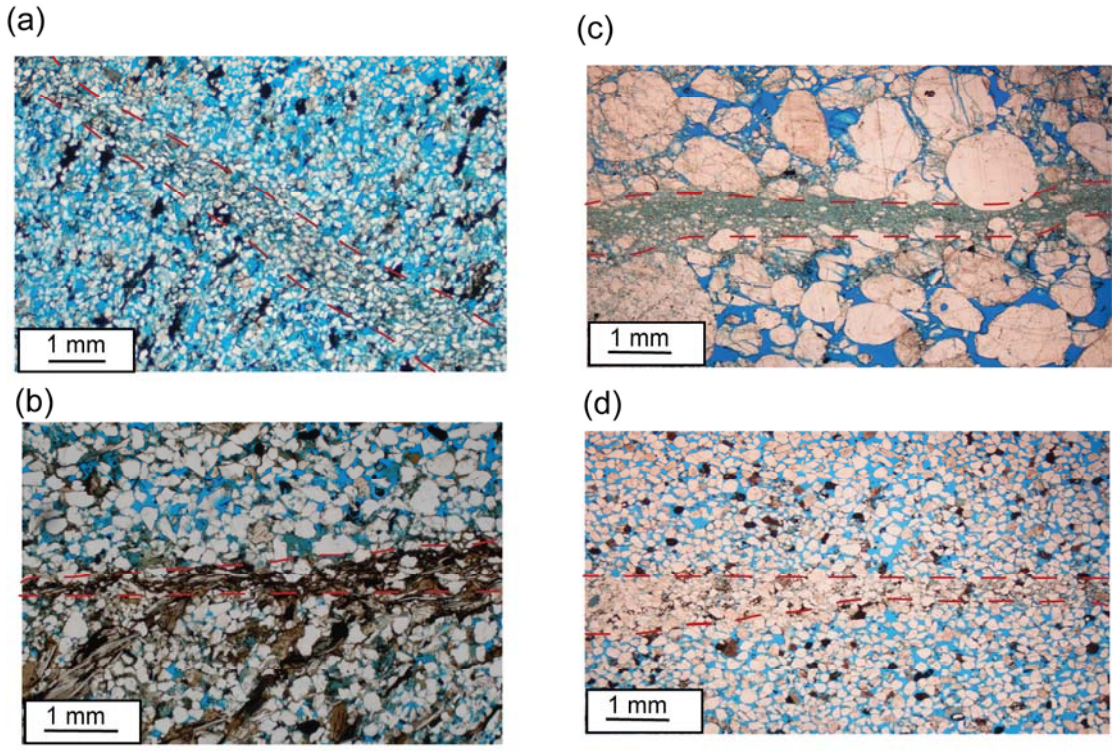

Fig.2. Examples of deformation bands formed as results of different deformation mechanisms; (a) A disaggregation band from Gullfaks field, North Sea(b) A phyllosilicate band from Huldra field, North Sea (c)A cataclastic band from Sinai, Egypt (d) A dissolution band from San Rafael Desert,Utah.

Several publications address the effects of the small-scale geological features on large-scale permeability of the reservoirs (e.g. Durlofsky, 1992; Jourde, 2002; Sternlof et al., 2004). For more than two decades, much attention has been devoted to the petrophysical properties of deformation bands, in particular permeability reduction caused by the presence of deformation bands in faulted sandstones (Pitman, 1981; Jamison and Streans, 1982; Antonellini and Aydin, 1994; Knipe et al., 1997; Gibson, 1998; Fisher and Knipe, 2001; Ogilvie and Glover, 2001; Shipton et al., 2002; Sternlof et al., 2004). Individual cataclastic deformation bands in Utah are reported to reduce the porosity of the host sandstone by one order of magnitude and the permeability by three orders of magnitude (Antonellini and Aydin, 1994).

Phyllosilicate bands (Fig. 2b), which form by granular flow in sandstones containing more than 10-15% phyllosilicate, involve up to several orders of reduction in permeability according to plug measurements reported by Fisher and Knipe (2001). However, the dispersion in the reported porosity and permeability data for deformation bands is noticeable. Moreover, spatial variations in porosity and permeability, related to microstructural variations along individual deformation bands, have been given little or no attention in the literature (cf. Fossen and Bale, 2007).

In addition, most of the published porosity and permeability data for deformation bands are from either mini-permeameter or plug measurements. A central question is whether these data are representative of the permeability effects of millimeter wide deformation bands? What kinds of uncertainties are associated with these methods? There has been significant progress in numerical permeability models for sandstone reservoirs, one could ask whether existing image processing based methods typically applied to undeformed sandstones (e.g. Ehrlich et al., 1984; Wissler, 1987; Koplik et al., 1984; Doyen, 1988; Blair et al., 1996, Bakke and Øren, 1997; Keehm et al., 2004; 2006; White et al., 2006) could be used to estimate the porosity and permeability of deformation bands?

Objectives of this study

The prediction of fluid flow paths in deformed porous sandstone requires more accurate geological models of deformation band morphology, and their evolution. The studies collected in this dissertation share the common aim of increasing our understanding of the detailed microstructure and petrophysical properties of deformation bands with special reference to deformation bands formed in extensional geological settings, in particular rift related structures similar to the North Sea. In order to achieve this goal a three-part workflow was defined.

1- Analogue modeling of deformation bands by ring-shear experiments (Paper 1). In the ring-shear project, we aimed to investigate the initiation and development of shear zones in highly porous sand at different stress levels. The effect of grain size on deformation process was also studied. Fundamental for this study was the creation of shear zones which are similar to natural deformation bands formed at shallow to medium burial depth.

2- Outcrop study; an outcome of this work was establishing a database on thin sections of different types of deformation bands. Our database involves examples from Corsica (France), Sinai (Egypt), Utah (USA). The main focus was to present a new type of deformation band, first observed by us during the field and laboratory works on samples from Sinai, Egypt (Paper 2). These bands are distinct from other deformation bands in our database. The work examines the microstructure and petrophysical properties of this new band type and discusses mechanisms and causes for their formation.

3- Numerical analysis of the petrophysical properties of deformation bands and their host rock, such as porosity and permeability (Papers 3 and 4); the main concern for this part was to find a reasonably accurate method to estimate the porosity and permeability of deformation bands. Furthermore we sought to explain the wide dispersion in the published petrophysical properties of deformation bands. Examples of different types of deformation bands from localities around the world were examined using optical microscopy, Secondary Electron Microscope and image processing.

References

Agung, M. W., Sassa, K., Fukuoka, H., Wang, G., 2004. Evolution of shear-zone structure in undrained ring-shear tests. Landslides 1, 101-112.

Allan, U. S., 1989. Model for hydrocarbon migration and entrapment within faulted structures. AAPG Bulletin, 73, 803-811.

Antonellini, M. and Aydin, A., 1994. Effect of faulting on fluid flow in porous sandstones: petrophysical properties, AAPG Bulletin, 78, 355-377.

Antonellini, M.A., Aydin, A. & Pollard, D. D., 1994. Microstructure of deformation bands in porous sandstones at Arches National Park, Utah. Journal of Structural Geology, 16, 941–959.

Antonellini, M. and Pollard, D., 1995. Distinct element modelling of deformation bands in sandstone, Journal of Structural Geology, 17, 8, 1165-1182.

Aydin, A., 1978. Small faults formed as deformation bands in sandstone. Pure and applied Geophysics 116: 913-913.

Aydin, A., Johnson, A. M., 1978. Development of faults as zones of deformation bands and as slip surfaces in sandstone. PAGEOPH 116.

Aydin, A., Borja, R. I. and Eichhubl, P., 2006.Geological and Mathematical framework for failure modes in granular rock. Journal of Structural Geology, 28, 83-98.

Bakke, S. and Øren, P. E., 1997. 3-D Pore-scale modelling of sandstones and flow simulations in the pore networks, SPE 35479, 2.

Berg, R. R. (1975). Capillary entry pressure in stratigraphic traps. AAPG Bulletin, 59, 939-956.

Blair, S. C., Berge, P. A., and Berryman, J. G., 1996. Using two-point correlation functions to characterize microgeometry and estimate permeabilities of sandstones and porous glass, J. Geophys. Res., 101(B9), 20359-20375.

Borja, R. I., 2003. Computational modelling of deformation bands in granular media. II. Numerical Simulatiions, Comput. Methods Appl. Mech. Engreg. 193, 2699-2718.

Bésuelle, 2001. Compacting and dilating shear bands in porous rocks: Theoretical and experimental conditions, Journal of Geophysical Research, Vol. 106, No.87, P. 13,435-13,442.

Cashman, S. & Cashman, K., 2000. Cataclasis and deformation-band formation in unconsolidated marine terrace sand, Humboldt County, California. Geology,28, 111–114.

Clausen, J. A., Gabrielsen, R. H., 2002. Parameters that control the development of clay smear at low stress states: an experimental study using ring-shear apparatus. Journal of Structural Geology 24(10), 1569-1586.

Cowie, P.A. & Scholz, C.H., 1992. Displacement–length scaling relationship for faults: data synthesis and analysis. Journal of Structural Geology, 14, 1149–1156.

Doyen, P. M., 1988. Permeability, conductivity, and pore geometry of sandstone, J. Geophys. Res., 93, 7729-7740.

Du Bernard, X. D., Eichhubl, P., and Aydin, A., 2002. Dilation bands: A new form of localized failure in granular media, Geophysical Research Letters 29(24), 2176.

Ehrlich R., Kennedy, S. K., Crabtree, S. J. and Cannon, R. L., 1984. Petrographic image anlysis: I. Analysis of reservoir pore complexes, Journal of Sedimentary Petrology, 54, 1515-1522.

England, W.A., MacKenzie, A.S., Mann, D.M., Quigley, T.M., 1987. The movement and entrapment of petroleum fluids in the subsurface. Journal of the Geological Society, 144, 327– 347.

Fisher, Q. J., & Knipe, R. J., 1998. Microstructural controls on the petrophysical properties of fault rocks. In G. Jones, Q. J. Fisher & R. J. Knipe, Faulting and fault

sealing in hydrocarbon reservoirs. Geological Society of London Special Publications 147, 117-135, London; The Geological Society.

Fisher, Q.J., Harris, S. D., McAllister, E., Knipe, R. J., Bolton, A. J., 2001, Marine and Petroleum Geology, 18, 251-257.

Fisher, Q. J. and Knipe, R. J., 2001. The permeability of faults within siliciclastic petroleum reservoirs of the North Sea and Norwegian Continental Shelf, Marine and Petroleum Geology, 18, 1063-1081.

Fossen, H., Schultz, R. A., Shipton, Z., Mair, K., 2007. Deformation bands in sandstone-a review. Journal of the Geological Society, London, 164, 4, 755-769.

Fossen, H & Bale, A. 2007: Deformation bands and their influence on fluid flow. AAPG Bulletin 91, 1685-1700.

Gibson, R.G. 1994. Fault-zone seals in siliciclastic strata of the Columbus Basin, offshore Trinidad. AAPG Bulletin, 78, 1372–1385.

Gibson, R.G. 1998. Physical character and fluid-flow properties of sandstone derived fault zones. In: Coward, M.P., Johnson, H. & Daltaban, T.S. (eds) Structural Geology in Reservoir Characterization. Geological Society, London, Special Publications, 127, 83–97.

Hesthammer, J. and Fossen, H., 2001. Structural core analysis from the Gullfaks area, northern North Sea, Marine and Petroleum Geology 18, 411-439.

Hesthammer, J., Bjorkum, P. A., Watts, L., 2002. The effect of temperature on sealing capacity of faults in sandstone reservoirs: Examples from the Gullfaks and Gullfaks Sør fields, North Sea, AAPG Bulletin.

Holcomb, D., J. W., Rudnicki, K. A., Issen, K., Sternlof, 2007. Compaction localization in the Earth and laboratory: state of the research and research directions, Acta Geotechnica, 2, 1-15.

Hubbert, M. K. (1953). Entrapment of petroleum under hydrodynamic conditions. AAPG Bulletin, 37, 1954-2026.

Jamison, W.R. & Stearns, D.W. 1982. Tectonic deformation of Wingate Sandstone, Colorado National Monument. AAPG Bulletin, 66, 2584–2608.

Jourde, H., Flodin, E. A., Aydin, A., Durlofsky, L. J., and Wen, X-H., 2002. Computing permeability of fault zones in eolian sandstone from outcrop measurements, AAPG Bulletin, 86(7), 1187-1200.

Keehm, Y., Mukerji, T., Nur, A., 2004. Permeability prediction from thin sections: 3D reconstruction and Lttice-Boltzmann flow simulation, Geophys. Res. Let., 31, L04606.

Keehm, Y., Sternlof, K., Mukerji, T., 2006. Computational estimation of compaction band permeability in sandstone, Geosciences Journal, 10, 4, 499-505.

Kjelstad, A., Chuhan, F., Høeg, K., Bjørlykke, K., 2002. Cataclastic shear band formation in sands at high stresses: An analogue experimental model and its relevance for faults in sedimentary basins. PhD Thesis, University of Oslo.

Klein, E., P., Baud, T., Reuschle and T-f., Wong, 2001. Mechanicl behaviour and failure mode of Bentheim Sandstone under triaxial compression, Phys. Chem., Earth (A), Vol. 26, NO. 1-2, pp. 21-25

Knipe, R.J., Fisher, Q.J. & Clennell, M.R. et al. 1997. Fault seal analysis: successful methodologies, application and future directions. In: Møller-Pedersen, P. & Koestler, A.G. (eds) Hydrocarbon Seals: Importance for Exploration and Production. Norwegian Petroleum Society Special Publication, 7, 15–40.

Knipe, R. J., Fisher, Q. J., Jones, G., Clennell, M. B., Farmer, B., Kidd, B., McAllister, E., Porter, J. R., & White, E. A., 1997, Fault seal prediction methodologies, applications and successes. In P. Mùller-Pedersen, & A. G. Koestler (Eds.), Hydrocarbon seals Ð importance for exploration and production. Special Publication NPF, 7, 15-38, Amsterdam; Elsevier.

Koplik, J., Lin, C., Vermette, M., 1984. Conductivity and permeability from microgeometry, J. Appl. Phys., 56, 3127-3131.

Lothe, A. E., Bjørnevoll Hagen, N., Gabrielsen, R. H., Larsen, B.T., 2002. An experimental study of the texture of deformation bands: effects on porosity and permeability of sandstones. Petroleum Geoscience 8, 195-207.

Main, I., Mair, K., Kwon, O., Elphick, S., and Ngwenya, B., 2001. Experimental constraints on the mechanical and hydraulic properties of deformation bands in porous sandstones: a review. In: Holdsworth, R. E, Strachan, R. A., Magloughlin, J. F. and Knipe, R. J. (Eds). The Nature and Tectonic Significance of Fault Zone Weakening. Geological Society, London, Special Publication, 186, 43-63.

Mair, K., Marone, C., 1999. Friction of simulated fault gouge for a wide range of velocities. Journal of Geophysical Research 104(B12), 28,899-28,914.

Mair, K., Main, I. G. and Elphick, S. C., 2000. Sequential growth of deformation bands in the laboratory. Journal of Structural Geology 22, 25-42.

Mair, K., Frye, K. M., Marone, C., 2002. Influence of grain characteristics on the frictioin of granular shear zones. Journal of Geophysical Research 107(B10).

Mandl, G., de Jong L. N., Maltha, A., 1977. Shear zones in granular material. Rock Mechanics. 9, 95-144.

Marone, C., Scholz, C. H, 1989. Particle-size distribution and microstructures within simulated fault gouge. Journal of Structural Geology 11(7), 799-814.

McGrath, A., & Davison, I., 1995. Damage zone geometry around faulttips. Journal of Structural Geology, 17, 1011-1024.

Mollema, P.N. & Antonellini, M.A. 1996. Compaction bands: a structural analogue for anti-mode I cracks in aeolian sandstone. Tectonophysics, 267, 209–228.

Ngwenya, B. T., O. Kwon, et al. (2003). "Permeability evolution during progressive development of deformation bands in porous sandstones. Journal of Geophysical Research 108(B7): 2343 10. 1029/2002JB001854.

Ogilvie, S. R., Glover, Paul, W. J, 2001. The petrophysical properties of deformation bands in relation to their microsturcture. Earth and Planetary Science Letters, 193, 129-142.

Okubo, C. H., Schultz, R. A., 2005. Journal of the Geological Society, London, 162, 939-949.

Olsson, W. A., D. J., Holcomb, J. W. Rudnicki, 2002, Compaction loclization in porous sandstone: implication for reservoir mechanics, Oil & Gas science and Technology, Rev. IFP, Vol., 57, No. 5, pp. 591-599

Peacock, D. C. P., & Sanderson, D. J., 1994. Geometry and development of relay ramps in normal fault systems. American Association of Petroleum Geologists Bulletin, 78, 147-165.

Pittman, E. D., 1981. Effect of fault-related granulation on porosity and permeability of quartz sandstones, Simpson Group (Ordovician) Oklahoma, AAPG Bull., 65, 2381-2387.

Rawling, G. C., Goodwin, L. B., 2003. Cataclasis and particulate flow in faulted, poorly lithified sediments. Journal of Structural Geology 25(3), 317-331.

Rudnicki, J. W., J. R., Rice, 1975, Conditions for the localization of deformation in pressure-sensitive dilatant materials, J. Mech. Phys., Solids, 1975, Vol. 23, pp. 371-394

Rudnicki, J. W., 2002. Condition for compaction and shear bands in a transversely isotropic material, International Journal of Solids and Strcuctures, 39, pp. 3741-3756

Rudnicki, J. W., 2004. Shear and compaction band formation on an elliptic yield cap, Journal of Geophysical Research, Vol. 109

Sassa, K., Fukuoka, H., wang, G., Ishikawa, N., 2004. Undrained dynamic-loading ring-shear apparatus and its applicatiion to landslide dynamics. Lanslides 1, 7-19.

Schowalter, T. T. (1979). Mechanisms of secondary hydrocarbon migration and entrapment. AAPG Bulletin, 63, 723-760.

Schultz, R. A. and Balasko, C. M., 2003. Growth of deformation bands into echelon and ladder geometries, Geophysical Research Letters, 30, 2033.

Schultz, R. A., Siddharthan, R., 2005. A general framework for the occurrence and faulting of deformation bands in porous granular rocks, Tectonophysics, 411, 1-18.

Shipton, Z.K. & Cowie, P.A. 2001. Analysis of three-dimensional damage zone development over _m to km scale range in the high-porosity Navajo sandstone, Utah. Journal of Structural Geology, 23, 1825–1844.

Shipton, Z. K., Evans, J. P., Robeson, K. R., Forster, C: B., Snelgrove, S., 2002. Structural heterogeneity and permeability in eolian sandstone: Implications for subsurface modelling of faults. AAPG Bull. 86 (%), 863-883.

Sperrevik, S., Gillespie, P. A., Fisher, Q. J., Halvorsen, T., Knipe, R. J., 2002. Empirical estimation of fault rock properties. In: Koestler, A. G. and Hunsdale, R. (Eds). Hydrocarbon Seal Quantification. Norwegian Petroleum Society (NPF), Special Publication. 11,109-125.

Sternlof, K. R., Chapin, J. R., Pollard, D. D., and Durlofsky, L. J., 2004. Permeability effects of deformation band in arrays in sandstone. AAPG Bull., 88, 9, 1315-1329.

Watts, N. L. (1987). Theoretical aspects of cap-rock and fault seals for single and two phase hydrocarbon columns. Marine and Petroleum Geology, 18, 4, 274-307.

Wissler, T. M., 1987. Sandstone pore structure: A quantitative analysis of digital SEM images, PhD. thesis, Mass. Inst. of Technol., Cambridge.

White, J., A., Borja, R. I., Fredrich, J. T., 2006. Calculating the effective permeability of sandstone wit multiscale lattice Boltzmann/finite element simulations. Acta Geotechnica, 1, 195-209.

Yielding, G., Freeman, B., & Needham, D. T., 1997. Quantitative fault seal prediction. American Association of Petroleum Geologists Bulletin, 81, 897-917.

Zhang, S., Tullis, T. E., 1998. The effect of fault slip on permeability and permeability anisotropy in quartz gouge. Tectonophysics 295(1-2), 41-52.

Zhu, W., Wong, T., 1997. The transition from brittle faulting to cataclastic flow. Journal of Geophysical Research 102(B2), 3027-3041.

Paper 1

Torabi, A., Braathen, A., Cuisiat, F., and Fossen, H., 2007. Shear zones in porous sand: Insights from ring-shear experiments and naturally deformed sandstones. Tectonophysics, 437, 37-50.

Available online at www.sciencedirect.com
ScienceDirect
Tectonophysics 437 (2007) 37–50
TECTONOPHYSICS
www.elsevier.com/locate/tecto

Shear zones in porous sand: Insights from ring-shear experiments and naturally deformed sandstones

Anita Torabi [a,*], Alvar Braathen [a], Fabrice Cuisiat [b], Haakon Fossen [a]

[a] *Centre for Integrated Petroleum Research, Department of Earth Science, University of Bergen, Post Box 7800, 5020 Bergen, Norway*
[b] *Norwegian Geotechnical Institute, Post Box 3930, N-0806 Oslo, Norway*

Received 20 September 2006; received in revised form 15 February 2007; accepted 27 February 2007
Available online 19 March 2007

Abstract

We have used thin section and particle size analyses to relate stress–strain relationships in ring-shear experiments with burial depth at the time of faulting in naturally deformed samples. We show that the burial depth (level of stress) and the amount of shear displacement at the time of deformation are important factors influencing the type of grain breakage and also the type of shear zone that forms. Further, petrographic image analyses with porosity estimations show systematic change related to progressive development of the shear zones and the development of two end-member types of shear zones: (a) Shear zones with diffuse boundaries formed at low levels of stress, and (b) Shear zones with sharp boundaries formed at higher levels of stress. We consider the mechanism of deformation at shallow depth/low level of stress to be dominated by reorganization, rolling and flaking of grains. This mechanism causes rough surfaces of the grains at the margins and within the shear zones. At greater depths or at higher levels of stress, the predominant mode of fracturing transgresses from flaking to grain splitting, resulting in lower porosity values and greater particle size reduction. Furthermore, this transition results in a slow increase in the power law dimension from 1.4 to 1.6 with respect to the increased displacement.

Keywords: Shear zone; Stress; Strain; Particle size; Porosity; Burial depth

1. Introduction

Zones of localized deformation found in highly porous rocks and sediments, in most cases mechanically stronger and with lower porosity than surrounding rocks, are commonly referred as deformation bands (Aydin et al., 2006; Fossen et al., in press). In this study we investigate a type of deformation band which has a strong component of shear and involves both compaction and shearing of sand and sandstone. Shear deformation is localized to a zone, which we will call a shear zone. It is commonly seen that the petrophysical properties of the rock are changed during the course of the deformation. In particular, the permeability within the shear zone may change dynamically during and after deformation, dependent on many factors. Their occurrence and formation have therefore been the subjects of considerable attention among petroleum and hydro geologists.

Initiation and development of shear zones as deformation structures in highly porous, granular rock are affected by the mechanical and hydraulic properties of the host rock. These properties depend on the microstructural evolution of the rock, in particular the mechanical processes that act during fault formation, how these processes interact, and the stage of evolution

* Corresponding author.
E-mail address: anita.torabi@cipr.uib.no (A. Torabi).

0040-1951/$ - see front matter © 2007 Elsevier B.V. All rights reserved.
doi:10.1016/j.tecto.2007.02.018

(Ngwenya et al., 2003). Outcrop and drill core observations represent only the final results of deformation. Indirect information about the evolution of the structures can be gained by studying natural structures representing various stages of strain. Alternatively, such information can be directly obtained through controlled laboratory experiments performed in a deformation apparatus, such as the ring-shear apparatus.

The mechanism of deformation in porous sand and sandstones is dependent on the initial porosity, grain size, pore fluid pressure, temperature, burial depth, and state of stress and strain throughout the deformation history (Fossen et al., in press). These factors control the type of shear zone that forms and influence its thickness. For example, high porosity and coarse grain size combined with shallow burial depth (low confining pressure) at the time of faulting tend to increase the thickness of shear zones (e.g. Antonellini and Aydin, 1999).

The deformation mechanism controlling factors are conveniently isolated and studied in the laboratory. Hence the advantage of experimental study of shear zones in granular materials is well documented. Such studies have attracted significant attention from geologists, rock and soil mechanics engineers, and geophysicists alike (Mandl et al., 1977; Zhu and Wong, 1997; Zhang and Tullis, 1998; Mair and Main, 2000; Main et al, 2001; Mair et al, 2002; Sperrevik et al., 2002; Lothe et al., 2002; Garga and Sendano, 2002; Clausen and Gabrielsen, 2002; Kjelstad et al., 2002; Ngwenya et al., 2003; Agung et al., 2004; Sassa et al., 2004). Most works are based on triaxial and uniaxial compressional tests. However some of the studies, including Mandl et al. (1977), Zhang and Tullis (1998), Garga and Sendano (2002), Sperrevik et al. (2002), Clausen and Gabrielsen (2002), Agung et al. (2004) and Sassa et al. (2004) used a low stress ring-shear apparatus. Mandl et al. (1977) used the ring-shear apparatus to study the development of shear zones and the accompanying changes in texture and stress state in granular material at a maximum of 920 kPa. Agung et al. (2004) investigated the evolution of shear zone structure in undrained ring-shear tests at 180 kPa under different shear displacements.

In the present study the occurrence and development of shear zones in sand has been investigated using a new high-stress ring-shear apparatus designed and built at the Norwegian Geotechnical Institute (NGI, Oslo, Norway). This instrument can handle up to 20 MPa imposed normal stresses, corresponding to about 2 km or more of overburden. Our aim is to explore the formation of shear zones and associated porosity change inside deformed sample at the simulated condition of relatively shallow burial depth. We implement the experimental results in the interpretation and classification of natural shear zones. Our outcrop samples are from an in-house database on faulted sandstones in Sinai (Egypt), Corsica (France), and Utah (USA). In the light of burial depth for the study areas at the time of deformation we studied and compared the results of experiments and natural rocks in order to further understand the physical processes of faulting. This has been performed by microstructural study of deformed sand and sandstones based on comparison of thin sections from experiments and from natural rocks.

2. Ring-shear apparatus

The ring-shear device was originally designed to study the residual strength of soils (Hvorslev, 1939; Bishop et al., 1971). In the ring-shear apparatus, the sample is forced to shear along a predefined plane located at the separation of the upper and lower confining rings (Hvorslev, 1939). Later Mandl et al. (1977) used the ring-shear apparatus to study shear zones in granular material. For a good historical review of the ring-shear apparatus and further information, the reader is referred to Sassa et al. (2004). The effect of clay and sand properties, strain rate and geometrical aspects on the clay smear continuity in the fault zone has been studied by Sperrevik et al. (2002) and Clausen and Gabrielsen (2002), both performing their experiments at NGI. Limitations inherent

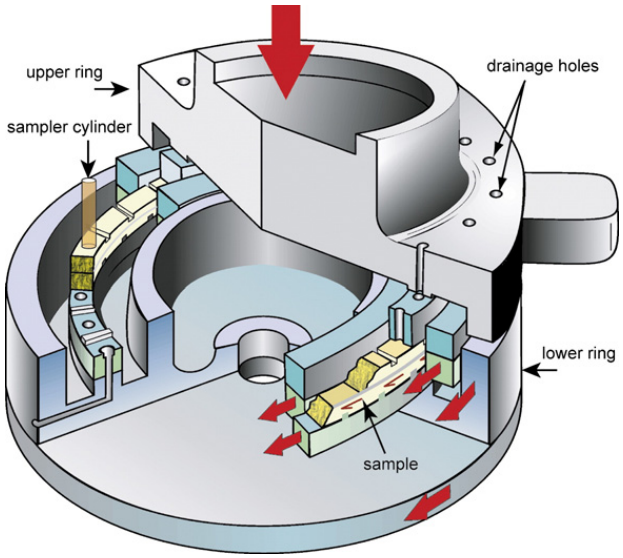

Fig. 1. A simplified sketch of the ring-shear cell. Rotating parts are drawn in light blue and movable parts in grey. The material sample is yellow. The horizontal red arrows on the lower ring indicate direction of movement. The vertical red arrow on the top of the upper ring shows the direction of loading on the ring-shear cell. Notice the drainage points placed on the upper and lower rings and knives to transfer shear stress to the sample. The width of the ring specimen is 25.4 mm and its height is 45 mm. The area of the sample is equal to 223 cm^2. The diameter of sampler cylinder is 1 in. Courtesy of NGI.

in the previous ring-shear apparatus at NGI (i.e. low stress level used for geotechnical applications) have motivated the construction of a new ring-shear device (Fig. 1). The new ring-shear apparatus can handle up to 20 MPa normal stresses, simulating more than 2 km burial depth, thus representing a significant improvement over the previous one. Besides, thin sections prepared from final samples can be used for porosity measurements and particle size analysis and further in the analysis of deformation under different stress conditions.

The ring-shear apparatus operates as a uniaxial deformation device during normal loading prior to shearing (similar to Mandl et al., 1977). During the rotation in the Mandl ring-shear apparatus, the normal loading remains constant but the maximum principal stress rotates due to shear stress such that at the horizontal shear zone the angle between the shear zone and the normal stress is equal to 45° (see Mandl et al., 1977).

The ring-shear apparatus consists of five parts (Cuisiat and Skurtveit, 2006):

- The ring-shear assembly and reaction frame
- The loading system
- The shearing system
- The hydraulic system
- Instrumentation, data acquisition and control systems

The ring-shear assembly consists of a pedestal, upper and lower frames, upper and lower rings, and inner and outer confining rings. The sample is contained within the annular space created between the inner and outer confining rings, and the lower and upper rings. The width of the annular space between the rings is 25.4 mm. The maximum height of the sample is 45 mm, limited by the need for seating of the O-rings at the upper ring to ensure hydraulic sealing. The area of the sample is equal to 223 cm^2. On the upper and lower rings, 48 knives (or grooves) are evenly located to ensure transfer of the torque to the specimen. 48 openings for valves are evenly distributed between the knives at the upper and lower rings for flow measurements. During shearing, the upper ring is fixed and only the lower ring rotates clockwise. Two reaction arms on the upper frame provide the reaction forces against the rotation forces of the lower assembly. Two load cells measure the reaction forces, which in the absence of friction are equal to the shear forces exerted on the specimen.

The following variables are measured during an experiment:

- Vertical force from MTS (MTS is a registered trademark) load cell (F_{MTS})
- Lateral forces F1 and F2 from tangential load cells
- Stroke from MTS transducer (δ_{MTS})
- Axial displacement from internal LVDT, i.e. Linear Variable Differential Transformer, (δ_{LVDT})
- Absolute motor rotation, torque, rotation velocity
- Pore pressures at upper and lower GDS (Global Digital System Ltd.) pumps (u_{up}, u_{low})
- Pressure difference across sample from pressure transducer (Δu)
- Status of automatic valves (open/closed)

The following variables are calculated and logged during an experiment:

- Shear stress τ : $\tau = \dfrac{2(F_1 + F_2)R}{\pi(r_o + r_i)(r_o^2 - r_i^2)}$

  where R is the radial distance between lateral load cells, r_o is the outer radius of the test specimen and r_i is the inner radius of the specimen; F_1, F_2 are the lateral forces from tangential load cells.
- Normal stress σ : $\sigma = \dfrac{F_{MTS}}{\pi(r_o^2 - r_i^2)}$

  where F_{MTS} is the vertical force from the MTS machine;
- Shear displacement at mid-sample l : $l = 2\pi \dfrac{(r_o + r_i)}{2} \dfrac{\theta}{360}\theta$

  is the rotation angle of the lower ring in degrees.

3. Ring-shear sample description and testing procedures

The test program was designed for initial testing of the apparatus and to explore its potential for studying sand deformation. In total, four different types of sand have been used (Table 1). Three types of sand from

Table 1
Description of sands used in the ring-shear experiments

Type of sand	Grain size (D_{60}) in mm	Age	Type	Angularity	Location
Bornholm no. 1	0.4	Jurassic	Quartzarenite	Subrounded–subangular	Denmark
Bornholm no. 17	0.2	Jurassic	Quartzarenite	Subrounded–subangular	Denmark
Bornholm no. 15	0.93	Early Jurassic	Quartzarenite	Subrounded–subangular	Denmark
Baskarp	0.17	Holocene	Quartzarenite	Subangular–angular	Sweden

Bornholm, Denmark (Jurassic) and a Holocene, well-sorted sand from Baskarp, Sweden were used for the low stress experiments. The Baskarp sand was also used for the high-stress experiments. The sands contain more than 90% quartz and have different grain size and angularity. The Bornholm sand was chosen because of its sub-rounded form and availability in different grain sizes at NGI. We have performed drained experiments at atmospheric pore pressure, and the shear rate was so slow that any induced overpressure would not exceed 100 kPa at any time during shearing. This value is small compared to the total normal stress applied on the specimen (5 or 20 MPa), which ensures that the shear induced pressure build-up will not influence the frictional behavior of the sands. Testing procedures for the new ring-shear apparatus were developed during the experimental program (Cuisiat and Skurtveit, 2006).

- The silt fraction (>0.075 mm) of the material was removed prior to mounting of the sample because of potential clogging of the filters by fine material.
- Sand was tamped into the cell in a wet condition. The amount of water needed varies with the type of sand, the mixture should be sticky, not a slurry.
- The lower ring was filled with sand. The top surface was flattened with a flat knife.
- First the sample was saturated with water. The experiments were then carried out in drained conditions (outlet opened to atmosphere).
- The sample was then loaded normally with a rate of 1 MPa/min until the desired normal stress was reached.

In tests RT04, RT05, RT06, RT08, RT09, RT10, RT13; a vertical cyclic load at 28 kN was applied (100 cycles: mean: 28 kN, amplitude: 5 kN, frequency: 0.05 Hz) to ensure full penetration of the "knives" into the sample, and homogeneous stress distribution within the sample.

- Minimum rest period was 15 min before shearing.
- The shearing has been done stepwise with stops for flow measurements under constant normal stresses (shear rate was 2°/min). Flow measurement was done before every stage of shearing.
- Thin section samples were collected with a steel cylinder at the end of the tests. The steel cylinder was pushed down vertically into the sample (perpendicular to the shear zone) from top to the bottom without lateral movement. The samples were oven-dried at 105°C for 24 h and then impregnated with epoxy under vacuum. A detailed description of the tests is presented in Table 2.

4. Methodology of analyzing the thin sections

Polished thin sections from sheared sand and sandstones have been prepared and studied by both optical and Scanning Electron Microscope (SEM). Backscattered Electron Images (BSE) from the SEM were generated from thin sections and analyzed by means of standard image analysis software (ImageJ). Particle size area distributions based on grain areas were obtained from the BSE Images. The selected areas in pixels were calibrated in square millimeters by setting the real scale on the image.

The description of the particle size distribution for the samples includes statistical analysis. The latter is presented as exceedence frequency plots for all the thin sections. Exceedence Frequency (EF) of a particular value of a measured variable is defined as the number of data with values greater than that value, divided by the total number of the data.

Table 2
Description of the ring-shear experiments

Test no.	Sand type	Grain size (D_{60}) in mm	Initial porosity (%)	Porosity reduction due to loading	Initial height (mm)	Vertical stress (MPa)	Rotation (degree)	Shear displacement (mm)
RT01	21 Bornholm	0.373	44.6	2.9	40	5	45	109.75
RT02	21 Bornholm	0.373	45	3.3	40	5	60	146.34
RT03	21 Bornholm	0.373	45	3.3	40	5	75	182.93
RT04	21 Bornholm	0.373	45	4	44	5	360	878.07
RT05	17 Bornholm	0.191	47.5	2.4	40	5	60	146.34
RT06	15 Bornholm	0.934	43.4	6.8	44	5	150	365.86
RT08	Baskarp	0.176	37	1.7	45	5	450	1097.6
RT09	Baskarp	0.176	41	4.1	44	20	75	182.93
RT10	Baskarp	0.176	41	5.4	44	20	45	109.75
RT13	15 Bornholm	0.934	43	3.5	44.5	5	75	184.06

In the present study, the plots of log EF versus log particle size areas have been investigated. The best fit for a given particle size distribution of a shear zone is a power law described by its dimension D (exponent). The calculated D is two-dimensional but can be converted to three dimensions by simply adding 1 (Sammis et al., 1987; Blenkinsop, 1991).

Porosity has been measured in thin sections through binary images from BSE images (Table 3). However, since porosity measurements are influenced by the threshold level between black (pores) and white (particles) pixels, and any void appears black in the binary images, the measured porosities may be slightly overestimated.

5. Results from ring-shear experiments

Based on the detailed analysis of the thin sections from the ring-shear experiments we have classified the shear zones into two different categories:

i) Shear zones with diffuse boundaries formed at low level of stress.
ii) Shear zones with sharp boundaries formed at higher levels of stress.

This division is supported by particle size analysis using high-resolution 2-D images (BSE images) from thin sections. In this context, it is important that the distributions and not the averages of particle sizes are indicative of the underlying processes of cataclastic deformation (Marone and Scholz, 1989). At a low level of stress (5 MPa normal stress), flaking of the grains is the dominant mode of deformation (Fig. 2a), resulting in rough grain surfaces. At higher levels of stress (20 MPa normal stress), the grains mostly break by splitting (Fig. 2b). Changing of the dominant grain breakage mode from flaking to splitting creates different types of shear zones. Based on thin section studies, vertical sections through the deformed sand have been separated into three main parts (Fig. 3a),

- The "top layer", representing the upper part.
- The "shear zone" or the middle part.
- The "bottom layer" or the lower part of the section.

The boundaries of the shear zones are for the most part gradual in the thin sections for experiments performed at 5 MPa normal stress and low rotations (shear displacements); such as for thin sections from experiments RT01, RT02, RT03, RT06 and RT13. We call such shear zones *diffuse boundary shear zones* (Fig. 3a). However, in some thin sections, such as RT04, RT08 and RT09, RT10; sharp shear zone boundaries are visible at high shear rotation (high displacements) under 5 MPa normal stresses. They are also present for the relatively lower shear strain displacements obtained under 20 MPa normal stresses. The margins of such *sharp boundary shear zones* are here named the "upper" and "lower shear zone margin", respectively (Fig. 3b). The diffuse boundary shear zones are wider than the sharp boundary shear zones. RT09 (20 MPa; 75 degree rotation) represents the best example of

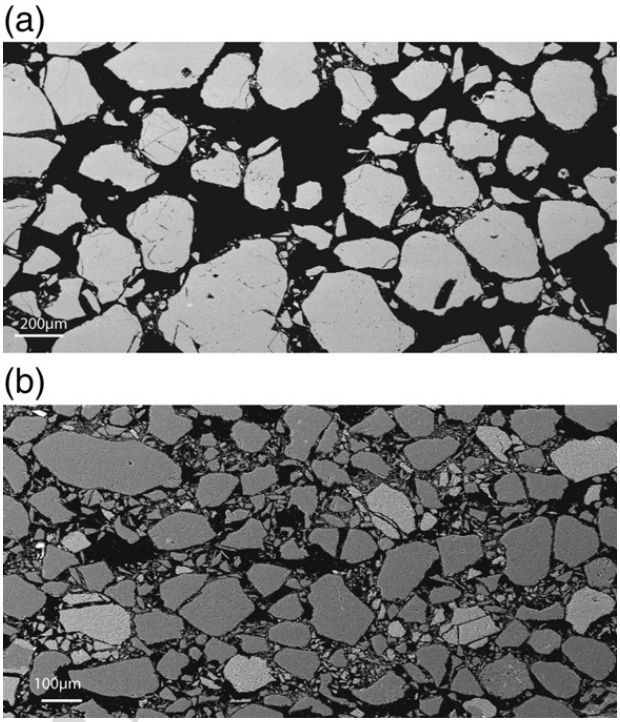

Fig. 2. Different types of grain breakage in thin sections; (a) grain flaking is dominant at low level of stress (BSE image from RT01, top layer); (b) grain splitting is the dominant mechanism at higher levels of stress (BSE image from RT09, top layer).

Table 3
Estimated porosities from BSE images of thin sections from ring-shear experiments

Test no.	Initial porosity (%)	Top layer porosity (%)	Upper margin shear zone porosity (%)	Shear zone porosity (%)	Lower margin shear zone porosity (%)	Bottom layer porosity (%)
RT01	44.6	42	–	33	–	–
RT02	45	39	–	23		
RT03	45	40	–	20		
RT04	45	32	20	15	18	30
RT06	43.4	35		24		31
RT08	37	34	31	11	29	30
RT09	41	24	20	13	15	25
RT10	41	18	9	7	11	28
RT13	43	32		15		36

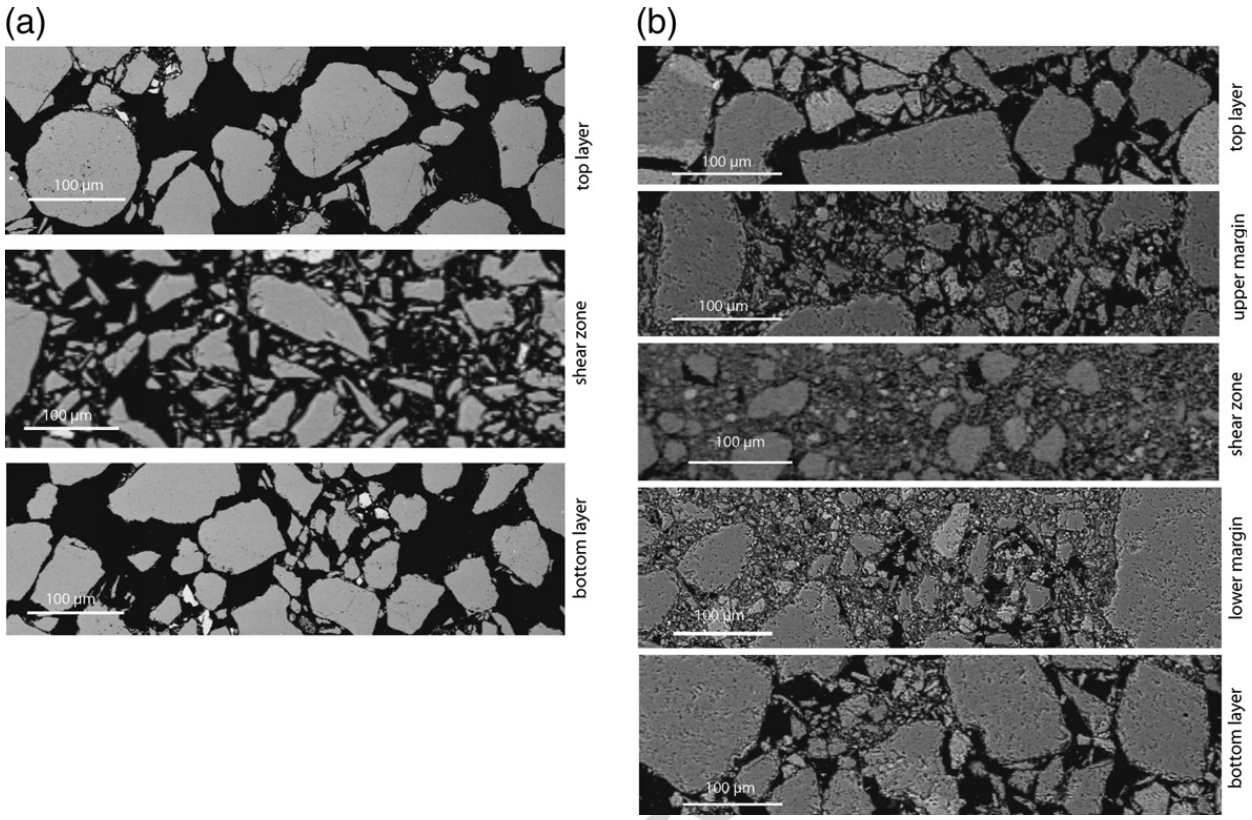

Fig. 3. Classification of shear zones based on BSE images from SEM study; (a) note the formation of a diffuse boundary shear zone at low level of stress, seen in an example from RT02 and (b) sharp boundary shear zone at high level of stress, seen in an example from RT09.

a strongly layered shear zone. This shear zone shows a more compacted central part with maximum reduction in particle size and significant porosity decrease (Figs. 3b and 4a, b). The shear zone is surrounded by margins and the top and bottom layers that contain coarser particle size compared to the shear zone. In sharp boundary shear zones like RT09 there is an asymmetry in the particle size distribution, with slightly more particles size reduction in the lower than the upper margin. Similar observations have been reported by Mandl et al. (1977) and Agung et al. (2004) for layered shear zones.

The particle size distribution plots for sample RT09 (Fig. 4b) indicate that the best fit to the particle size distribution is a power law with a low D value (1.44). The overall results reveal that increasing the normal stress and/or shear stress (by rotation) changes the D values gradually from 1.4 at low levels of stress to 1.5 at higher levels of stress. Based on the results of the experiments, we have chosen to explore three variables, namely the role of shear displacement, grain size and loading.

5.1. The role of shear displacement

Four experiments have been conducted on the pure, medium-grained, sub-rounded Bornholm sand at 5 MPa. The experiments involved different amounts of rotation (shear displacement, Fig. 5a). With increasing shear displacement, the shear stress rose up to yield strength, which is the start of dominant grain fracturing between 2.3–2.7 MPa for these experiments. The post-yield development was in two parts, with an early (low-strain) history of gentle increase in shear stress and general shear localization (seen in RT01, RT02, RT03, RT04, Fig. 5a) before the shear stress started to increase faster (as seen in RT04 in Fig. 5a). Fig. 5b illustrates that the porosity change during the rapid increase of shear stress (up to 2.7 MPa) is very small. In the first part of the post-yield evolution porosity decreased faster than in the second part (only observed in RT04). This change indicates the onset of strong shear localization in the sand. The irregularities in the curves in Fig. 5a and b are probably related to uneven penetration of the knives into the specimen to transfer shear stress. The analysis of particle size distribution of thin sections from RT01, RT03, and RT04 reveals progressively more particle size reduction with increasing shear strain (displacement), see Fig. 6. The shear zones in the first three tests (RT01, RT02, and RT03) can be classified as shear zones with diffuse boundaries. The

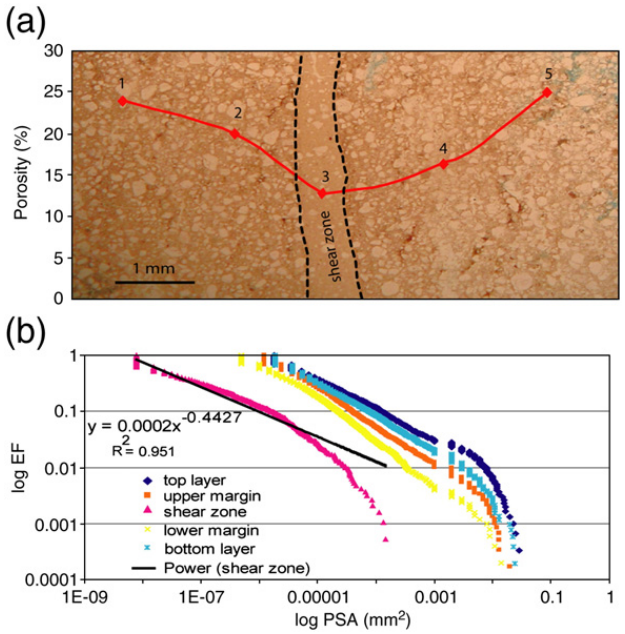

Fig. 4. Sharp boundary shear zone in an example from RT09; (a) Porosity variation inside the sample presented on the petrographic image; the maximum reduction occurred in the middle of the shear zone (point 3); points 1 and 5 show approximate locations of top and bottom layers and points 2 and 4 show locations in upper and lower margins. (b) Particle size analysis of the sample RT09, which shows EF (exceedence frequency) versus PSA (particle size area). Note the particle size reduction from outside the shear zone towards the middle of the shear zone. The shear zone is well layered and classified as a sharp boundary shear zone. A power law fit represents the best fit on the curve with 95% confidence.

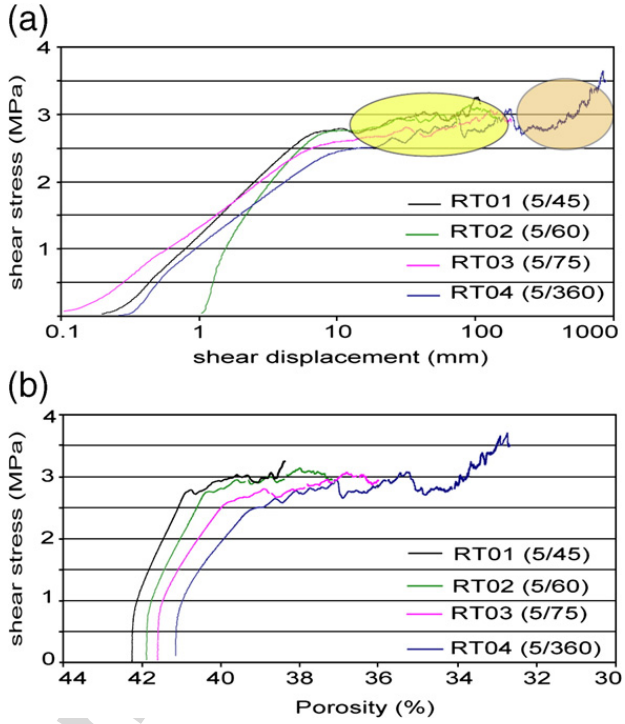

Fig. 5. (a) Shear stress versus shear displacement for RT01, RT02, RT03, RT04, which illustrate that with increasing shear displacement, shear stress rises up to yield strength (start of the grain crushing at 2.3–2.7 MPa). The post-yield has two parts, the first part has a gentler slope (yellow ellipse) than the second part (brown ellipse); the numbers in parentheses refer to normal stress in MPa, and rotations in degrees respectively. (b) Porosity is approximately constant in pre-yield part of the experiments. The porosity reduction is faster in the first part of the post-yield field.

shear zone in RT04 can be interpreted as a sharp boundary shear zone.

5.2. Effect of grain size

The ring-shear dataset enables the comparison of sands with different grain sizes, since the sands employed vary from medium-grained Bornholm sand in RT01, RT02, RT03, and RT04 via coarse-grained Bornholm sand in RT06 and RT13 to fine-grained Bornholm sand in RT05 (Table 1). Comparison of the results from experiments RT01, RT02, RT03, RT04, RT05, RT06, and RT13 shows no significant change in the frictional coefficient (ratio of shear stress to normal stress) of the sands with change in grain size at 5 MPa normal stresses; they show similar behavior for comparable shear displacements (Fig. 7a). However, *increasing* the degree of rotation from test to test makes significant differences in the final grain size distribution. Similarly, when comparing particle sizes of RT03 and RT13, which were both run at 5 MPa and 75 degree rotation (i.e. 182.93 mm shear displacement), the results show similar grain size reduction for two different grain sizes (Fig. 7b). Both of the shear zones can be defined as having diffuse boundaries.

5.3. Effect of loading

Normal stress prior to rotation creates irreversible deformation due to compaction of the sand (Fig. 8a).

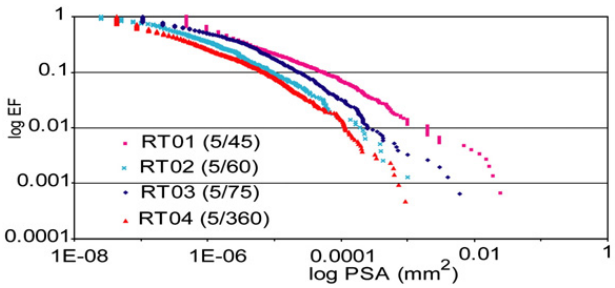

Fig. 6. Particle Size Area (PSA) versus Exceedence Frequency (EF) for shear zone samples from RT01 (45 degree, rotation), RT02 (60°), RT03 (75°), RT04 (360°), all loaded to 5 MPa but experiencing increased rotation. The plot shows how increased rotation reduces the particle size systematically. The numbers in parentheses refer to normal stress in MPa, and rotation in degrees respectively.

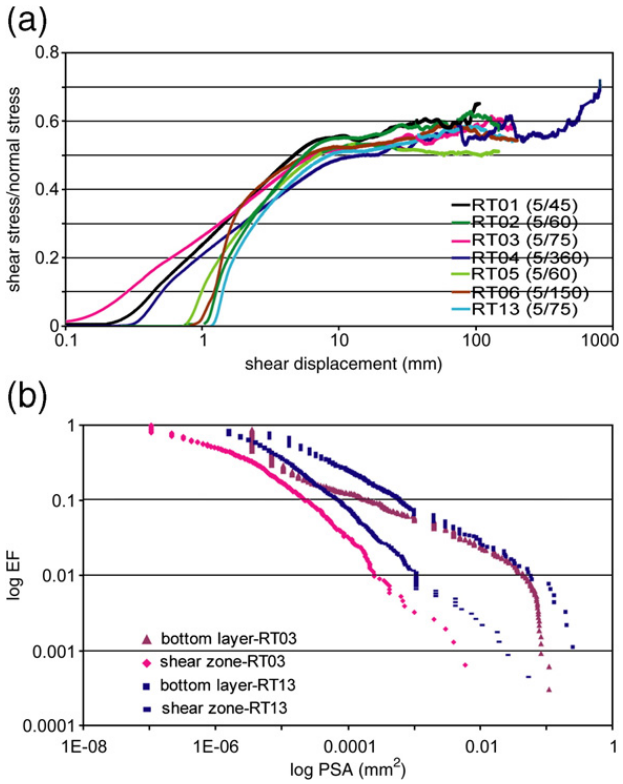

Fig. 7. (a) Friction coefficient as a function of shear displacement for coarse (sample from RT06 and RT13), medium (RT01, RT02, RT03, RT04), and fine (RT05) grained Bornholm sand. The plots suggest similarity in friction coefficient for experiments run at 5 MPa. (b) Particle size analysis for samples from RT03 (medium Bornholm sand) and RT13 (coarse Bornholm sand) both deformed at 5 MPa normal stress. They show a similar distribution of the particle size reduction for the two tests. The numbers in parentheses refer to normal stress in MPa, and rotation in degrees respectively.

Furthermore, compilation of all of the experiments (Fig. 8b) shows that with increasing axial strain during normal loading prior to shearing, the porosity decreases, thus confirming compaction during normal loading. Once rotation is imposed and shear displacement starts to accumulate in the post-yield stage, fracturing becomes more pronounced. Comparison of the test RT08 (5 MPa, 450 degree rotation) with RT09 (20 MPa, 75 degree rotation) and RT10 (20 MPa, 45 degree rotation), all run on fine-grained Baskarp sand (Fig. 9), show that at higher (20 MPa) normal stress, the yield strength increases to more than 10 MPa, and the shear zone becomes more localized. With further increase in shear displacement, the shear stress declines in RT09 and RT10. Test RT08, on the contrary, shows a pronounced peak in its yield strength, which can be related to lower, imposed normal stress (5 MPa) and low initial porosity. This is in accordance with Kjelstad et al. (2002), who showed the effect of initial porosity on the behavior of the same type of sand in direct shear ex-

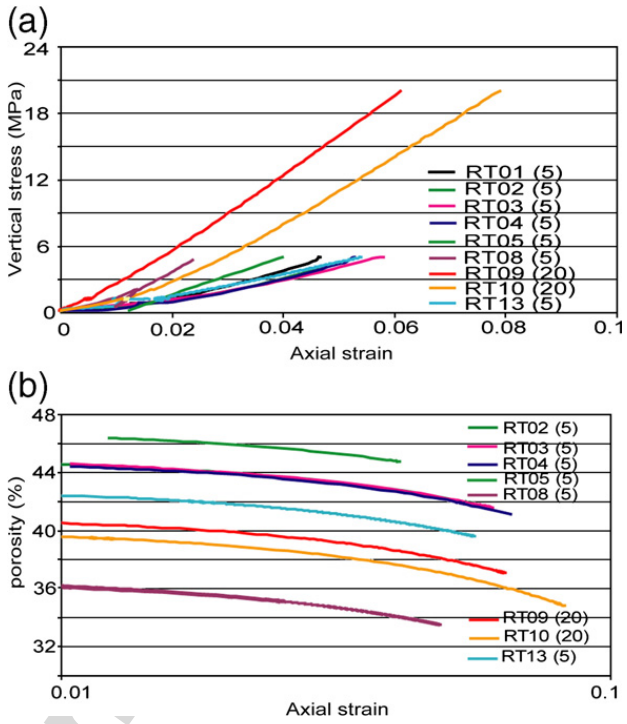

Fig. 8. (a) Effect of initial loading, all the experiments show compaction of the sand at the loading stage. (b) Effect of loading on porosity for all samples; with increase in axial strain the porosity decreases as a result of compaction. The numbers in parentheses refer to normal stress in MPa.

periments. Further, RT08 shows that after reaching the yield strength, the shear stress drops to a stable level (residual strength), see Fig. 9.

6. Examples of natural shear zones

Small shear localizations that form as a result of compaction and shear in porous rocks in nature are

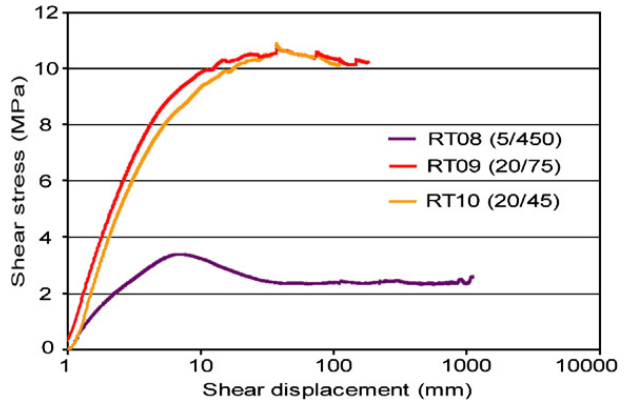

Fig. 9. Shear strength increases at higher normal stresses, comparison between tests RT09, RT10 (20 MPa) and RT08 (5 MPa), all run on fine-grained Baskarp sand. The numbers in parentheses refer to normal stress in MPa, and rotation in degrees respectively.

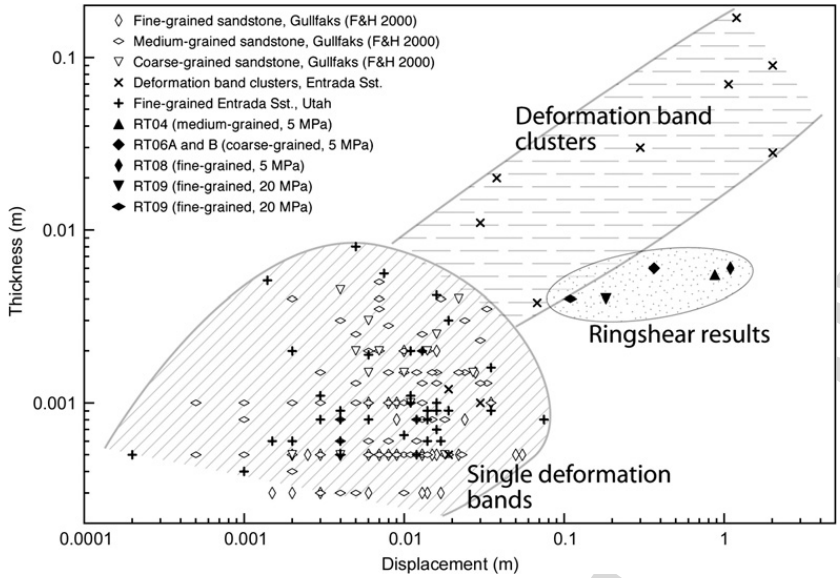

Fig. 10. Thickness and displacement relationship for natural deformation bands and experimental shear zones; the shear zones from ring-shear experiments show approximately similar thickness but higher displacement than the natural single deformation bands, in this sense they are similar to the deformation band clusters. Data from Gullfaks are from Fossen and Hesthammer (2000).

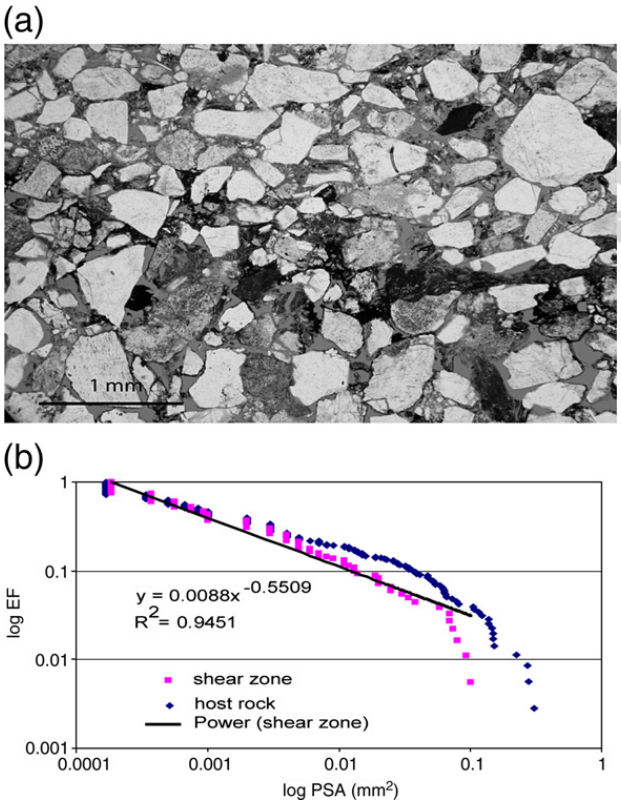

Fig. 11. (a) Petrographic image of the shear zone from thin section Corsica-3 (France). Note that, owing to the extensive flaking, the shear zone is classified as diffuse boundary shear zone. (b) Particle size analysis of the sample, which shows particle size reduction in the shear zone. The power-law fit to the shear zone particle size distribution has a low *D* value.

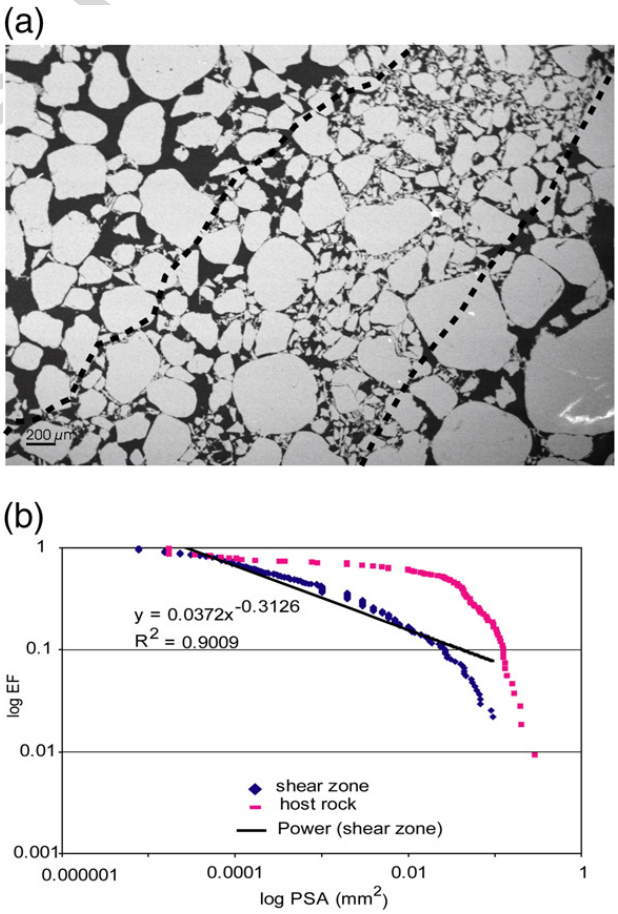

Fig. 12. (a) BSE image from thin section TM-4 (Sinai, Egypt). Note both flaking and splitting of the grains; the shear zone is classified as diffuse boundary shear zone. (b) Particle size analysis of the sample, which shows particle size reduction in the shear zone. The power-law fit to the shear zone particle size distribution has a low *D* value.

called deformation bands (Aydin, 1978) or, more specifically, compactional shear band (Schultz and Siddharthan, 2005; Fossen et al., in press). They have been studied throughout the world (e.g., Underhill and Woodcock, 1987; Fowles and Burley, 1994; Antonellini and Aydin, 1999; Antonellini and Aydin, 1999; Fossen and Hesthammer, 2000; Lothe et al., 2002; Rawling and Goodwin, 2003). Comparison of natural deformation bands with the experimental shear zones presented here reveals that they have a similar mm- to cm-scale range in thickness (Fig. 10). On the other hand, most natural examples have maximum displacements of a few centimeters, while created shear zones in ring-shear apparatus have up to 100 cm displacement.

We have studied samples from faulted, porous sandstones collected from Sinai (Egypt), Corsica (France), and Utah (USA). Most deformation bands in the database are not easily comparable with the experimental shear zones, however, there are similarities that are useful to highlight in a comparison. The differences can for example be ascribed to the occurrence of cement that is found in most reservoir sandstones. In order to avoid the effect of cement, which is absent in the experiments, the degree of cementation is small or negligible in the selected samples. Three thin sections were selected as examples due to good similarity with experimental shear zones. Thin section Corsica-3 shows a deformation band in poorly consolidated, shallow marine, medium-grained sandstone, sampled in the damage zone of a normal fault in the Aleria basin (Corsica, France). The sand is composed mainly of quartz, some feldspar and rock fragments. The throw of the band is about 5 mm, and was formed at a maximum burial depth of about 100 m. Thin sections TM-4 and WK-7 show deformation bands in a medium-grained fluvial sandstone sampled in the damage zone of the Tayiba Fault in Nubian Sandstone (eastern Suez Rift, Egypt) (Beach

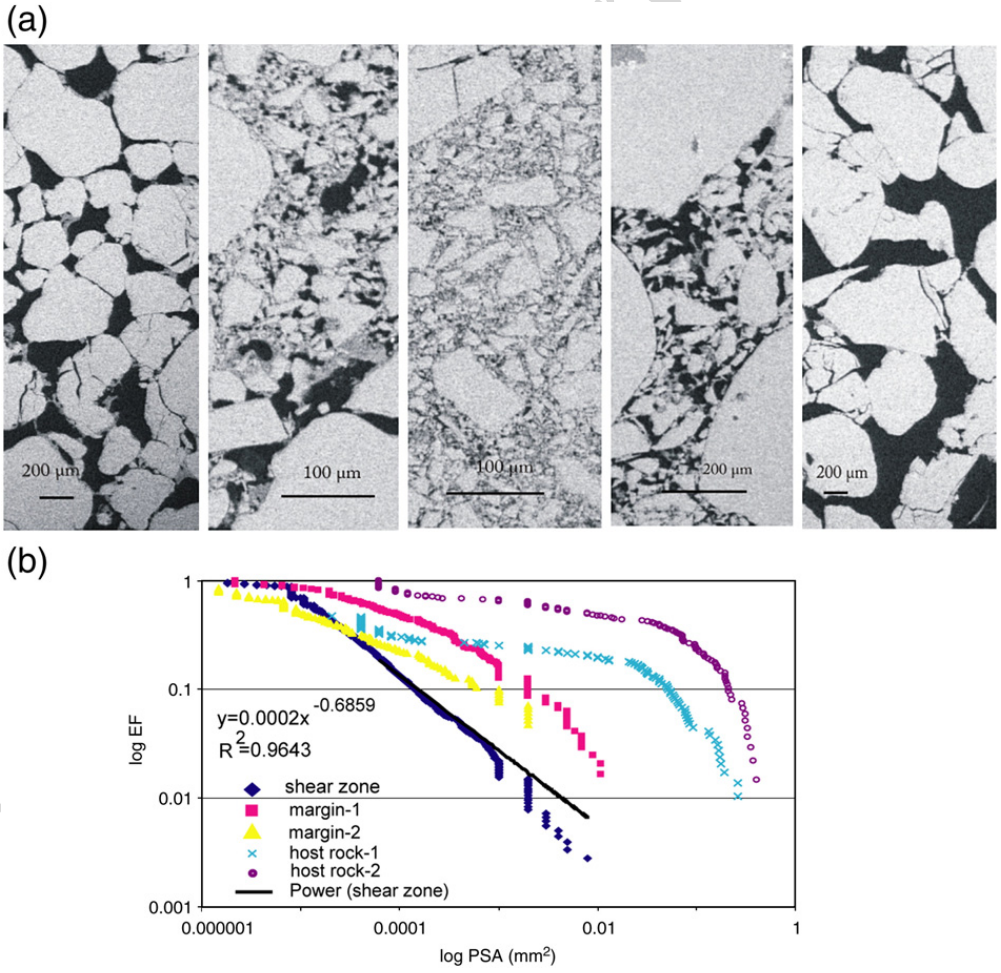

Fig. 13. (a) BSE images from thin section WK-7 (Sinai, Egypt); which presents a more compacted part in the centre of the shear zone and two margins (comparable to upper and lower margins in ring-shear result) and hosts (comparable to top and bottom layers). The shear zone can be considered as sharp boundary shear zone. (b) Grain size analysis of the thin section, which presents the grain size reduction from hosts to the shear zone; Note to the power-law fit to the shear zone with a low *D* value.

et al., 1999). The Nubian sandstone contains more than 90% quartz. The Tayiba fault has a throw of 120–150 m, whereas the deformation bands show throws of around 1 cm. The maximum burial depth during the formation of these structures is almost 1.5 km (Sharp, personal communication). However, a somewhat shallower depth is possible since the region was partly unroofed during progressive regional rifting.

Grain flaking is the dominant grain breakage mechanism in Corsica-3 (Fig. 11a and b), as seen by larger grains surrounded by a very fine-grained matrix in the deformation band. The band is dominated by two grain sizes and contains significant porosity. On the contrary, in TM-4 from Sinai, both flaking and splitting of grains are observed. The combination of flaking and splitting results in a few larger grains surrounded by a finer-grained matrix with a very heterogeneous grain size (Fig. 12a and b). Based on particle size analysis, the shear zones in the Corsica-3 and TM-4 are comparable to the diffuse boundary shear zones from the ring-shear experiments (Figs. 11a and 12a). WK-7 is zoned (Fig. 13a) and with a sharp boundary to the host sandstone. The core contains some smaller particles surrounded by a heterogeneous matrix, which is characteristic for combined flaking and dominant grain splitting, and the porosity is very low. The marginal zones contain larger particles but otherwise a matrix similar to the core. In this case the porosity is significantly higher. Study of the BSE images suggests that splitting is more pronounced than flaking. Grain size analysis of WK-7 (Fig. 13b) confirms the presence of a zoned shear zone with a central part of maximum grain size reduction, i.e. similar to the sharp boundary shear zone from ring-shear experiments. Besides, the grain size analysis of the shear zone from the thin sections show a power law distribution with low D values that, when compared with experimental shear zones, fits a pattern of gradual increase from 1.4 to 1.5 with higher stress (increasing burial depth and displacement).

When comparing the three examples of deformation bands, there seems to be an effect of burial depth. Near-surface faulting, as exemplified by Corsica-3, is dominated by flaking. At significant depth, represented by TM-4 and WK-7, grain splitting becomes pronounced and contributes in combination with flaking to significant grain size reduction. However, TM-4 and WK-7, which are from the same site, show clear differences. TM-4 is a diffuse boundary deformation band without zonation whereas WK-7 is a sharp boundary band that is zoned. As regards porosity, the band in TM-4 can be compared with the marginal zones of WK-7. Such differences could be explained by, for example, different burial depth during formation, since the region has experienced progressive unroofing, or by differences in shear or localization processes, or the velocity of deformation might explain the difference between WK-7 and TM-4. We return to this discussion below.

7. Discussion

There are limitations in the ring-shear experiments that have an impact on their value for comparison with deformation bands and faulted sandstone in nature. For example, the initiation of the shear zone is along a predefined plane, there is limited thickness of the confined sample inside the rings that hampers shear zone widening, and no cement is present contrary to the general observations from reservoir sandstones.

In the following, we first address the types of shear zones and the importance of grain characteristics identified in the experiments, before comparing the experimental shear zones with natural deformation bands. The latter is crucial in order to validate the experimental results before applying such results in reservoir models. According to the experiments reported here, the normal stress is the key factor that influences the type and thickness of shear zone, and the initial grain size is a subordinate factor. We conclude with a general discussion of grain size distribution, deformation mechanisms and porosity that can be expected in deformed sand and sandstone from different burial depths.

7.1. Formation of different type of shear zones

Two types of shear zones were observed in our experiments; (i) *diffuse boundary shear zones* and (ii) *sharp boundary shear zones*. Diffuse shear zones were also reported by Mandl et al. (1977) and Agung et al. (2004) who produced layered shear zone structures in both drained and undrained ring-shear tests at low normal stresses. Agung et al. (2004) divided the shear zone into three layers: The compacted core and the adjacent zones above and below the core. The sharp boundary shear zones produced in the current experiments are previously unreported from ring-shear experiments run on natural porous sand but they have been reported from the experiments on crushed granite (Beeler et al., 1996; Scruggs and Tullis, 1998). They are similar to the zoned deformation bands presented by Gabrielsen and Aarland (1990). They appear at higher levels of normal stress, as illustrated by experiments RT09 (Fig. 3b) and RT10 and are comparable with deeper burial depths as shown by the natural deformation band in WT-7 (Fig. 13) and also at high shear displacements according to the observations from experiment RT04.

Shear displacement affects the deformation mechanism. Fracturing of the grains becomes more pronounced with increased rotation in the experiments at 5 MPa (e.g. experiment RT04). At the same time the shear zone becomes more localized and strain hardened (Fig. 5a). This development can be directly linked to the formation of a sharp boundary shear zone (for example in RT04). In more detail, deformation progresses from the first part of the post-yield to the second part, representing a switch from early strain softening probably caused by crushing of the grains by either flaking or splitting in the yield stage, to strain hardening related to interlocking of the crushed grains in the shear zones followed by shear localization (Fig. 5a, b). At higher normal stress (20 MPa), the yield strength increases to more than 10 MPa (RT09 and RT10). In this condition, the mode of grain breakage is dominated by splitting rather than flaking of the grains, which leads to more compaction in the shear zone, seen as particle size and porosity reduction. The shear zone at this high normal stress (20 MPa) can be defined as a sharp boundary shear zone with a pronounced shear zone in the middle (Fig. 2b).

7.2. Effect of grain characteristics on deformation

Investigating the effect of grain size on frictional behavior of the sand (Fig. 7a) shows that initial grain size has no influence on the deformation behavior at 5 MPa normal stresses. According to Kjelstad et al. (2002), at normal stresses higher than 5 MPa, the strength values of initially loose sands are very similar for coarse-, medium-, and fine-grained mono-quartz sand. On the contrary, the effect of grain angularity and Particle Size Distribution (PSD) is important for the deformation of granular materials, as documented by Mair et al. (2002). They show that frictional strength and stability of a granular shear zone are sensitive to grain shape and Particle Size Distribution (PSD) during shear zone evolution. The impact is identified for different level of stress (5–25 MPa).

7.3. Comparison of experimental shear zones and natural deformation bands

The shear zones of the ring-shear experiments have a maximum thickness of 5 mm, which is approximately similar to that found for natural deformation bands, but the ring-shear experiments result in higher displacements (Fig. 10). Increasing the normal stress in the experiments (similar to burial depth in natural examples) leads to thinning of the shear zone and localization of strain. In this light, the high-displacement experimental shear zones can also be considered as analogues to sheared sand and sandstone in the core of faults. In the comparison of deformation bands sampled in sandstone from Corsica and Sinai with the experimental shear zones, it becomes clear that the experimental shear zones do not perfectly reproduce the natural examples. This can mostly be ascribed to the presence of cement in reservoir sandstone and the space restrictions imposed by the ring-shear apparatus.

Evidence of grain reorganization and flaking similar to sample Corsica-3, reveals shallow cataclasis at less than 1 km depth and favors the formation of diffuse boundary shear zones. Flaking of sand grains has also been observed in poorly consolidated sand in the Rio Grande Rift (Rawling and Goodwin, 2003). With increasing burial depth, our observations indicate that grains start to break by splitting rather than flaking, thereby promoting cataclasis (TM-4). At higher stress levels, sharp boundary shear zones form. At this stage, the deformation mechanism transgresses from predominantly flaking to predominantly splitting of the grains (e.g. the shear zone from sample WK-7 formed at about 1.5 km depth). Furthermore, grain size analyses of shear zones from the thin section show a power law distribution with low D values for all the three natural samples that fit a pattern of gradual increase of the dimension with higher stress (increasing burial depth and displacement).

7.4. Grain size distribution and deformation mechanism

In the present study, using different sands (quartz arenite) in the drained ring-shear experiments when (unlike the natural cases) there is no chemical alteration in the sample during deformation, the deformation of quartz and feldspar grains are similar at low normal stress (5 MPa, less than 1 km burial depth). Hence, grains have been broken mostly by flaking of the grain surfaces by abrasion, resulting in a low fractal dimension (1.4). With increasing burial depth (20 MPa, or more than 2 km burial depth), grains start to split. The change in the mode of fracturing from flaking to splitting increases the fractal dimension gradually. We conclude that the burial depth (normal stress in our experiments) and applied shear displacement are two significant factors influencing grain crushing and the resulting D values. Comparison of our results with previous studies reveals that even at 20 MPa normal stresses we do not reach the steady state particle size distribution ($D \sim 2.58$). We consider the mechanism of deformation at shallow depth/low level of stress to be dominated by reorganization, rolling and

flaking and minor splitting of the grains. This mechanism causes rough grain surfaces at the margins and within the shear zones, and produces a matrix of elongated grains surrounding surviving coarser grains. At deeper or at higher levels of stress the mode of fracturing transgresses from predominantly flaking to predominantly grain splitting, causing lower porosity values and increased particle size reduction.

Rawling and Goodwin (2003) assumed that their samples at low confining pressure had not reached a steady-state particle size distribution (characterized low D values of 1.7–2.1). Hence, with further deformation the particle size distribution would change, perhaps resulting in higher D values. Further, this transition results in a slow increase in the D values.

At higher confining pressure and burial depth, the relative size of the individual grains becomes an important factor influencing the grain fracturing (Sammis et al., 1987). At yet higher confining pressure, the third process of Blenkinsop (1991); (particle size reduction due to cataclasis); is responsible for fragmentation which is the development of cataclasis in a process of selective fracturing of relatively larger particles. This may also operate during localization and faulting.

A power-law gives the best fit for particle size area distribution of shear zones in this study. The power-law distribution is the only distribution that does not include a characteristic length scale. Thus it must be applicable to scale-invariant phenomena (Mandelbrot, 1982; Turcotte, 1997). A fractal distribution requires the number of objects larger than a specified size to have a power-law dependence on the size (Turcotte, 1997).

The power-law distributions, which fall within the limits of non-integer/fractional dimensions, i.e., $0<D<3$, can be defined as fractals and clearly scale-invariant (Turcotte, 1997). The power dimensions from both the experiments and natural examples are very low and so they might be considered as fractional dimensions. Since the dominant flaking at low stress levels creates angular and non-similar grains, the term self-affine might fit to this type of fractal. The power-law distribution is a non-linear relationship, which reveals that the obtained particle size distribution in the shear zones can be expressed by other factors, such as burial depth, stress levels at the time of deformation and strength of the grains.

8. Conclusions

Shear zones created in ring-shear experiments have been studied and compared with natural examples. Based on this study, the shear zone has been divided into three layers; (i) the “top layer”, representing the upper part; (ii) the “shear zone” or the middle part; and (iii) the “bottom layer” or the lower part of the section. The particle size distribution analysis shows that particle sizes are smaller in the middle part of the shear zone. The thin sections also show the development of two end-member types of shear zones: (a) Shear zones with diffuse boundaries formed at low levels of stress, and (b) Shear zones with sharp boundaries formed at higher levels of stress. We conclude that the burial depth (normal stress in our experiments) and the applied shear displacement are two significant factors influencing grain crushing and the resulting D values. We consider the mechanism of deformation at shallow depth/low level of stress to be dominated by reorganization, rolling and flaking of the grains. This mechanism causes rough surfaces of grains at the margins and within the shear zones. At higher burial depths or levels of stress the fracturing mode transgresses from predominantly flaking to predominantly grain splitting, causing lower porosity values and higher particle size reduction. Further, this transition result in a slow increase in the grain size-distribution D values.

We conclude that initial grain size has no influence on the deformation behavior of the sand at 5 MPa normal stresses. Comparison of experimental shear zones with the natural ones shows similar thickness but different displacements. Furthermore we presented comparable experimental shear zones to the natural examples.

Acknowledgments

The ring-shear experiments were carried out as part of the Fault Seal Project managed by the ”Norwegian Geotechnical Institute” (NGI) between 2003 and 2006, which was supported by NGI, The Norwegian Research Council (NRC), Norsk Hydro ASA, and Total. The permission to use data and publish the results is greatly appreciated. Professor Knut Bjørlykke (University of Oslo) advised in the course of the project. We appreciate the experimental work that has been carried out by Ra Cleave, Elin Skurtveit, Lars Grande and Trude Ørbech at NGI. Thanks go to Egil Erichsen for help with the SEM analyses and also to Brian Anthony Farrelly for his great help and kindness. This study was completed in the frame of Fault Facies Project at the Centre for Integrated Petroleum Research, University of Bergen, and supported by NRC, Statoil, Conoco-Philips, and Statoil-Vista.

References

Agung, M.W., Sassa, K., Fukuoka, H., Wang, G., 2004. Evolution of shear-zone structure in undrained ring-shear tests. Landslides 1, 101–112.

Antonellini, M., Aydin, A., 1999. Outcrop-aided characterization of a faulted hydrocarbon reservoir: Arroyo Grande Oil Field, California,

USA. Faults and subsurface fluid flow in the shallow crust. American Geophysical Union 113, 7–26.
Aydin, A., 1978. Small faults formed as deformation bands in sandstone. Pure and Applied Geophysics 116, 913–930.
Aydin, A., Borja, R.I., Eichhubl, P., 2006. Geological and mathematical framework for failure modes in granular rock. Journal of Structural Geology 28, 83–98.
Beach, A., Welbon, A.I., Brockbank, P.J., McCallum, J.E., 1999. Reservoir damage around faults: outcrop examples from the Suez rift. Petroleum Geoscience 5 (2), 109–116.
Beeler, N.M., Tullis, T.E., Blanoped, M.L., Weeks, J.D., 1996. Frictional behaviour of large displacement experimental faults. Journal of Geophysical Research 101 (B4), 8697–8715.
Bishop, A.W., Green, G.E., Garga, V.K., Andersen, A., Brown, J.D., 1971. A new ring-shear apparatus and its application to the measurement of residual strength. Geotechnique 21 (1), 273–328.
Blenkinsop, T.G., 1991. Cataclasis and processes of particle size reduction. PAGEOPH 136 (1).
Clausen, J.A., Gabrielsen, R.H., 2002. Parameters that control the development of clay smear at low stress states: an experimental study using ring-shear apparatus. Journal of Structural Geology 24 (10), 1569–1586.
Cuisiat, F., Skurtveit, E., 2006. Large strain testing of fault seals. Final Report on Fault Seal Project, NGI Repot No 2001288-3.
Fossen, H., Hesthammer, J., 2000. Possible absence of small faults in the Gullfaks Field, northern North Sea. Journal of Structural Geology 22 (7), 851–863.
Fossen, H., Schultz, R.A., Shipton, Z., Mair, K., in press. Deformation bands in sandstone — a review. Journal of the Geological Society (London), 164.
Fowles, J., Burley, S., 1994. Textural and permeability characteristics of faulted, high porosity sandstones. Marine and Petroleum Geology 11 (5).
Gabrielsen, R.H., Aarland, R.K., 1990. Characteristics of pre-syn-consolidation structures and tectonic joints and microfaults in fine- to medium-grained sandstones. Rock Joints. Balkema, Amsterdam, pp. 45–50.
Garga, V.K., Sendano, J.I., 2002. Steady state strength of sands in a constant volume ring shear apparatus. Geotechnical Testing Journal 25 (4), 414–421.
Hvorslev, M.J., 1939. Torsion shear tests and their place in the determination of the shearing resistance of soils. Proc. Am. Soc. Test. Mater., vol. 39, pp. 999–1022.
Kjelstad, A., Chuhan, F., Høeg, K., Bjørlykke, K., 2002. Cataclastic shear band formation in sands at high stresses: An analogue experimental model and its relevance for faults in sedimentary basins. PhD Thesis, University of Oslo.
Lothe, A.E., Bjørnevoll Hagen, N., Gabrielsen, R.H., Larsen, B.T., 2002. An experimental study of the texture of deformation bands: effects on porosity and permeability of sandstones. Petroleum Geoscience 8, 195–207.
Main, I., Mair, K., 2001. Experimental constraints on the mechanical and hydraulic properties of deformation bands in porous sandstones: a review. In: Holdsworth, R.E, Strachan, R.A., Magloughlin, J.F., Knipe, R.J. (Eds.), The Nature and Tectonic Significance of Fault Zone Weakening. Geological Society, London, Special Publication, vol. 186, pp. 43–63.
Mair, K., Fyre, K.M., M oren, C., 2002. Influence of grain characteristics on the friction of granular shear zones. Journal of Geophysical Research 107 (B10).
Mair, K., Main, I., Elphick, S., 2000. Sequential growth of deformation bands inthe laboratory. Journal of Structural Geology 22, 25–42.
Mandelbrot, B.B., 1982. The Fractal Geometry of Nature. Freeman, San Fransisco.
Mandl, G., de Jong, L.N., Maltha, A., 1977. Shear zones in granular material. Rock Mechanics 9, 95–144.
Marone, C., Scholz, C.H., 1989. Particle-size distribution and microstructures within simulated fault gouge. Journal of Structural Geology 11 (7), 799–814.
Ngwenya, B.T., Kwon, O., et al., 2003. Permeability evolution during progressive development of deformation bands in porous sandstones. Journal of Geophysical Research 108 (B7), 2343.t1 doi:10.1029/2002JB001854.
Rawling, G.C., Goodwin, L.B., 2003. Cataclasis and particulate flow in faulted, poorly lithified sediments. Journal of Structural Geology 25 (3), 317–331.
Sammis, C., King, G., Biegel, R., 1987. The kinematics of gouge deformation. PAGEOPH 125 (5).
Sassa, K., Fukuoka, H., Wang, G., Ishikawa, N., 2004. Undrained dynamic-loading ring-shear apparatus and its application to landslide dynamics. Landslides 1, 7–19.
Schultz, R.A., Siddharthan, R., 2005. A general framework for the occurrence and faulting of deformation bands in porous granular rocks. Tectonophysics 411, 1–18.
Scruggs, V.J., Tullis, T.E., 1998. Correlation between velocity dependence of friction and strain localization in large displacement experiments on feldspar, muscovite and biotite gouge. Tectonophysics 295, 15–40.
Sperrevik, S., Gillespie, P.A., Fisher, Q.J., Halvorsen, T., Knipe, R.J., 2002. Empirical estimation of fault rock properties. In: Koestler, A.G., Hunsdale, R. (Eds.), Hydrocarbon Seal Quantification. Norwegian Petroleum Society (NPF), Special Publication, vol. 11, pp. 109–125.
Turcotte, D.L., 1997. Fractals and Chaos in Geology and Geophysics. Cambridge University Press.
Underhill, J.R., Woodcock, N.H., 1987. Faulting mechanisms in high-porosity sandstones; New Red Sandstone, Arran, Scotland. In: Jones, M.E., Preston, R.M.F. (Eds.), Deformation of Sediments and Sedimentary Rocks. Geological Society Special Publication, vol. 29, pp. 91–105.
Zhang, S., Tullis, T.E., 1998. The effect of fault slip on permeability and permeability anisotropy in quartz gouge. Tectonophysics 295 (1-2), 41–52.
Zhu, W., Wong, T., 1997. The transition from brittle faulting to cataclastic flow. Journal of Geophysical Research 102 (B2), 3027–3041.

Paper 2

Rotevatn, A., **Torabi, A.**, Fossen, H., and Braathen, A., 2007. Slipped deformation bands: a new type of cataclastic deformation bands in Western Sinai, Suez Rift, Egypt. Accepted, Journal of Structural Geology.

Slipped deformation bands: a new type of cataclastic deformation bands in Western Sinai, Suez Rift, Egypt

ATLE ROTEVATN[1,2], ANITA TORABI[1,2], HAAKON FOSSEN[2] & ALVAR BRAATHEN[1,3]

[1] *Department of Earth Science, University of Bergen, Box 7800, 5020 Bergen, Norway*

[2] *Centre for Integrated Petroleum Research, University of Bergen, Box 7800, 5020 Bergen, Norway*

[3] *Now at: the University Centre in Svalbard, Box 156, 9171 Longyearbyen, Norway*

Corresponding author: atle.rotevatn@cipr.uib.no

ABSTRACT

We describe a new type of cataclastic deformation band that features a central discrete slip surface within separate, individual bands. This is unusual as slip surface development is normally constrained to the eventual brittle failure of a deformation band cluster zone due to strain hardening and sequential growth of deformation bands. The bands also lack the zone of compaction that is known to encapsulate the cores of many classical cataclastic deformation bands. Furthermore, the studied bands are thin, many less than 1 mm wide, with measured offsets of up to 230 mm, surpassing those of classical cataclastic bands by about one order of magnitude. Thin section and particle size distribution analyses demonstrate that cataclasis in the bands is intense, particularly in those that contain a central slip surface. However, petrophysical analysis demonstrates that porosities inside the bands are, in contrast to classical cataclastic bands, relatively high (9-32%). Nevertheless, permeability is reduced by up to 4.5 orders of magnitude relative to that of the host rock. This is in excess of what is previously reported from single cataclastic bands and indicate that the bands may represent baffles to fluid flow. At the same time, the central slip planes may promote along-band flow, which may have a positive effect on communication within a water or hydrocarbon reservoir.

We conclude that, unlike classical cataclastic bands, the bands of this study strain soften during their evolution. Thus, they can accumulate higher strains than classical cataclastic bands and are prone to be reactivated during progressive deformation. The bands appear to have formed under conditions close to simple-shear, following an evolution of (1) band nucleation by grain fracturing and crushing, (2) progressive

cataclasis, (3) nucleation of a central fracture, and (4) slippage along the fracture – the end result is referred to as a 'slipped deformation band'. Widespread background intragranular fracturing of the host rock and relatively high porosity in the bands are suggested as the most probable causes of deviation from traditional models for tectonic deformation in high-porosity sandstones.

INTRODUCTION

A fundamental understanding of faulting in porous media is essential for structural geologists working with the deformation of sedimentary rocks. The topic has been the subject of keen interest, partly due to its relevance in water and, particularly, hydrocarbon reservoirs (e.g. Antonellini & Aydin 1995, Hesthammer & Fossen 2001, Shipton et al. 2002). Faulted silicilastic rocks require some special considerations, as fault initiation and deformation mechanisms in highly porous rocks differ from those in low- or non-porous rocks. Of particular interest is the fact that the pore space within the rock volume facilitates some characteristic deformation processes. These include: (1) rigid grain reorganization (granular flow) resulting in compaction, dilation or isochoric strain; (2) grain fracturing/crushing (cataclasis) related to high stress concentrations at grain contact points (e.g. Antonellini et al. 1994). The resulting structural elements are generally referred to as *deformation bands* (Aydin 1978, also known as shear bands, granulation seams and microfaults) – tabular-planar deformation structures along which shear takes place.

Deformation bands differ from discrete fault surfaces in a number of ways. Primarily, they do not exhibit a discrete and continuous slip plane (grain-scale micro-fractures do however exist), but rather a shear zone of less than a few millimetres width, across which displacement is distributed. They feature offsets on a millimetre to centimetre scale, and lengths ranging from less than one to tens of metres. Single deformation bands longer than 100 metres are rare. The displacement-length ratio of (cataclastic) deformation bands may be up to three orders of magnitude larger than that of faults (Fossen & Hesthammer 1997).

Classified by deformation mechanism (following Fossen et al. 2007), there are two main types of deformation bands. One is known as *disaggregation bands* (e.g. Mandl et al. 1977, Bense et al. 2003); a sub-type of these are known as *phyllosilicate bands*

(framework phyllosilicate bands of Knipe et al. 1997). Disaggregation bands form by localized grain reorganization, but practically no grain crushing. This type of band is the most common type of band at shallow deformation depths. The other type is referred to as *cataclastic bands* (e.g. Aydin 1978, Aydin & Johnson 1983, Davis 1999), as grain crushing or cataclasis is an important mechanism. Cataclastic bands are favoured by high confining pressures (e.g. Fossen et al. 2007) and good sorting and rounding, which produce high stress concentrations at grain contact points (Gallagher et al. 1974). In simple terms, cataclasis is regarded as a common deformation mechanism in porous sandstones having undergone faulting at depths greater than 1 km (e.g. Fisher & Knipe 2001). In this work we focus on cataclastic deformation bands that differ from those described in the literature. Thus, in order to comprehend the differences appearing from the descriptions below, we first take a look at what we in the current study refer to as classical cataclastic deformation bands.

Classical cataclastic deformation bands

What is now considered the classical work on cataclastic deformation bands was carried out in the Entrada and Navajo Sandstones of southern Utah by Aydin (1978). Microstructurally, Aydin described the cataclastic deformation bands as 0.5 mm thick zones of grain crushing encapsulated in a zone of compaction and grain reorganization. Aydin and Johnson (1978) also presented a three-stage model for faulting in porous sandstones: (1) nucleation and growth of an individual deformation band, (2) formation of multiple deformation bands (cluster zones) due to strain hardening, and (3) the breakthrough of a continuous slip surface in the cluster zone. It is important to notice that slip surfaces in these rocks only occurs after the accumulation 10s or 100s of bands in a decimetre to metre thick zone. The findings of Aydin (1978) and Aydin & Johnson (1978) have later been supported by a number of field based studies, both from the same rock units (Antonellini & Aydin 1995, Fossen & Hesthammer 1998, Davis 1999, Davatzes & Aydin 2003, Shipton & Cowie 2003, Johansen & Fossen *in press*), and from similar rock units in the western USA (Jamison & Stearns 1982, Sternlof et al. 2004), Great Britain (Underhill & Woodcock 1987, Edwards et al. 1993, Beach et al. 1997), the North Sea (Hesthammer & Fossen, 2001) and numerous other places. Furthermore, experimental work gives additional support to their model (e.g. Mair et al. 2000, Lothe et al. 2002).

Previous work has established that deformation bands can alter the effective permeability of highly porous sandstones (e.g. Sternlof et al. 2004). For cataclastic deformation bands of the type studied by Aydin and others (e.g. Aydin 1978, Aydin & Johnson 1978, Aydin & Johnson 1983, Antonellini et al. 1994), the permeability measured across a single deformation band can be reduced by several orders of magnitude relative to that of an adjacent undeformed sample, with the greatest reductions occurring in the most permeable sandstones. Some of the published data (e.g. Antonellini & Aydin 1994, Fisher & Knipe 2001) indicate permeability contrasts of up to 6 orders of magnitude, while others report lower values (Taylor & Pollard 2000). One reason for the locally high contrast reported by some authors is that permeability has been measured across multiple deformation bands, and a distinction between single and multiple bands are generally not made in published data sets. According to our own field data from localities in Utah (see discussion and figures therein), most single cataclastic deformation bands have a permeability 0-3 orders of magnitude lower than the adjacent host rock. The permeability reduction is due to the significant changes in porosity, pore-throat geometry and pore connectivity caused by grain crushing and reorganization.

The current study is based on outcrops of faulted pre-rift sandstones in the eastern flank of the late Oligocene to early Miocene Suez rift, in the Western Sinai Peninsula, Egypt (Fig. 1). In this area we identified and investigated a type of cataclastic deformation bands that seem incompatible with the classical bands described by Aydin (1978) and others. In particular, they do not comply with Aydin and Johnson's (1978) model, where a cluster of deformation bands is formed before the formation of a slip plane. Instead, the deformation bands described in this paper develop internal central slip planes within far-apart individual deformation bands that are unrelated to deformation band cluster zones. This study undertakes an investigation of these deformation bands, and seeks to:

1. document and describe their geometry and structural characteristics;
2. measure and assess their petrophysical properties and potential effect on fluid flow;
3. discuss how these deformation bands may have formed, and why they deviate from the classical model for fault initiation in porous sandstones.

GEOLOGICAL SETTING

The Suez Rift is an aborted arm of the Red Sea rift system, forming a NW-SE trending basin, c. 300 km long and c. 80 km wide, separating the Sinai micro-plate from the African plate (Fig. 1a, e.g. Garfunkel & Bartov 1977, Lyberis 1988, Bosworth et al. 2005). The main phase of rifting occurred during the separation of the African and Arabian plates from the latest Oligocene until its termination in the Miocene (c. 24 – 15.5 Ma). Termination of rifting relates to initiation of the Dead Sea–Aqaba transform, which accommodates continued extension in the Red Sea rift (Cochran 1983). The Suez rift is characterized by classical rift geometries featuring half-grabens and rotated normal fault blocks (e.g. Moustafa 1993, Jackson et al. 2006). The current work is based on outcrop studies along extensional faults in the eastern shoulder of the Suez Rift, c. 1.5 km into the footwall of the rift-bounding Thal Fault (Fig. 1), as described by Sharp et al. (2000). Deformation bands in the Nubian Sandstone of the hangingwall and footwall of these faults are the focus of this study. The term *Nubian Sandstone* (Shukri 1945) refers to a regionally extensive succession of Cambrian to Early Cretaceous sandstones in the NE African region (e.g. Bosworth 1995). In Sinai, the Nubian Sandstone comprises predominantly non-marine fluvial sands, with a few marginal marine and aeolian interbeds (e.g. Gupta et al. 1999). At the localities featured in this study they are mainly fluvial. The maximum burial depth of the stratigraphic level of the study area at the time of faulting is about 1.5 km (Du Bernard et al. 2002).

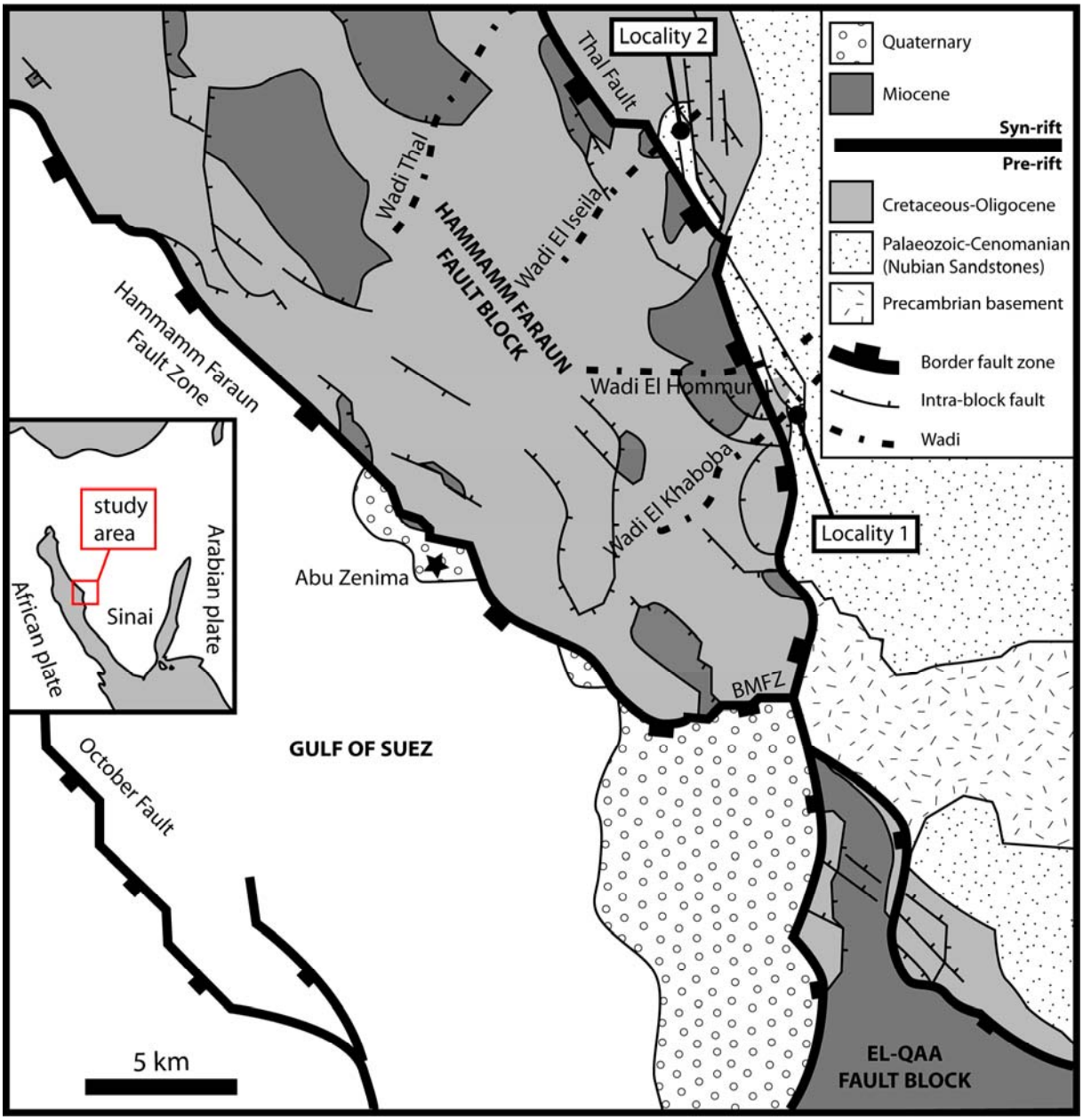

Fig. 1. Structural map of the Hammam Faraun fault block and surrounding areas. The localities of the current study are indicated. Based on Moustafa (1993), Sharp et al. (2000) and Jackson et al. (2006).

FIELD DATA AND RESULTS

Localities and field methods

We focus on two localities, at which a large number of deformation bands were examined. Both localities are found NE of the Hammamm Faraun fault block, along extensional faults that probably formed coevally with the larger Thal Fault. At both localities, the Nubian Sandstone comprises the hangingwall and footwall of the extensional faults.

At locality 1 (Wadi El Khaboba; Fig. 1) a NW striking fault displays an offset of c. 15 m; the sense of slip is normal, with a small sinistral strike-slip component. The fault core is characterized by a 5-15 cm thick zone of cataclasites derived from sandstones in the hangingwall and footwall, encapsulated by a 30-100 cm thick zone with a very high density of anastomosing cataclastic deformation bands. Several discrete slip planes in the core accommodate the majority of fault displacement. The studied deformation bands are found in the damage zone (Fig. 2) of this fault, c. 1-30 m away from the fault core.

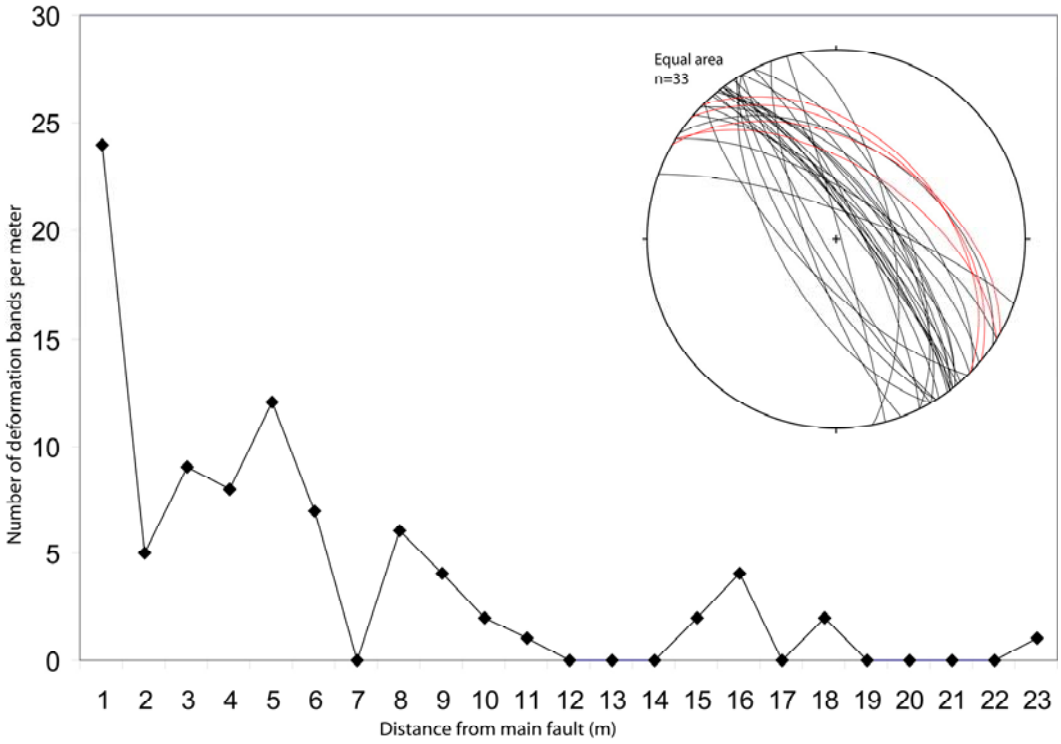

Fig. 2. Damage zone profile from locality 1 in Wadi el Khaboba. The structure frequency profile records the number of deformation bands per metre against distance from main fault. The equal area stereo net shows that the bands (black great circles) strike sub-parallel to the main fault (red great circles) and thus are related to its formation.

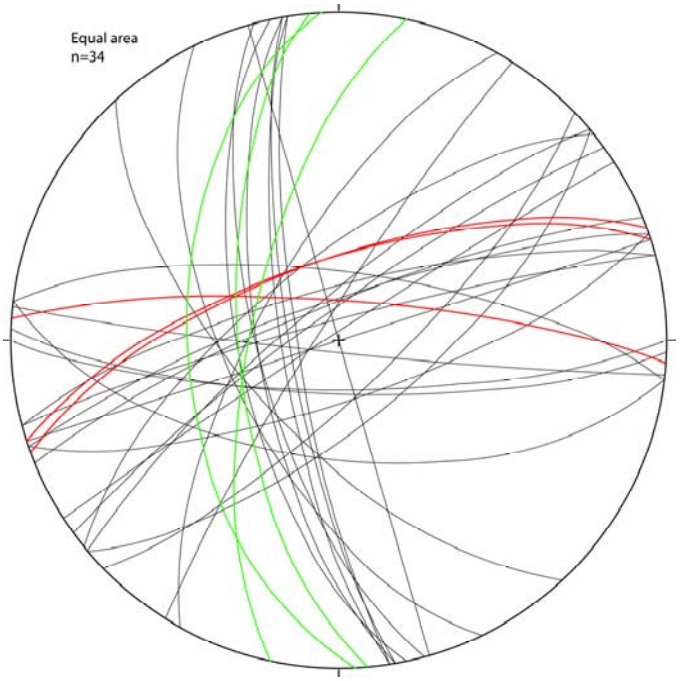

Fig. 3. Equal area stereo net showing the orientation of deformation bands and faults at locality 2 in Wadi El Iseilat. The largest fault in the area is plotted as red great circles. The smaller but, for the studied outcrop, closer and more influential fault is plotted as green great circles. Black great circles represent deformation bands.

At locality 2 (Wadi El Iseila; Fig. 1), there are two faults affecting the Nubian Sandstone (Fig. 3). The largest fault strikes WSW and has an offset of c. 150 metres. The studied outcrop is 150-200 metres into the footwall of this fault. There is also another smaller, but, for the studied outcrop, more influential fault, striking S with an offset of c. 15 m. This fault features a c. 1.2 m thick core comprising a c. 30 cm thick cataclasite, and a c. 90 cm thick zone of anastomosing deformation bands, displaying ladder and fishnet geometries (Davis 1999, Schultz & Balasko 2003). As on the previous locality, several discrete slip surfaces in the fault core have accommodated most of the fault displacement. The studied deformation bands are located 5-30 metres into the hangingwall of the latter fault.

As the lithology and deformation bands at the two localities are very similar, we will not differentiate between the localities in the following, but treat them as one. Numerous deformation bands were identified and recorded in the damage zones of the main faults, the results of which are outlined below. Basic field methods were applied: compass, measuring tape and GPS were used to record orientations, offsets, thicknesses, spatial relationships and positioning. Furthermore, a mini-permeameter was used to collect permeability data, and samples for thin sections and laboratory analysis of petrophysical properties were collected.

Host rock

The host rock at both localities is fluvial sandstone from the Jurassic to Early Cretaceous Malha Formation (Abdallah & El Adindani 1963) of the Nubian Sandstone succession. Grain sizes vary from medium to very coarse sand, and the stratigraphic units feature well preserved cross-stratification. The host rock is very loose, which may partly be a result of weathering, but largely a result of poor consolidation. The latter is common for sandstones at shallow burial depths, which may be relatively loose and friable at burial depths down to 2.5-3 km (Bjørlykke & Egeberg 1993). Thin sections confirm only minor effects of burial diagenesis (Fig. 4a). Dissolution has occurred at some grain contacts but is not abundant. Cementation is practically non-existent, consistent with the shallow (~1.5 km) burial depths that the Nubian Sandstone has experienced in this area; quartz cementation occurs mainly at temperatures in excess of 90 °C (Walderhaug, 1996) or at depths in excess of 3.5 km (Bjørlykke & Høeg 1997). Grain fracturing, however, is widespread in the host rock (Fig. 4b), particularly in coarse-grained sandstone layers. The degree to which grains are affected by fracturing varies from single fractures to complete grain breakdown. Grain fracturing is laterally relatively uniform within layers of similar grain size, but is in some thin sections seen to increase in intensity near the deformation bands.

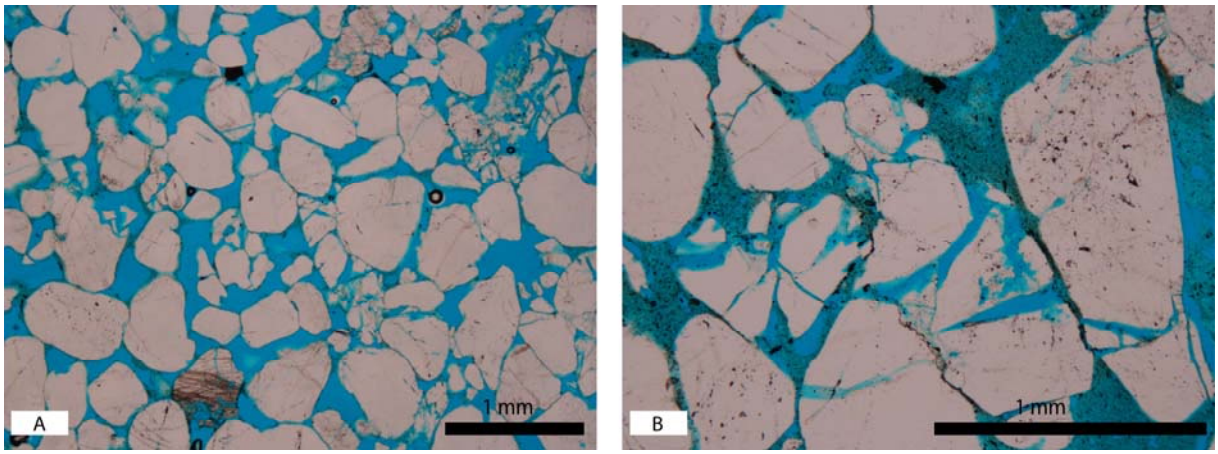

Fig. 4. Photomicrographs of host rock samples. Note that grain fracturing is abundant.

Deformation bands in the field

The deformation bands observed in the current study (referred to as Sinai bands in the following) display characteristics that are both similar and different from classical cataclastic deformation bands (CCDB). The bands are recognized as cataclastic deformation bands based on three criteria: 1) Displacement is detectable and on a mm to cm scale; 2) displacement is accommodated in a mm-thick, white coloured shear zone; 3) in the thin zone of shearing, grain size reduction is detectable by eye or hand lens, and further confirmed by thin section analysis and SEM images (see below). Although these criteria match those of CCDB, the Sinai deformation bands display other characteristics that are not compatible with CCDB. Most notably, many of the deformation bands feature slip planes within widely spaced individual bands that are not associated with deformation band clusters (Fig. 5). Deformation bands without slip surfaces were also identified, and the following visual subdivision was made in the field: 1) deformation bands with no visible fracture- or slip plane (Fig. 6a); 2) deformation bands with a visible central fracture (Fig. 6d); 3) deformation bands featuring a central fracture with visible slickenlines (Fig. 6g). The fracture planes and slip planes seen in some of the deformation bands were of varying continuity, ranging from patchy cm-scale occurrences to completely continuous along much of the strike of the deformation band (Figs. 6d and 6g).

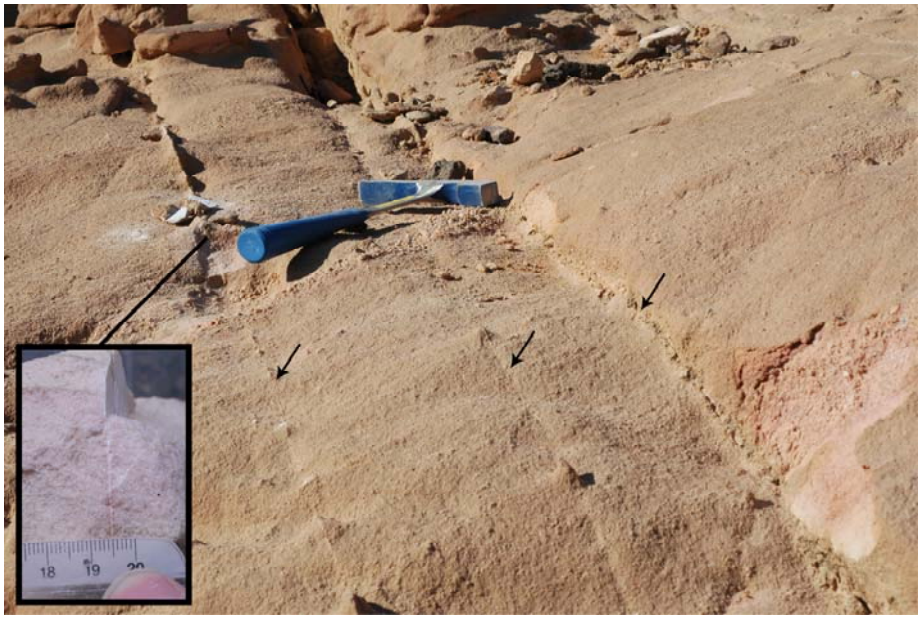

Fig. 5. Picture from the studied outcrop at locality one showing three individual deformation bands (indicated by arrows), all of which feature central slip planes. The inset shows a hand specimen taken from one of the deformation bands, where the slip plane is clearly visible. The scale bar on the inset is in centimetres.

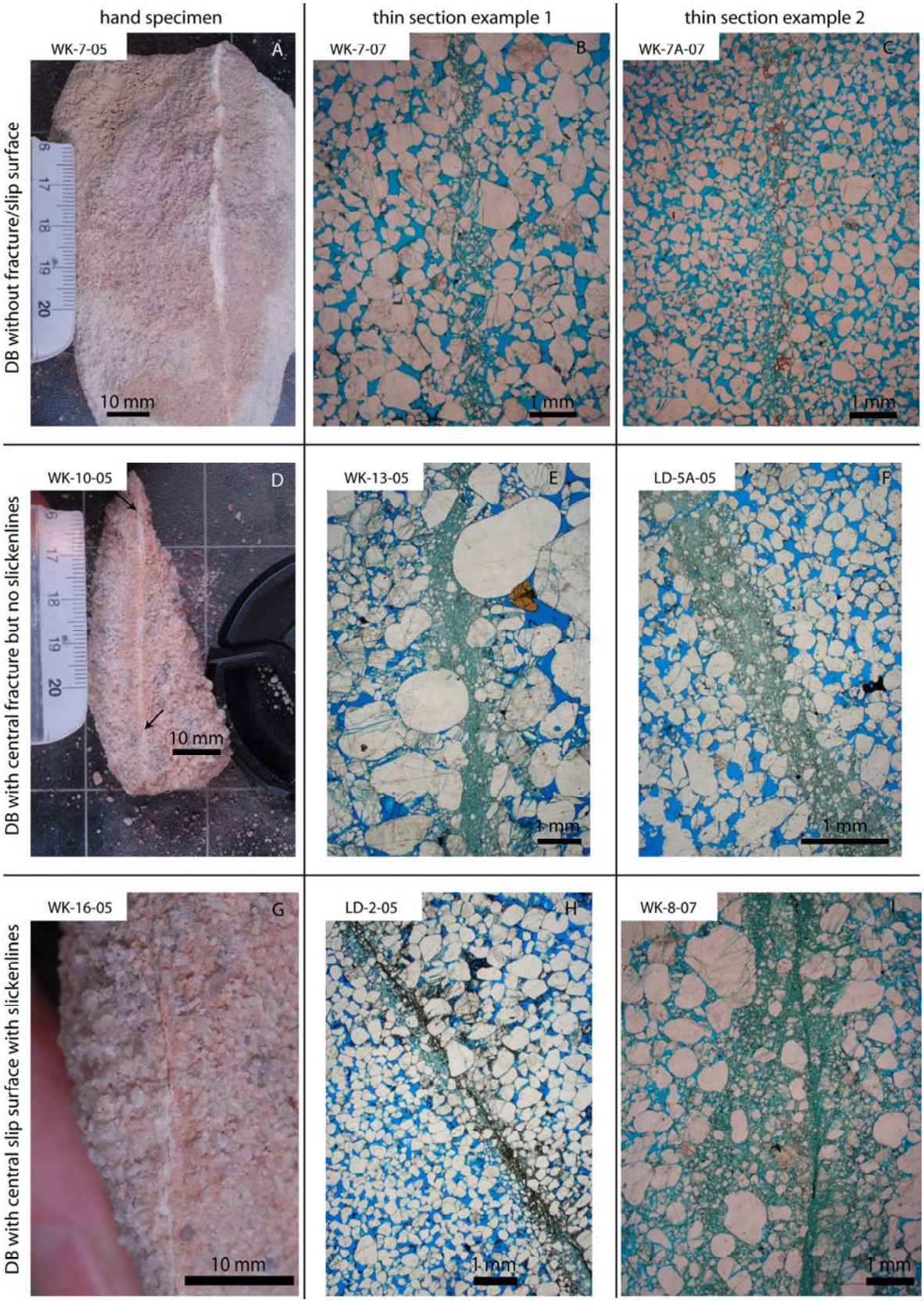

Fig. 6. Field photos and photomicrographs of deformation band samples collected in the field. **(a-c)** Deformation bands without fracture/slip surface. **(d-f)** Deformation bands with a central fracture but no slickenlines. **(g-i)** Deformation bands with a central slip surface with slickenlines.

Offset and thickness

The studied deformation bands feature thicknesses similar to or slightly less than CCDB (Fig. 7), the mean thickness of the bands being 0.8 mm (Table 1). Offsets are larger than those known for CCDB, the maximum offset recorded being 230 mm and the mean offset being 21 mm (Table 1). There is no strong correlation between offset and thickness, which is typical for cataclastic deformation bands. The thickness of the Sinai bands remains stably at around 0.8 mm for most bands, regardless of the amount of offset. However, the Sinai data indicate a correlation between the amount of offset and the development and growth of a central slip surface. Where the offset is less than c. 15 mm there is a mix of bands with no slip plane, bands with fracture planes but no slickenlines and bands with slip planes featuring slickenlines. Where offset exceeds c. 15 mm however, practically all bands feature slip planes with slickenlines (Fig. 7). It thus appears that beyond this value, displacement is no longer accommodated by cataclastic shear, but rather accommodated by slip along a discrete slip surface.

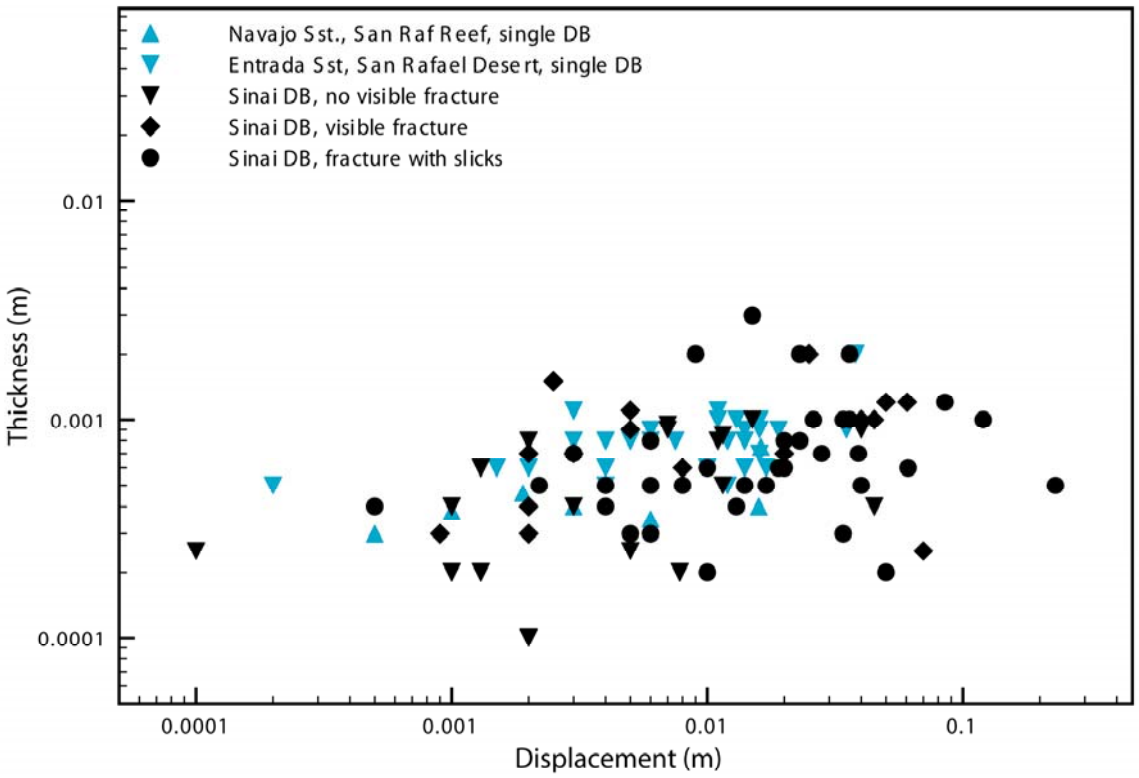

Fig. 7. Log-log plot of displacement versus thickness of deformation bands. Three series of field measurements from Sinai are plotted: Deformation bands with no fracture plane, deformation bands with a central fracture but no slickenlines, and deformation bands with a central slip plane with slickenlines. In

addition, two series from Utah (unpublished) are plotted, from the Navajo Sandstone and the Entrada Sandstone, respectively.

Table 1. *Mean offset and mean thickness of deformation bands.Only bands were both offset* and *thickness were successfully recorded are included.*

Deformation band population	n*	mean offset (mm)	mean thickness (mm)
Def. bands without central fracture	27	7.9	0.6
Def. bands with central fracture but no slickenlines	16	21.3	0.9
Def. bands with central slip surface with slickenlines	39	29.9	0.8
Total	*82*	*21.0*	*0.8*

* n = number of measurements

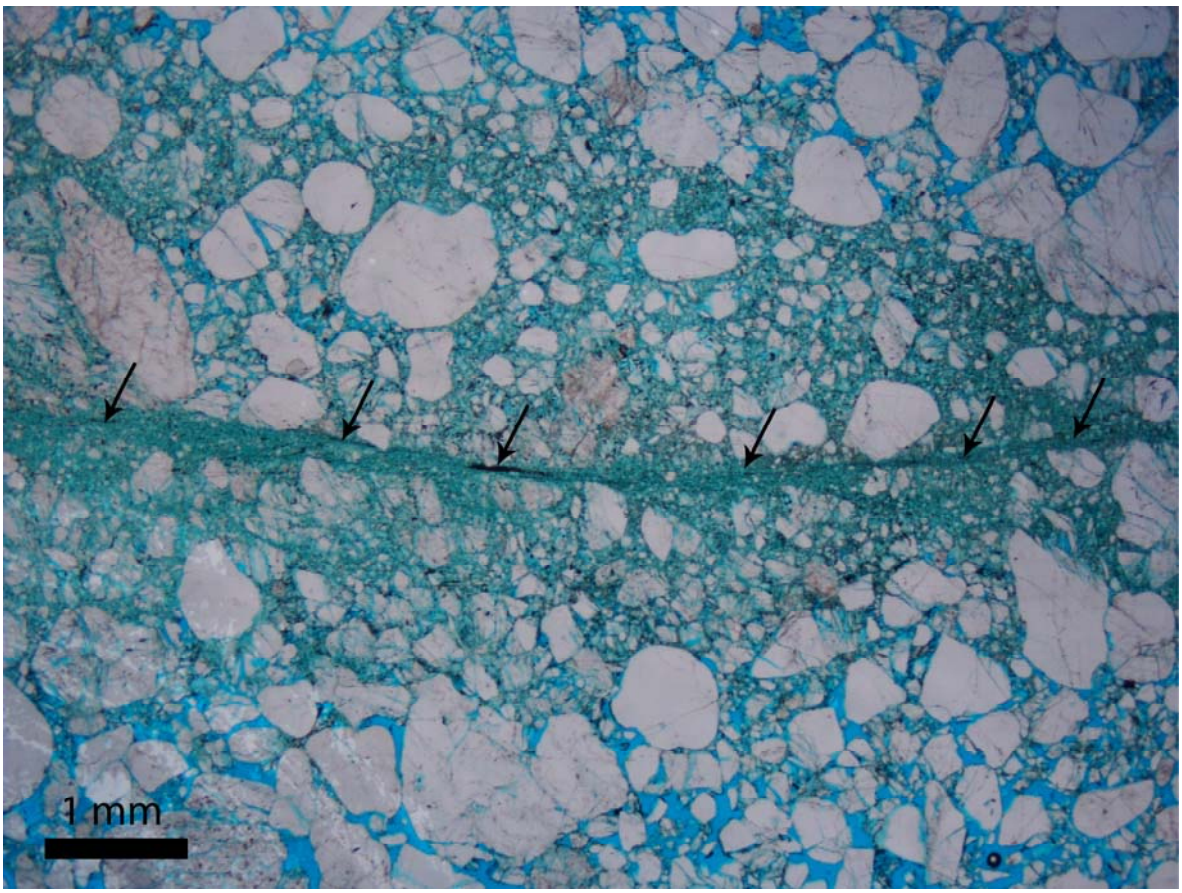

Fig. 8. Thin section of slipped deformation band showing severe crushing near the slip surface, indicated by arrows.

Fig. 9 (opposite). Results from statistical analysis of particle size distribution obtained from Backscattered Electron images (BSE). Log EF (exceedence frequency) is plotted against log PSA (particle size area). **(a-d)** Deformation bands with no visible fracture. **(e-h)** Deformation bands with a central fracture. All of these, except **(e)**, feature visible slickenlines.

Deformation bands without fracture/slip surface

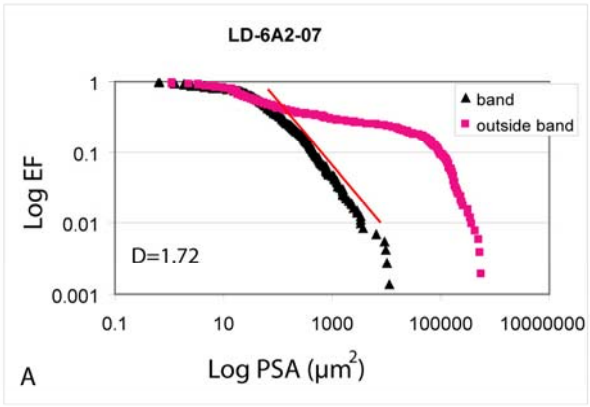

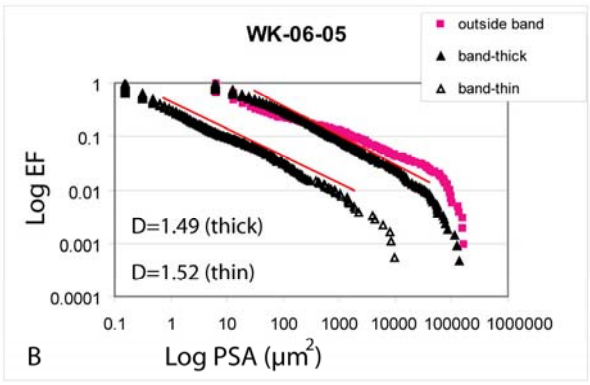

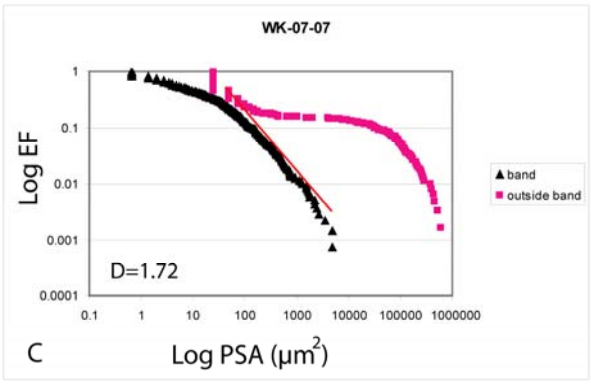

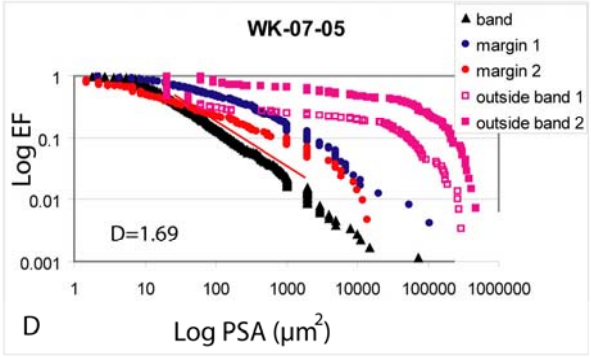

Deformation bands with central slip plane

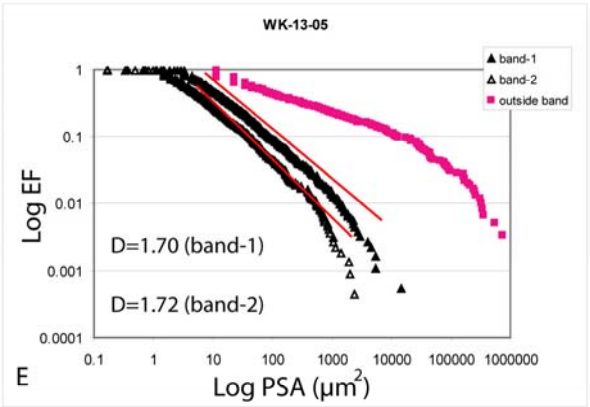

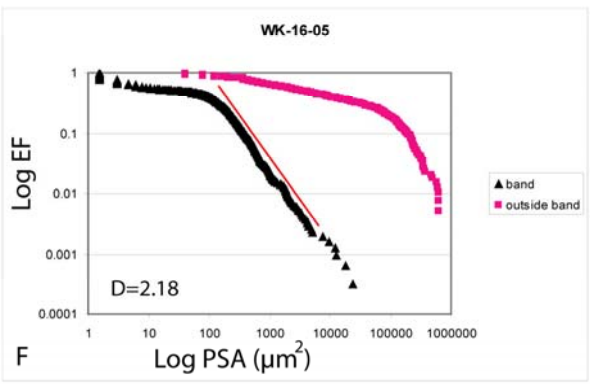

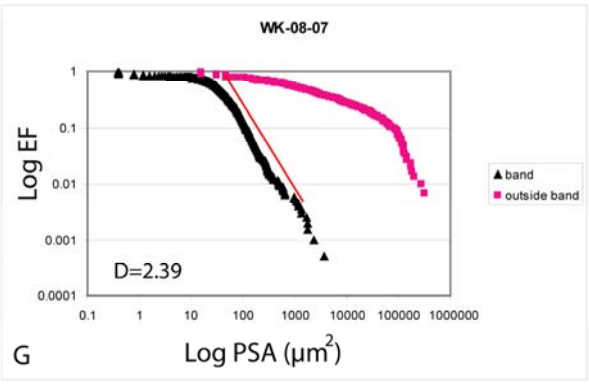

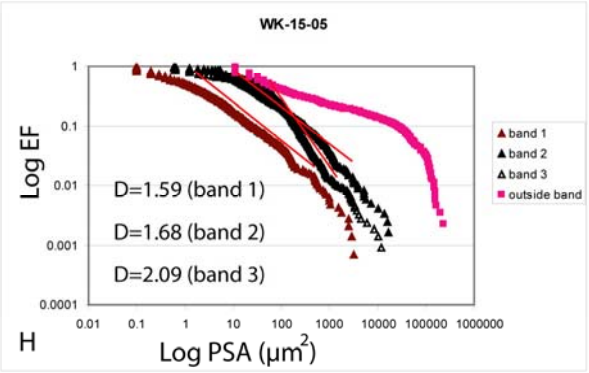

Cataclasis and grain size distribution

The cataclastic cores of the bands in the current study exhibit grain crushing ranging from mild grain breakdown to extremely intense cataclasis (Fig. 6). The most intense grain crushing is observed in bands containing a central fracture- or slip surface (Fig. 8). This is supported by statistical analysis of particle size distribution obtained from Backscattered Electron images (BSE) using image processing methods (Torabi et al. 2007).

The results are presented graphically in Fig. 9, where plots of log EF vs. log particle size areas (PSA) have been investigated. Exceedence Frequency (EF) of a particular value of a measured variable is defined as the number of data with values greater than that value, divided by the total number of the data. In each of the examined thin sections, images of the host rock outside of the band as well as the band itself have been investigated. The particle size distribution plots show that, for all of the analysed samples, there is a reduction of grain size in the bands relative to the host rock. The kinked or curved appearance of most host rock particle size distribution plots are different from the straight lines or curves with straight central segments seen in the deformation band particle size distribution plots. This is typical of cataclastically deformed sand (e.g. Sammis et al. 1987). In these cases the particle size distribution of the bands can be described by a power law with dimension *D* (exponent). The calculated two-dimensional *D* can be converted to the third dimension by adding 1 (Sammis et al. 1987, Blenkinsop 1991, Torabi et al. 2007). The value of the three-dimensional D is presented in table 2.

Table 2. *Deformation band particle size distribution data.Note that for some thin sections, multiple bands were analyzed.*

Sample no.	n	D	R^2	slip surface
LD-6A2-07	732	1.72	0.9824	no
WK-06-05 thick band	2183	1.49	0.9715	no
WK-06-05 thin band	1815	1.52	0.9896	no
WK-07-07	1400	1.72	0.9734	no
WK-07-05	1715	1.69	0.9668	no
WK-13-05 band1	1867	1.7	0.9954	fracture, no SL
WK-13-05 band2	2258	1.72	0.9927	fracture, no SL
WK-16-05	3164	2.18	0.9696	yes
WK-08-07	2048	2.39	0.9772	yes
WK-15-05 band1	1450	1.59	0.9926	uncertain
WK-15-05 band2	1217	1.68	0.981	uncertain
WK-15-05 band3	2172	2.09	0.9864	yes

n denotes the number of data points (measured grains) for each sample. *D* is the 3D power law dimension (or simply D-value).
R^2 is the coefficient of determination, indicating the power law fit to the particle size distribution (where 0 is no fit and 1 is a perfect fit).

Particle size distribution plots from the margin of the deformation bands show distributions intermediate between those of the host rock and the band (Fig. 9 d, h). In general, there is a positive correlation between the value of D and the intensity of cataclasis: high D-values indicate strong cataclasis. The bands hosting a central slip plane feature the highest D values (2.09-2.39) and thus have undergone the most intense cataclasis (Table 2). Nevertheless, there are still some unbroken large grains in many of the bands (Fig. 6h). The intensity of the cataclasis is lower in the bands without a central slip surface (D=1.49-1.72) than in those containing slip surfaces (Fig 6 and 9, table 2). Bands with the least intense cataclasis, i.e. where the grain breakdown is mild and limited, appear to have undergone much less deformation and are thus labelled *incipient bands* (Fig. 10). These are bands that do not host a central fracture- or slip surface. The relationship between these incipient bands and more mature bands will be addressed further in the discussion.

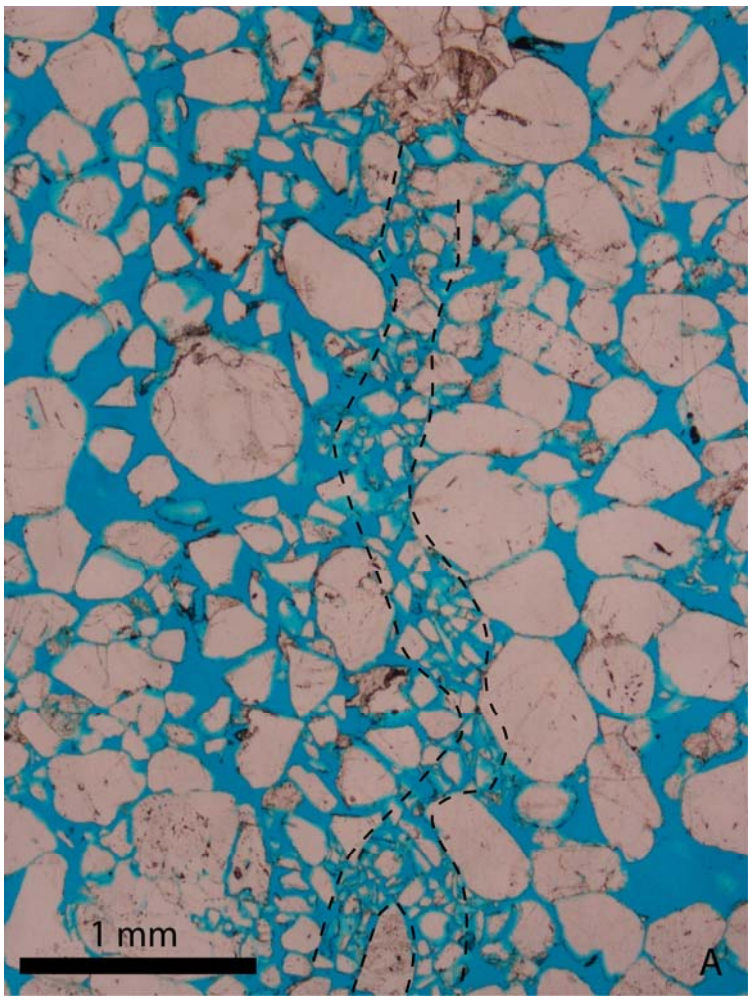

Fig. 10. Photomicrograph of incipient deformation band. Incipient deformation bands represent the earliest stage of development for the studied deformation bands.

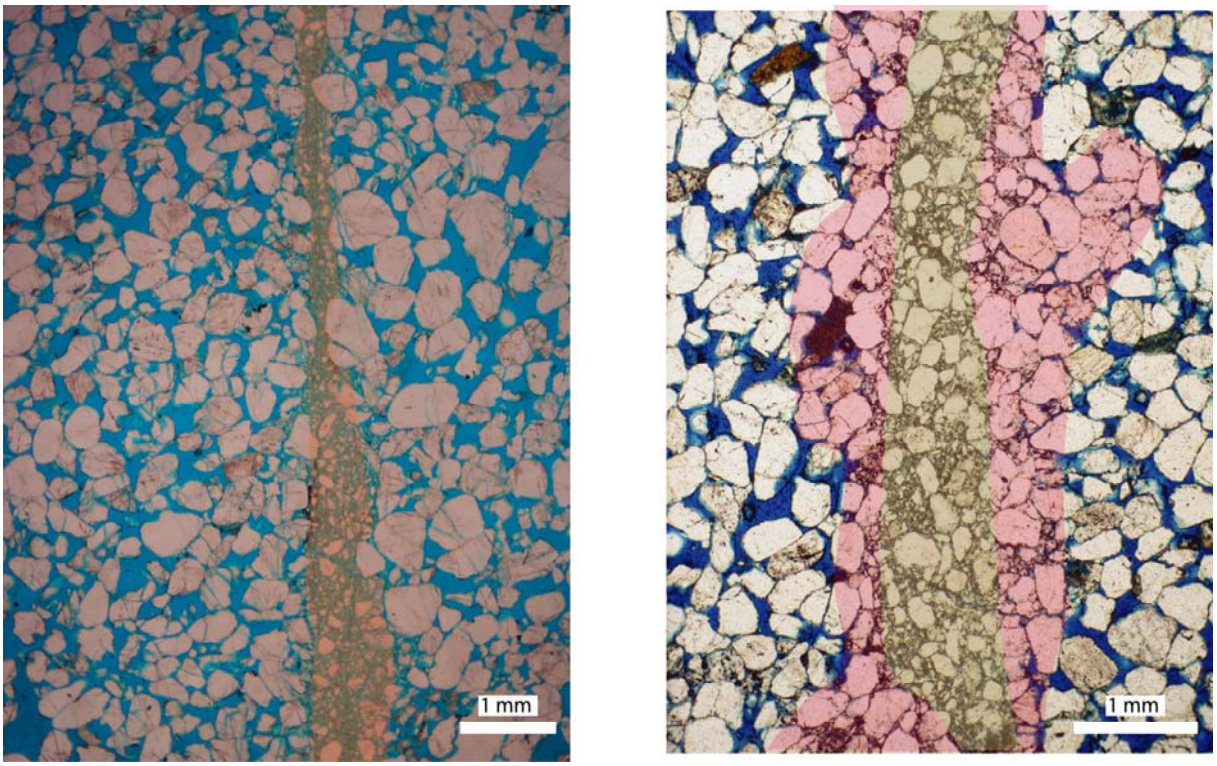

Fig. 11. (a) Photomicrograph showing typical deformation band architecture of the bands in the current study. Note that there is a cataclastic core, but no surrounding compactional envelope. **(b)** Architecture of a classical cataclastic deformation band with a cataclastic core and a zone of compaction enveloping the core. This photomicrograph is from the Navajo Sandstone in Utah, and is modified from Fossen and Gabrielsen (2005).

Architecture

The core of classical cataclastic deformation bands is known to be encapsulated in a zone of compaction and grain reorganization (Aydin 1978). However, the bands in the current study feature no such zone of compaction (Fig. 11). Instead the bands display a sharp transition between undeformed host rock and the cataclastic core. The transition is sharpest across bands that contain a central slip plane, as the cataclasis is most intense here.

The slip surfaces themselves are easy to identify as discontinuities within the cataclastic core of the band (Fig. 6i). Most slip surfaces do not appear as open fractures in thin section. However, precipitated black minerals (probably iron oxides and/or

hydroxides, Fig. 12) provide evidence for palaeo-fluid flow and precipitation along the slip surfaces.

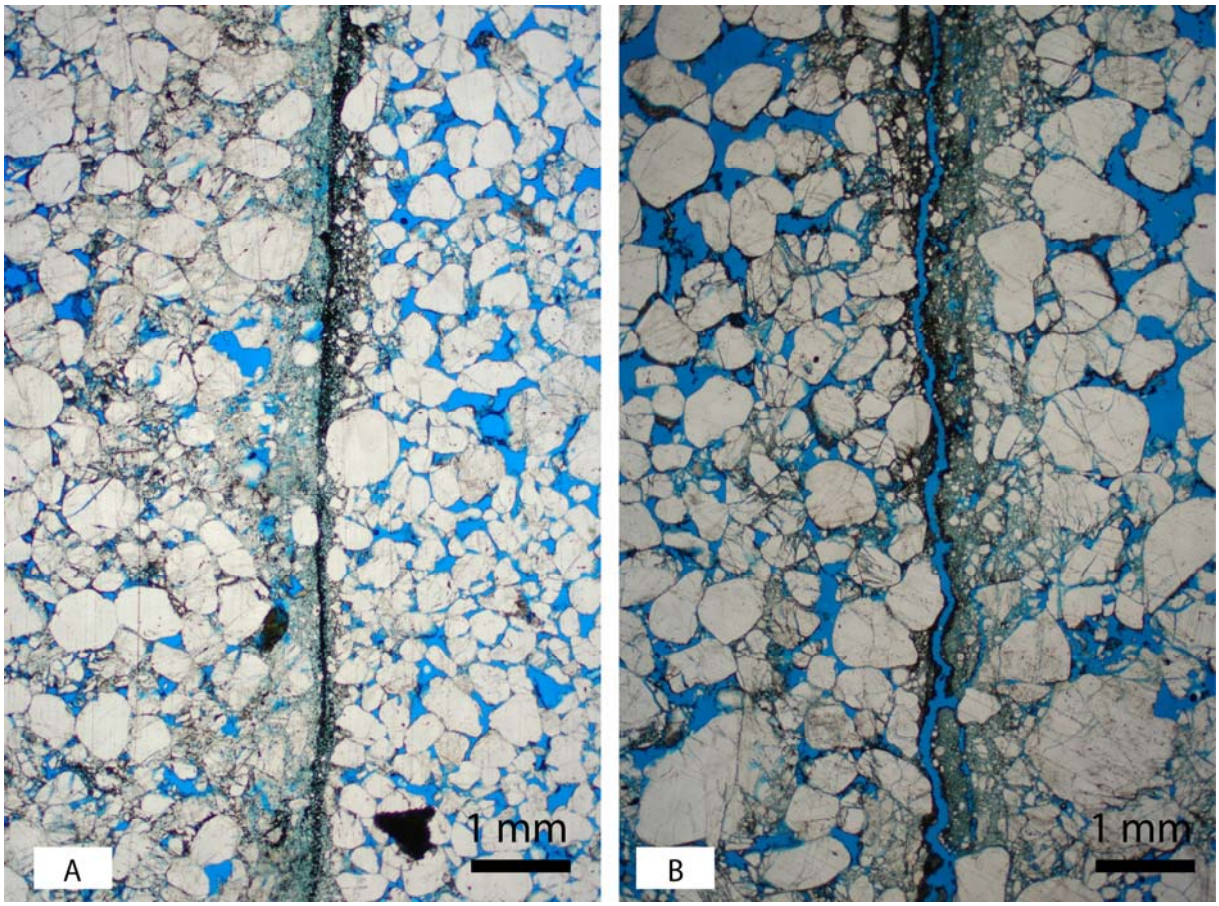

Fig. 12. Photomicrographs of deformation bands hosting a central slip surface with slickenlines. Note the black precipitated minerals (probably ferric oxides) in the centre of the bands, which we interpret as evidence for palaeo-fluid flow in along the slip surfaces.

PETROPHYSICAL PROPERTIES

Methods

Porosity and permeability measurements have been carried out using different field-, laboratory- and image analysis techniques. For porosity, image analysis techniques using optical microscopy for host rock samples and SEM imagery for deformation band samples were applied (see Appendix A for details). A total of 44 porosity determinations using this technique were conducted on a selection of thin sections from collected hand samples. Eleven of these were host rock thin sections and

33 thin sections with deformation bands. In addition to this, one sample was analysed at ResLab Reservoir Laboratories in Stavanger, Norway, where helium porosity by Boyle's law technique was determined (see Appendix A for details).

For permeability, a combination of mini-permeameter field measurements and laboratory experiments were applied. The laboratory measurements were conducted at ResLab Reservoir Laboratories, determining the Klinkenberg-corrected gas permeability (Klinkenberg 1941) by the steady state technique (see Appendix A for details). Eight core plugs, drilled and sampled in the field, were analyzed using this method. Of these, 2 were host rock samples, 2 were samples with single bands with slip surface and 4 were samples taken from slip surfaces along the main fault in locality 1. In addition to this, measurements were conducted in the field using a TinyPerm II Portable Air Permeameter (mini-permeameter) manufactured by New England Research (see Appendix A for details). Permeabilities from 43 sample locations in the field were determined using this method. Of these were 8 host rock, 10 bands with no slip surface, 5 bands with fracture plane but no visible slickenlines, and 20 bands hosting a slip surface with slickenlines.

Porosity

The results from the porosity determinations are shown in Fig. 13. The data are organized by type of sample: host rock, incipient bands, bands without slip surface and bands with a central slip surface.

The data show that host rock porosity and porosity of incipient bands fall within approximately the same range of values (21-35% for host rock samples and 24-35% for incipient bands). This is in agreement with observations from thin sections (Fig. 10), which show that porosity is relatively unchanged in such bands. However, the populations of deformation bands *without* and *with* slip surfaces, fall within a relatively lower range of porosity values (10-26% and 9-32%, respectively), although there is overlap with host rock and incipient band porosities. The large variations of porosity values within the deformation bands are probably explained by differences in amount and localization of cataclasis in the bands. For one of the samples, a porosity profile across a deformation band (featuring a central slip surface) was made (Fig. 14). The profile shows a porosity drop across a band from the host rock, via the margin to the

centre of the cataclastic core. However, porosity in the bands is surprisingly high (lowest value being 9%) when compared with other studies of cataclastic deformation bands (Fig. 13). The implications of this are addressed in the discussion.

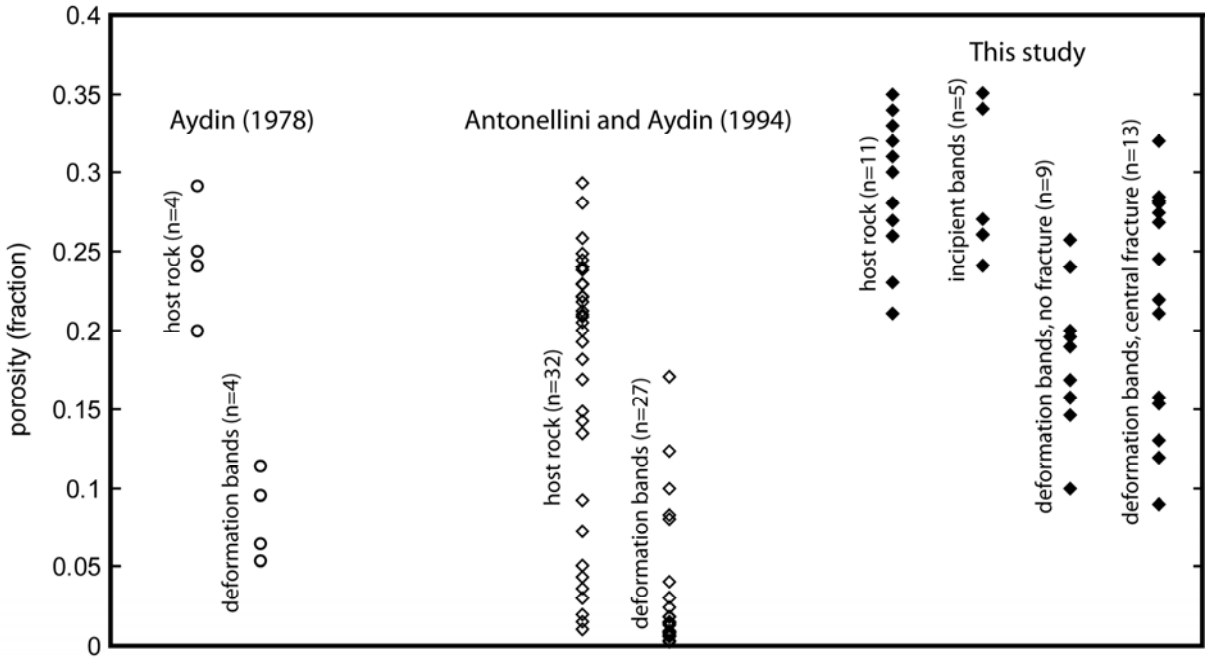

Fig. 13. Porosity data for deformation bands of the current study compared to data from Aydin (1978) and Antonellini and Aydin (1994).

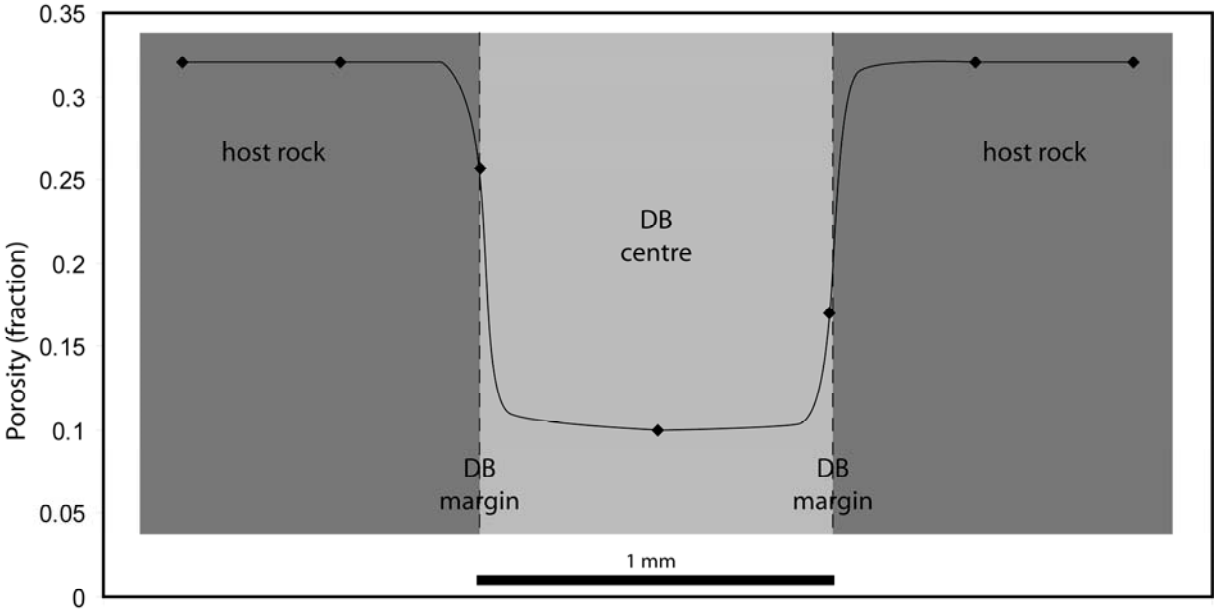

Fig. 14. Porosity profile across a single cataclastic deformation band. The geometry of the extrapolation curve between data points is inferred from thin section studies, which indicate abrupt transitions in grain size from host rock to deformation band.

Permeability

Permeability results from laboratory and mini-permeameter measurements are shown in Fig. 15. The results are separated according to sample type: host rock, bands with no visible fracture, bands with a visible central fracture but no slickenlines, and, finally, bands hosting a central slip surface with slickenlines. In addition, a population of laboratory measurements from main fault slip surfaces at locality 1 is shown. Incipient bands have not been tested for permeability due to difficulties excavating a surface suitable for mini-permeameter measurements. Furthermore, samples of incipient bands for laboratory determination of permeability were too loose to be fit for analysis. All measurements represent permeability of flow *across* the band. Band-parallel permeability was not measured.

The permeametry data reveal a distinctly reduced permeability in all bands relative to the host rock. The host rock permeability values range from 4000 to 53000 mD with a mean of 13000 mD. These values are extremely high and probably inaccurate due to the mini-permeameter's limitations in resolving permeabilities above 10000 mD. However, note that the laboratory measurements fall within the range of the mini-permeameter measurements. We therefore consider the measured values to be sufficiently accurate for

comparative purposes. The different types of bands feature permeability values 1.5 to 4.5 orders of magnitude lower than those of the host rock. Deformation bands without any fracture- or slip surface display permeability values between 13.7 mD and 64.3 mD, with a mean of 31.1 mD. The bands with a central fracture but no slickenlines fall within the range of 4.0-26.2 mD, with a mean of 14.6 mD. Finally, the bands hosting a central slip plane with slickenlines display permeabilities of 1.7 to 22.1 mD, with a mean of 7 mD. Hence, there is an increase in permeability contrast (relative to the host rock) from bands with no fracture development (1.5 to 3.5 orders of magnitude), via bands with a central fracture but no slickenlines (2 to 4 orders of magnitude), to bands with a central slip surface with slickenlines (up to 4.5 orders of magnitude). A permeability reduction of 1.5 to 4.5 orders of magnitude is within the high range of our own and previously published data for deformation band permeability (see Fig. 16 and e.g. Antonellini & Aydin 1994, Ahlgren 2001, Fisher & Knipe 2001, Lothe et al. 2002). Mini-permeameter measurements of slip planes in the core of the main fault at locality 1 record a lower permeability reduction of approximately 1.5-2.5 orders of magnitude.

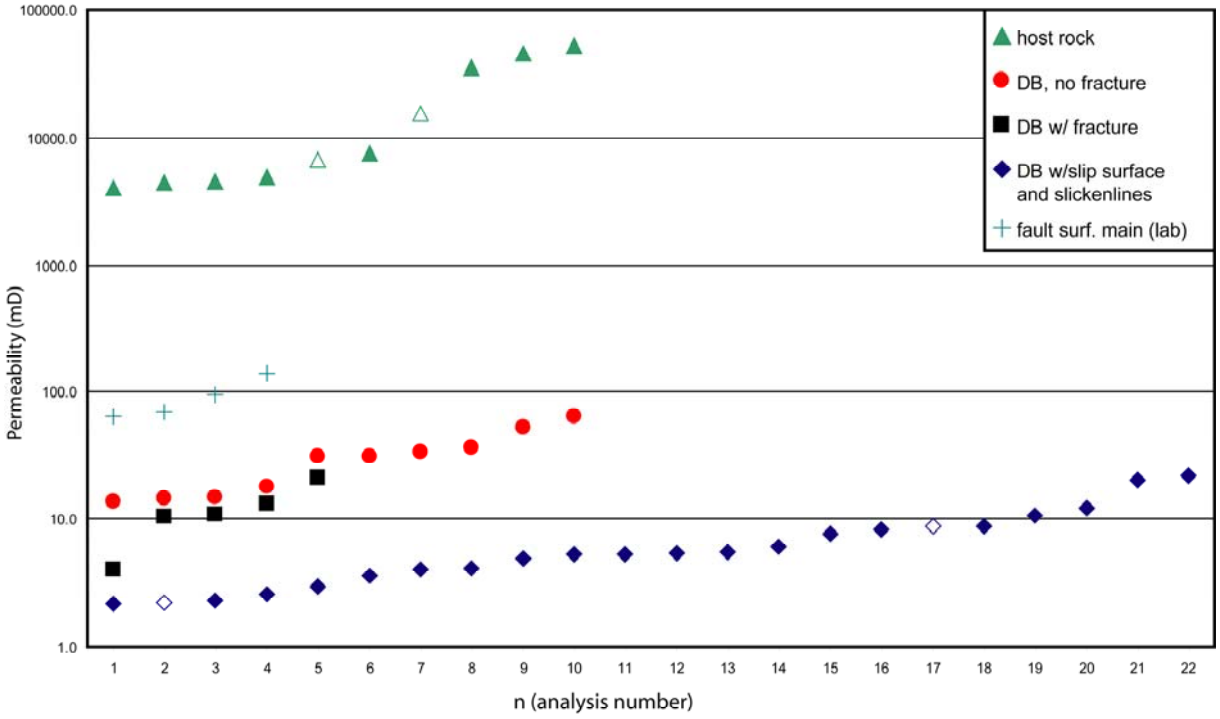

Fig. 15. Deformation band permeability data. Open data points indicate laboratory measurements of permeability, whereas the filled points are mini-permeameter measurements. See text for details.

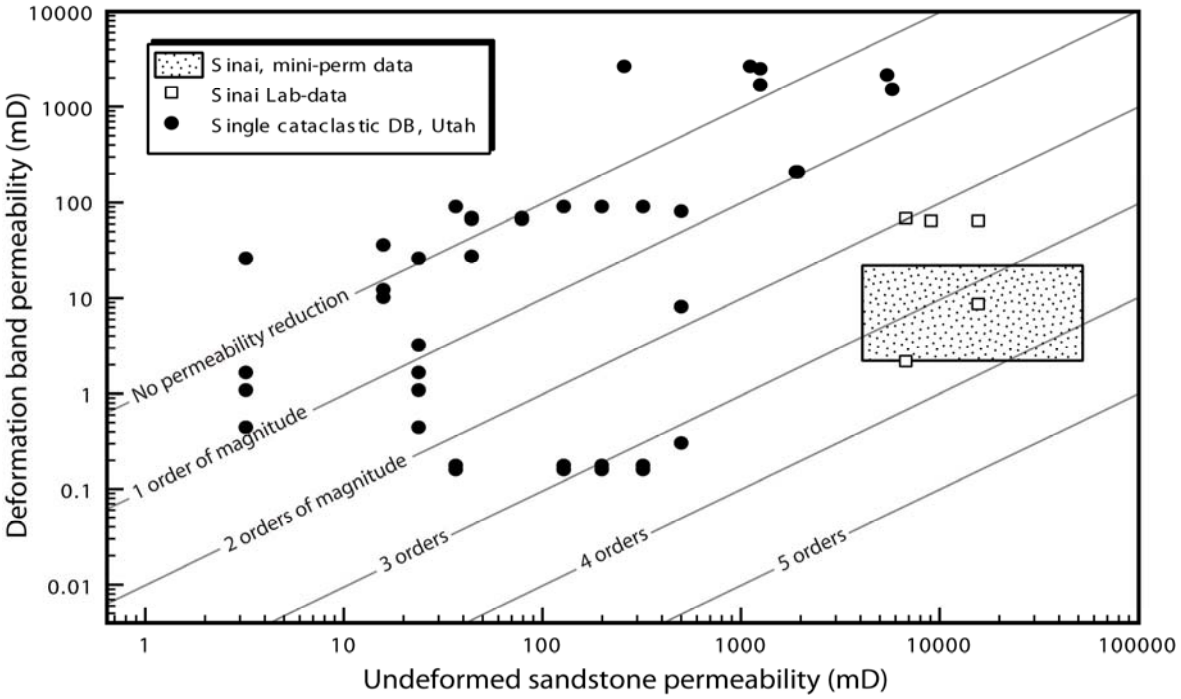

Fig. 16. Permeability contrast data from the current study (bands with central slip surface) plotted together with our own data from single deformation bands (CCDB) in Utah (unpublished).

Table 3. *Comparative properties of classical cataclastic deformation bands and the Sinai bands.*

Criteria	Classical bands	Sinai bands
Similarities		
appearance in outcrop	white streaks	white streaks
thickness	very thin, mostly ~1 mm	very thin, mostly ≤1mm
displacement	mm- to cm-scale displacement	mm- to cm-scale displacement
thickness-displacement correllation	weak correllation	weak correllation
Differences		
architecture	compaction zone enveloping cataclastic core	no compaction zone enveloping core
accommodation of shear displacement	grain reorganization and cataclasis	cataclasis and discrete slip
strain distribution	strain distributed across core and compaction zone	very localized strain
geomechanical response to failure	strain hardening	strain softening
response to post-nucleation additional stress	new band formation	reactivation and slip plane formation
shear mode	compactional shear	closer to simple shear
porosity inside band	very low - some times as low as 1 % or less	relatively high - 9% to 32%
permeability contrast	0-3 orders of magnitude (our single-band measurements)	1.5-4.5 orders of magnitude

DISCUSSION

The deformation bands examined in this work occur in highly porous sandstones and are visually very similar to classical cataclastic deformation bands (CCDB). Furthermore, grain comminution is an important deformation mechanism at the microscale, and none of the bands accumulate large (metre-scale) displacement. However, detailed investigation reveals differences that are significant (Table 3). The

Sinai bands deviate from CCDB in several aspects. Firstly, they lack a grain compaction envelope around the cataclastic zone and, secondly, they exhibit more pronounced cataclasis. However, the most outstanding difference occurs when a central fracture forms in the bands, which localizes most of the subsequent strain accumulation to a zone that is narrower than the original band (see below for the reasoning behind this temporal relationship). At this point, the life of the deformation band as such is over, and it is converted into a *slipped deformation band*. The ensuing discrete slip explains why Sinai bands have accumulated more offset (we have recorded offsets up to 230 mm) than CCDB, which die after accumulating 3-4 cm offset at the most.

The development history of the deformation bands described in the current study can be inferred from the interpretation of different developmental stages, based on the thin sections. The least developed and most pristine bands are the so-called incipient bands (Fig. 10). Cataclasis is mild and there is no porosity reduction (Fig. 13). Only initial deformation appears to have taken place. This stage is followed by bands with pronounced cataclasis but no fracture plane/slip surface (Fig. 6a-c), and, finally, by bands with a central fracture- or slip surface (Fig. 6d-i). We believe that these represent increasingly progressed stages of the evolution of the Sinai bands. We suggest the following model for the evolution of deformation bands in the localities studied here:

1. Scattered grain crushing due to vertical loading (compaction).
2. Nucleation of a cataclastic deformation band. Mild cataclasis, no porosity reduction (incipient band).
3. Progressive shear and cataclasis. The band now displays pronounced cataclasis. Porosity is mildly reduced but still relatively high.
4. Progressive shear, cataclasis and nucleation of a fracture plane in the centre of the band. The fracture nucleates in patches along the band (Fig. 6d), which gradually propagate and coalesce until the fracture is continuous along the entirety of the band (Fig. 6g). No significant further reduction of porosity.
5. Discrete slip along the fracture plane. Slickenlines form. Extreme cataclasis develops near the slip surface (Fig. 8). No significant further reduction of porosity.

The question remains, however: why is a central slip plane generated rather than multiple adjacent bands, as seen in Utah and many other places?

The reactivation of Sinai bands and the resulting formation of a central slip surface contradicts the accepted concept of strain hardening within CCDB (Aydin 1978), where adjacent deformation bands form sequentially by hardening prior to the formation of a slip surface. There is no obvious reason why a similar pattern is not seen in the Sinai bands, but clues may perhaps be found in the pre-existing grain fracturing of the host rock and/or the relatively high porosity observed in the Sinai bands compared to that of CCDB (Fig. 13, Antonellini & Aydin 1994). The proposed deformation bands evolution can be illustrated in a Q-P diagram (Fig. 17), where the mean and differential stresses are plotted along the horizontal and vertical axes, respectively. In this diagram the cam cap envelope (e.g. Antonellini et al. 1994, Borja & Aydin 2004, Wong et al. 2004, Wibberley et al. *in press*), which depends on grain size, porosity and other rock properties, separates elastic from permanent (inelastic) strain. Dilation occurs in the left part of the envelope (at low mean stress), simple shear in the top part (at high differential stress) and pure compaction where the cam-cap intersects the horizontal axis (at relatively high confining pressure). Pure compaction thus occurs at or near zero differential stress at what is referred to as the grain crushing pressure (P*). The distributed grain fracturing in the Nubian Sandstone in the studied locality

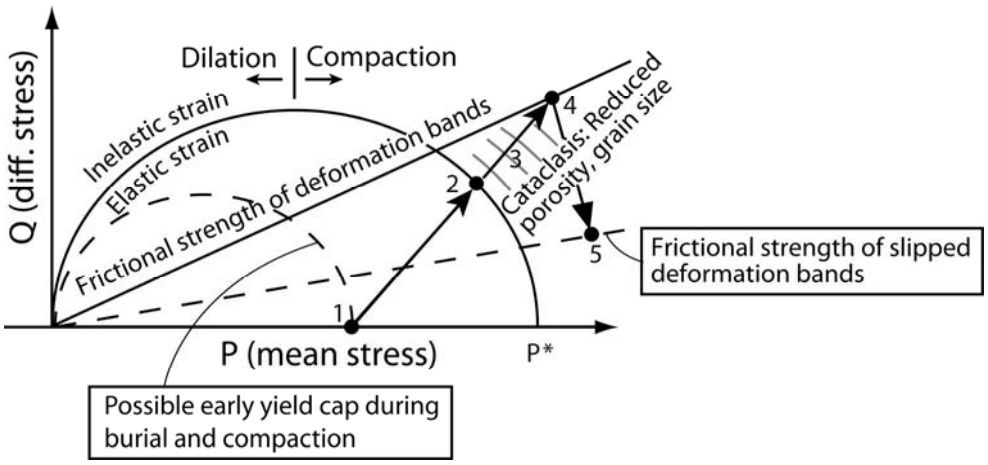

Fig. 17. Q-P diagram (differential stress vs. mean stress) applied to porous rocks (modified from Fossen et al. 2007). The yield surface/cap depends on porosity and grain size as indicated. Numbers 1-5 indicate the stages of development for deformation bands investigated in this study, see text for details.

indicates that the state of stress in the sandstone was close to P*. This abundant grain fracturing must have been caused by the weight of the overburden. We suggest that the local grain crushing pressure (P* in Fig. 17) was reached at some pre-deformation band stage, although unequivocal evidence for this is not found. Although not a common feature for sandstones at shallow burial depths, experimental work has demonstrated that such fracturing may occur at low stresses (2-6 MPa, Chuhan et al. 2002). Interestingly, experiments in the same study have also shown that microfractures can form during compaction. These microfractures are not visible under the microscope. Such fractures cause a general weakening of the sandstone that promotes cataclasis. Yet, pervasive grain fracturing is more common at higher stresses, which at shallow depths could be promoted by low pore pressures (Wong & Baud 1999, Baud et al. 2000). Furthermore, the large host rock grain sizes are more prone to grain fracturing than their fine-grained equivalents at low stresses (lower than 5 MPa, Chuhan et al. 2002). A combination of these effects may thus have been at work to achieve the level of background grain fracturing seen in the host rock.

We speculate that pre-existing grain fractures may promote cataclasis as differential stress builds up and deformation bands form (stage 2 above and in Fig. 17). The grain fractures represent micro-discontinuities that weaken the rock locally, and therefore represent locations where deformation bands can nucleate and grow, especially if the micro-fractures are orientated favourably relative to the applied stress. As cataclasis is a process of grain fracturing, a cataclastic deformation band is essentially a compilation of micro-fractures. In CCDB, stress concentration at the contact point of unfractured grains is allowed to build up until eventually causing failure. Although this is clearly also the case for the bands in Sinai, we believe that the background fracturing of the host rock grains may have had two important effects that make these bands different: 1) the grains fail earlier and without a preceding phase of shear-induced compaction (which is not to be confused with the burial compaction that caused the background grain fracturing seen in the host rock); 2) upon failure, inter-granular fractures grow faster and may have a preferred orientation as fracture growth may follow preferentially orientated intra-granular grain fractures. Thus, shear-induced cataclasis (stages 2-3 above and in Fig. 17) may progress faster and be more severe than what would be the case for a CCDB for the same applied stress. Furthermore, if inter-granular fractures attain a preferred orientation parallel to the band, it may strongly contribute to

local weakening within the band. Hence, the band becomes susceptible to brittle failure and forms a through-going slip surface (stage 4-5 above and in Fig. 17).

Another aspect of rapidly progressing and intense cataclasis is the rapid reduction to very small grain sizes within the band (see e.g. Fig. 9f and 9g). This implies more grains from breakdown of larger grains, and also more grain fracture surfaces. This would aid the nucleation and propagation of a central fracture within a band, since: there are more grain fractures available for amalgamation to a fracture surface. Evidence for the high-intensity cataclasis is found in the particle size distribution data and the magnitude of the three dimensional power law dimension D. As previously mentioned, the high values of D (2.09-2.39, Table 2) recorded in the bands with slip planes indicate that the cataclasis is severe. If compared to Particle size distribution plots from CCDB in the damage zone of the Bartlett Fault, SE Utah (Fig. 18, D= ~1.4-1.5), the value of the three dimensional D is evidently much higher in the Sinai bands containing slip surfaces than in the Utah bands. Thus, the cataclasis is significantly less severe in CCDB from the Bartlett Fault than that of the slipped deformation bands in the current study. However, for Sinai bands *without* a central fracture/slip surface, the D values (1.49-1.72) are comparable, although slightly higher, to those from the Bartlett fault.

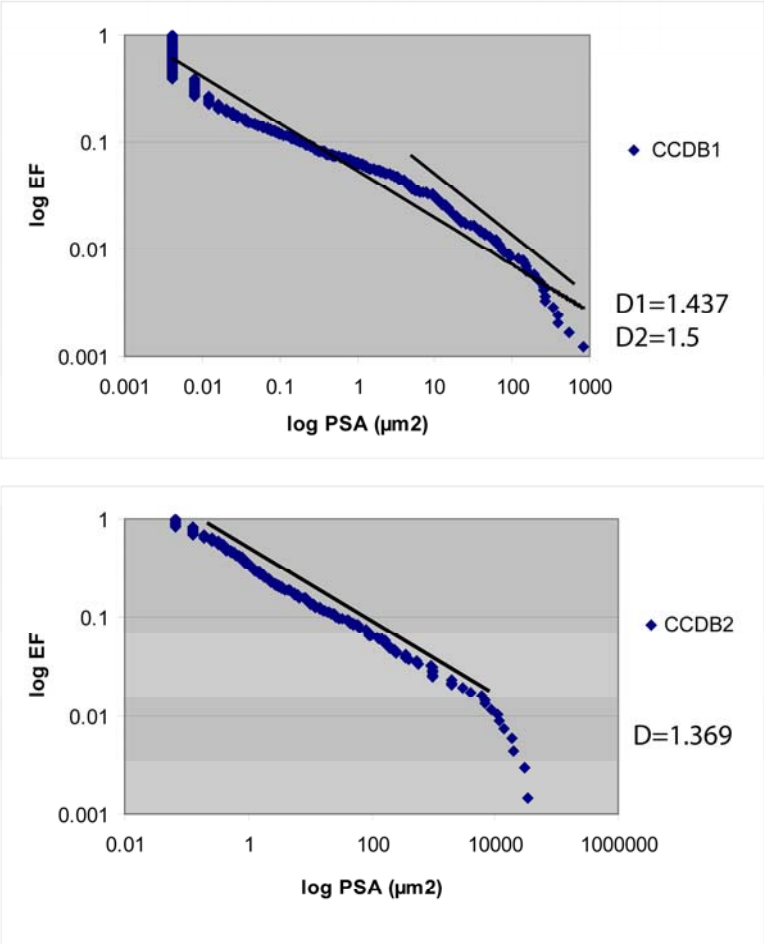

Fig. 18. Particle size distribution data from two deformation bands in the damage zone of the Bartlett Fault, Utah (unpublished). Note that for deformation band CCDB1, two values of the power-law dimension *D* have been calculated, one for the entirety of the data series (D1), and one for the steepest segment (D2).

Porosity is another factor that may have an effect. Higher porosity affect the cam cap envelope and may lower the critical pressure required for failure (Fig. 17, Schultz & Siddharthan 2005, Fossen et al. 2007). Hence, the high porosity within the bands may cause the Sinai bands to be more susceptible to subsequent brittle failure than CCDB. The CCDB, undergoing much more syn-kinematic compaction to the point of complete destruction of porosity, will increase the required critical pressure for subsequent failure (reactivation) and thus strain harden. As the Sinai bands preserve porosity to a larger degree, they have not strain hardened to any significant extent. Thus, the combined effect of preserved porosity and the presence of intra-granular fractures in the host rock make the Sinai bands represent zones of weakness after initial failure.

The porosity difference between Sinai bands and CCDB furthermore suggests that dissimilar modes of deformation are involved in their formation. Whereas CCDB form during compactional shear (resulting in very low porosity), the relatively high porosity in the Sinai bands indicate that they were formed by a mode closer to simple shear. This

also explains why there is no compaction zone enveloping the cataclastic zone. To our knowledge, no record exists of cataclastic deformation bands having formed by isochoric simple shear.

The permeability data presented in this paper are, as previously mentioned, in the upper range of our own and previously published petrophysical data for CCDB (Fig. 16). There are systematic variations, however, with a gradual increase in permeability contrast (relative to matrix permeability) from bands with no slip plane through to bands with fully developed slip surfaces. Permeability contrast also increase with the severity of the cataclasis affecting the same bands. The progressive cataclasis and the associated destruction of pore connectivity, explains the stepwise increase of the permeability contrast described above. Additionally, slip surface wall rocks make efficient sealing membranes, bringing the permeability contrast to a maximum where they are present.

The recorded permeability data have implications for fluid flow. Should such deformation bands occur in a subsurface reservoir, they would represent potential baffles to flow, even more so than CCDB. What is not captured by our permeability measurements, however, is the effect of intra-band slip surfaces on flow *parallel* to the band. The slip surfaces may represent fractures along which fluids can flow. Because of this, their impact on reservoir performance is likely to be significantly different to that of CCDB. Whereas CCDB generally reduce permeability and is considered negative in a reservoir setting, bands with slip planes, although baffles to band-normal flow, represent potential conduits for band-parallel flow. Depending on the continuity and interconnectedness of such bands, they might actually have a positive effect on reservoir communication.

SUMMARY AND CONCLUSIONS

A new type of cataclastic deformation bands has been presented. Based on the collected data and field observations, we draw the following conclusions:

1. The cataclastic deformation bands (CCDB) described in this work are different from classical cataclastic deformation bands described in the existing literature (e.g. Aydin 1978). The Sinai bands are characterized by intense cataclasis,

relatively little compaction, strain weakening and, in many cases, discrete slip along a central slip surface. The bands are thought to have formed under near simple shear conditions.

2. A stepwise model for the evolution of the studied deformation bands has been suggested and is laid out in detail in the previous section.

3. The background grain fracturing observed in the host rock, combined with the limited porosity collapse, is the most probable explanation for the deviation from the classical model for faulting in porous clastic rocks (Aydin & Johnson 1978).

4. The deformation bands feature porosities that are significantly higher than published figures for cataclastic deformation bands elsewhere (e.g. Antonellini & Aydin 1994).

5. Permeability contrast data fall in the high range of data for classical cataclastic deformation bands, particularly where slip surfaces are developed (Fig. 16 and e.g. Antonellini & Aydin 1994, Lothe et al. 2002).

6. In a reservoir setting, the structures may represent baffles to cross-band flow, but slip surfaces also represent fractures *along* which fluids may flow. The bands may therefore act as conduits to band-parallel flow and increase connectivity within a hydrocarbon or groundwater reservoir.

ACKNOWLEDGEMENTS

Ian Sharp is thanked for directing us to the outcrops used in this study. Eivind Bastesen is thanked for assistance during the first field season, and for useful discussions in the early stages of this study. Jan Tveranger and Nestor Cardozo are thanked for an enjoyable time in the field. Nestor Cardozo is also thanked for critical reviews of the manuscript. The authors wish to acknowledge the Fault Facies project for funding this study through the financial project support granted by the Norwegian Research Council, Statoil and ConocoPhillips.

APPENDIX A: POROSITY AND PERMEABILITY ANALYSIS METHODS

Porosity image analysis technique

Porosity has been estimated from BSE images of thin sections using image processing method (Torabi et al. 2007). Grain and pore phases of deformed sandstone occupy different spatial positions. In such a two-phase (grain-pore) system of volume v each phase occupies a subvolume v_1 (for grains) and subvolume v_2 (for pores), and a characteristic or indicator function can be defined as follows:

$$f(\overrightarrow{r}) = \begin{cases} 0 & r \in v_1 \\ 1 & r \in v_2 \end{cases} \qquad (1)$$

Each image includes a matrix of M by N pixels. In order to be able to use the indicator function to characterize the microgeometry of the samples, the colour intensity range should be limited to two pixel values representing the two phases of the medium (binary image). For a binary image we define a function $f_{(i,j)}$ that is zero for grains and one for pores, and (i, j) indicates the position of pixels in the image. The pore one-point correlation function, s_1, gives information about the volume fraction of the two phases in an image consisting of M by N pixels (Garboczi et al. 1999), which is the porosity (ϕ).

$$s_1 = \phi = < f_{(i,j)} > = \frac{1}{MxN} \sum_{ij} f_{(i,j)} \qquad (2)$$

i=1, 2, 3,...M and j=1, 2, 3,…N

Porosity laboratory measurements:

Grain volume was measured by helium injection using a Boyle's law porosimeter. Bulk volume was determined by immersing the sample in mercury, using the weigh balance/ buoyancy technique. Porosity and grain density were calculated by recording the weight of the samples.

Gas permeability laboratory measurements:

Gas permeability (core plugs taken perpendicular to deformation bands and host rock core plugs) was determined by flowing nitrogen gas through the samples. At steady state conditions, the gas flow rate, the pressure drop over the plug sample and the upstream pressure were recorded. The confining pressure applied during the measurement was 20 bar. The gas permeability K_g was then calculated using Darcy's law (Darcy 1856). The Klinkenberg corrected permeability value, K_l, was determined empirically, based on the measured K_g and the corresponding average pore pressure, P_m (Klinkenberg 1941).

Mini-permeameter analysis procedure:

Measurements were conducted using a TinyPerm II Portable Air Permeameter (mini-permeameter) manufactured by New England Research When recording permeability data, the operator pressures a rubber nozzle against the specimen and withdraws air from it with a single stroke of a syringe. As air is pulled from the sample, a micro-controller unit simultaneously monitors the syringe volume and the transient vacuum pulse created at the sample surface. Using signal processing algorithms the micro-controller computes the response function of the sample/instrument system. The response function is related to permeability *K*:

$$T = -0.8206 \times \log_{10}(K) + 12.8737,$$

where *T* is the value of the response function and the recorded output from the mini-permeameter. When performing the tests in the field, the deformation bands were excavated, carefully removing part of the hangingwall of the deformation band. Once access was gained to the surface of the band/slip surface, the tests were performed as described above. For each sample point 3-5 measurements were made, in order to ensure the quality of the data. For each sample point, an average of the measurements was calculated and used as the representative value for that point.

REFERENCES

Abdallah, A. M. & El Adindani, A. 1963. Stratigraphy of upper Paleozoic rocks, western side of the Gulf of Suez **25**. Geological Survey of Egypt Paper, 18 p.

Ahlgren, S. G. 2001. Exploring the formation, microtexture, and petrophysical properties of deformation bands in porous sandstone. *AAPG Bulletin* **85**, 2046.

Antonellini, M. & Aydin, A. 1994. Effect of faulting on fluid flow in porous sandstones: petrophysical properties. *AAPG Bulletin* **78**, 355-377.

Antonellini, M. & Aydin, A. 1995. Effect of faulting on fluid flow in porous sandstones: geometry and spatial distribution. *AAPG Bulletin* **79**, 642-671.

Antonellini, M., Aydin, A. & Pollard, D. D. 1994. Microstructure of deformation bands in porous sandstones at Arches National Park, Utah. *Journal of Structural Geology* **16**, 941-959.

Aydin, A. 1978. Small faults formed as deformation bands in sandstone. *Pageoph* **116**, 913-930.

Aydin, A. & Johnson, A. M. 1978. Development of faults as zones of deformation bands and as slip surfaces in sandstone. *Pageoph* **116**, 931-942.

Aydin, A. & Johnson, A. M. 1983. Analysis of faulting in porous sandstones. *Journal of Structural Geology* **5**, 19-31.

Baud, P., Zhu, W. & Wong, T.-f. 2000. Failure mode and weakening effect of water on sandstone. *Journal of Geophysical Research* **105**, 16371-16389.

Beach, A., Brown, J. L., Welbon, A. W., McCallum, J. E., Brockbank, P. J. & Knott, S. D. 1997. Characteristics of fault zones in sandstones from NW England: application to fault transmissibility. In: *Petroleum geology of the Irish Sea and adjacent areas* (edited by Meadows, N. S., Trueblood, S. P., Hardman, M. & Cowan, G.). Geological Society, London, Special Publications **124**, 315-324.

Bense, V. F., Van den Berg, E. H. & Van Balen, R. T. 2003. Deformation mechanisms and hydraulic properties of fault zones in unconsolidated sediments; the Roer Valley Rift System, The Netherlands. *Hydrogeology Journal* **11**, 319-332.

Bjørlykke, K. & Egeberg, P. K. 1993. Quartz cementation in sedimentary basins. *AAPG Bulletin* **77**, 1538-1548.

Bjørlykke, K. & Høeg, K. 1997. Effects of burial diagenesis on stresses, compaction and fluid flow in sedimentary basins. *Marine and Petroleum Geology* **14**, 267-276.

Blenkinsop, T. G. 1991. Cataclasis and processes of particle size reduction. *Pageoph* **136**, 59-86.

Borja, R. I. & Aydin, A. 2004. Computational modeling of deformation bands in granular media. I. Geological and mathematical framework. *Comput. Methods Appl. Mech. Engrg.* **193**, 2667-2698.

Bosworth, W. 1995. A high-strain rift model for the southern Gulf of Suez (Egypt). In: *Hydrocarbon Habitat in Rift Basins* (edited by Lambiase, J. J.). Geological Society, London, Special Publications **80**, 75-102.

Bosworth, W., Huchon, P. & McClay, K. 2005. The Red Sea and Gulf of Aden Basins. *Journal of African Earth Sciences* **43**, 334-378.

Chuhan, F. A., Kjeldstad, A., Bjørlykke, K. & Høeg, K. 2002. Porosity loss in sand by grain crushing - experimental evidence and relevance to reservoir quality. *Marine and Petroleum Geology* **19**, 39-53.

Cochran, J. R. 1983. A model for development of the Red Sea. *AAPG Bulletin* **67**, 41-69.

Darcy, H. 1856. *Les Fontaines Publiques de la Ville de Dijon*, Dalmont, Paris, 647 p.

Davatzes, N. C. & Aydin, A. 2003. Overprinting faulting mechanisms in high porosity sandstones of SE Utah. *Journal of Structural Geology* **25**, 1795-1813.

Davis, G. H. 1999. *Structural geology of the Colorado Plateau Region of Southern Utah, with special emphasis on deformation bands*. The Geological Society of America, 157 p.

Du Bernard, X., Labaume, P., Darcel, C., Davy, P. & Bour, O. 2002. Cataclastic slip band distribution in normal fault damage zones, Nubian sandstones, Suez rift. *Journal of Geophysical Research* **107**, ETG6-1, 6-12.

Edwards, H. E., Becker, A. D. & Howell, J. A. 1993. Compartmentalization of an aeolian sandstone by structural heterogeneities: Permo-Triassic Hopeman Sandstone, Moray Firth, Scotland. In: *Characterization of fluvial and aeolian reservoirs* (edited by North, C. P. & Prosser, D. J.). *Geological Society, London, Special Publications* **73**, 339-366.

Fisher, Q. J. & Knipe, R. J. 2001. The permeability of faults within siliciclastic petroleum reservoirs of the North Sea and Norwegian Continental Shelf. *Marine and Petroleum Geology* **18**, 1063-1081.

Fossen, H. & Gabrielsen, R. H. 2005. *Strukturgeologi (structural geology textbook in Norwegian)*. Fagbokforlaget, Bergen, 375 p.

Fossen, H. & Hesthammer, J. 1997. Geometric analysis and scaling relations of deformation bands in porous sandstone. *Journal of Structural Geology* **19**, 1479-1493.

Fossen, H. & Hesthammer, J. 1998. Deformation bands and their significance in porous sandstone reservoirs. *First Break* **16**, 21-25.

Fossen, H., Schultz, R. A., Shipton, Z. K. & Mair, K. 2007. Deformation bands in sandstone - a review. *Journal of the Geological Society, London* **164**, 755-769.

Gallagher, J. J., Friedman, M., Handin, J. & Sowers, G. M. 1974. Experimental studies relating to microfracture in sandstone. *Tectonophysics* **21**, 203-247.

Garboczi, E. J., Bentz, D. P. & Martys, N. S. 1999. Digital images and computer modeling. In: *Methods in the Physics for porous media* (edited by Wong, P.-Z.). Academic Press, San Diego, California **35**, 1-41.

Garfunkel, Z. & Bartov, Y. 1977. Tectonics of the Suez Rift. *Geological Survey of Israel Bulletin* **71**, 1-41.

Gupta, S., Underhill, J. R., Sharp, I. R. & Gawthorpe, R. L. 1999. Role of fault interactions in controlling synrift sediment dispersal patterns: Miocene, Abu Alaqa Group, Suez Rift, Sinai, Egypt. *Basin Research* **11**, 167-189.

Hesthammer, J. & Fossen, H. 2001. Structural core analysis from the Gullfaks area, northern North Sea. *Marine and Petroleum Geology* **18**, 411-439.

Jackson, C. A. L., Gawthorpe, R. L., Leppard, C. W. & Sharp, I. R. 2006. Rift-initiation development of normal fault blocks: insights from the Hammam Faraun fault block, Suez Rift, Egypt. *Journal of the Geological Society, London* **163**, 165-183.

Jamison, W. R. & Stearns, D. W. 1982. Tectonic deformation of Wingate Sandstone, Colorado National Monument. *AAPG Bulletin* **66**, 2584-2608.

Johansen, T. E. S. & Fossen, H. *in press*. Internal deformation of fault damage zones in interbedded siliciclastic rocks. Geological Society, London, Special Publications.

Klinkenberg, L. J. 1941. The permeability of porous media to liquid and gases. In: *Drilling and Production Practice*. American Petroleum Inst. 200-213.

Knipe, R. J., Fisher, Q. J., Jones, G., Clennell, M. R., Farmer, A. B., Harrison, A., Kidd, B., McAllister, E., Porter, J. R. & White, E. A. 1997. Fault seal analysis: successful methodologies, applications and future directions. In: *Hydrocarbon Seals: Importance for Exploration and Production* (edited by Møller-Pedersen, P. & Koestler, A. G.). Norwegian Petroleum Society Special Publication **7**, 15-40.

Lothe, A. E., Gabrielsen, R. H., Bjørnevoll-Hagen, N. & Larsen, B. T. 2002. An experimental study of the texture of deformation bands; effects on the porosity and permeability of sandstones. *Petroleum Geoscience* **8**, 195-207.

Lyberis, N. 1988. Tectonic evolution of the Gulf of Suez and the Gulf of Aqaba. *Tectonophysics* **153**, 209-220.

Mair, K., Main, I. & Elphick, S. 2000. Sequential growth of deformation bands in the laboratory. *Journal of Structural Geology* **22**, 25-42.

Mandl, G., DeJong, L. N. J. & Maltha, A. 1977. Shear zones in granular material. *Rock Mechanics* **9**, 95-144.

Moustafa, A. R. 1993. Structural characteristics and tectonic evolution of the east-margin blocks of the Suez rift. *Tectonophysics* **223**, 281-299.

Sammis, C., King, G. & Biegel, R. 1987. The kinematics of gouge deformation. *Pageoph* **125**, 777-812.

Schultz, R. A. & Balasko, C. M. 2003. Growth of deformation bands into echelon and ladder geometries. *Geophysical Research Letters* **30**, 2033, 10.1029/2002GL018449.

Schultz, R. A. & Siddharthan, R. 2005. A general framework for the occurrence and faulting of deformation bands in porous granular rocks. *Tectonophysics* **411**, 1-18.

Sharp, I. R., Gawthorpe, R. L., Armstrong, B. & Underhill, J. R. 2000. Propagation history and passive rotation of mesoscale normal faults: implications for syn-rift stratigraphic development. *Basin Research* **12**, 285-306.

Shipton, Z. K. & Cowie, P. A. 2003. A conceptual model for the origin of fault damage zone structures in high-porosity sandstone. *Journal of Structural Geology* **25**, 333-345.

Shipton, Z. K., Evans, J. P., Robeson, K. R., Forster, C. B. & Snelgrove, S. 2002. Structural heterogeneity and permeability in faulted aeolian sandstone: Implication for subsurface modeling of faults. *AAPG Bulletin* **86**, 863-883.

Shukri, N. M. 1945. Geology of the Nubian sandstone. *Nature* **156**, 116.

Sternlof, K. R., Chapin, J. R., Pollard, D. D. & Durlofsky, L. J. 2004. Permeability effects of deformation band arrays in sandstone. *AAPG Bulletin* **88**, 1315-1329.

Taylor, W. L. & Pollard, D. D. 2000. Estimation of in-situ permeability of deformation bands in porous sandstone, Valley of Fire, Nevada. *Water Resources Research* **36**, 2595-2606.

Torabi, A., Braathen, A., Cuisiat, F. & Fossen, H. 2007. Shear zones in porous sand: Insights from ring-shear experiments and naturally deformed sandstones. *Tectonophysics* **437**, 37-50.

Underhill, J. R. & Woodcock, N. H. 1987. Faulting mechanisms in high porosity sandstones; New Red Sandstone, Arran, Scotland. In: *Deformation of sediments and sedimentary rocks* (edited by Jones, M. E. & Preston, R. M. F.). Geological Society, London, Special Publications **29**, 91-105.

Wibberley, C. A. J., Petit, J.-P. & Rives, T. *in press*. The mechanics of fault distribution and localization in high-porosity sands, Provence, France. In: *The localization of*

fracture damage in rocks (edited by Couples, G. D., Lewis, H. & Meredith, P. D.). The Geological Society of London, Special Publication, *in press*.

Wong, T.-f. & Baud, P. 1999. Mechanical compaction of porous sandstones. *Oil & Gas Science and Technology - Rev. IFP* **54**, 715-727.

Wong, T.-f., David, C. & Menébdez, B. 2004. Mechanical compaction. In: *Mechanics of fluid-saturated rocks* (edited by Guéguen, Y. & Boutéca, M.). Elsevier, Amsterdam 55-114.

Paper 3

Torabi, A., Fossen, H., and Alaei, B., 2007. Application of spatial correlation functions in permeability estimation of small-scale deformation bands in porous rocks. In press, Journal of Geophysical Research (Solid Earth).

Application of spatial correlation functions in permeability estimation of deformation bands in porous rocks

Anita Torabi[1], Haakon Fossen[1], Behzad Alaei[2]

1) Department of Earth science, University of Bergen, Centre for Integrated Petroleum Research, Allégt. 41, 5007 Bergen, Norway

2) Rocksource ASA, Olav Kyrresgt. 22, 5808 Bergen, Norway

Corresponding author, anita.torabi@cipr.uib.no

Abstract

Millimeter-thick strain localization structures in porous sandstones, known as deformation bands, are reported to perturb the permeability structure of petroleum reservoirs and aquifers. However, the internal permeability structure of deformation bands is difficult to assess by means of classical methods. We have used spatial correlation functions to estimate the porosity and specific surface area in the deformed sandstones from high-resolution Backscattered Electron images. This work demonstrates the use of a modified version of the Kozeny-Carman relation to calculate permeability based on the information obtained from image processing. We have identified the anisotropy with regard to petrophysical properties in deformed sandstones and demonstrated variations in microstructure and properties across and along the deformation bands. Our results show that properties outside the deformation bands differ significantly from those inside the band (up to three orders of magnitude). Moreover permeability varies by up to two orders of magnitude along a single band. Furthermore, our porosity and permeability estimates are lower than those obtained from plug measurements. While plug measurements measure the effective permeability across a 2.54 cm (inch) long sample, the method demonstrated here provides a means to estimate porosity and permeability on the microscale, and to map out the variations in these properties along as well as across deformation bands and similar structures.

Key words: Microstructure, Permeability and porosity, transport properties

1. Introduction

Much attention has recently been devoted to faulted sandstones and their porosity and permeability structure [Ogilvie et al., 2001; Bense et al., 2003; Sternlof et al., 2004; Kwon et al., 2005]. Deformation localizes in highly porous sandstones and sediments by the formation of deformation bands [Aydin et al., 2006; Fossen et al., 2007], which are millimeter thick zones of deformation. Deformation bands range from compactional through simple shear to dilational, and involve particulate flow, cataclasis and/or dissolution. In most cases, porosity and permeability are altered within deformation bands during formation and growth. In particular, many deformation bands have been found to have considerably lower permeability than their host rocks [Pittman 1981; Jamison and Stearns 1982; Antonellini and Aydin, 1994; Knipe et al., 1997; Gibson 1998; Fisher and Knipe, 2001; Lothe et al., 2002; Shipton et al., 2002], although dilation and permeability increase can occur in some cases [e.g., Du Bernard et al., 2002]. Deformation bands are common constituents of clastic petroleum reservoirs, where they occur as single structures, as clusters and in fault damage zones [e.g., Hesthammer and Fossen, 2001]. Thus, predicting the role of deformation bands in a petroleum reservoir relies on a sound understanding of their permeability structure.

Permeability is traditionally measured using a mini-permeameter in the field or by drilling inch-size cores for laboratory testing. In our experience, mini-perm measurements have large uncertainties, and plug measurements are hampered by sampling difficulties, weathering effects and high cost, and require advanced laboratory facilities. Moreover, the resolution of plug measurements is constrained by the plug length (usually 2.54 cm/ 1 inch) while deformation structures such as single deformation bands in porous sandstones are only around 1 mm thick.

As an alternative approach, image processing methods can be used to characterize the microstructure of the rocks and to provide a quantitative means for understanding the dependence of physical properties on the pore structure [Blair et al., 1996]. During the past decades, different approaches have been used to relate microstructural information to physical, mechanical and transport properties of rocks [Ehrlich et al., 1984; Wissler, 1987; Koplik et al., 1984; Doyen, 1988; Blair et al., 1996, Bakke and Øren, 1997; Keehm et al., 2004; 2006; White et al., 2006; Wu et al., 2006]. For instance, Bakke and Øren [1997] presented a process-based modeling for sandstone that accounts for physical

processes such as sedimentation, compaction and digenesis. Their model is suitable only for undeformed sandstone with a limited range of grain size. Keehm et al. [2004]; [2006] predicted permeability from thin sections. They reconstructed 3D porous media from 2D thin section using a stochastic method and the Lattice Boltzmann technique for 3D flow simulation. We have applied Blair et al's. [1996] method to the high resolution Backscattered Electron images (BSE) of deformation bands. Moreover, employing high resolution images allows us to capture complex microgeometry in deformation bands. In this study we use spatial correlation functions to characterize the microgeometry of small-scale deformation structures in a statistical way and to estimate their physical properties such as porosity and specific surface area.

Few attempts have been made to apply the spatial correlation functions to obtain microgeometry of anisotropic porous media. Berge et al. [1993, 1997] applied correlation functions for anisotropic porous media on 2D images of tuff. Berryman [1998] has developed the fundamental formulation for stationary anisotropic porous materials but his concept has not been tested on real anisotropic rock samples.

In the present study, we show how deformation bands induce anisotropy (both across and along the band) to sandstone at the microscale and for the first time apply Berryman's concept [1998] to a natural anisotropic and heterogeneous media. Under Fault Facies research project at the Centre for Integrated Petroleum Research at the University of Bergen, we have investigated many faulted sandstones from different sedimentary basins to explore the effects of deformation bands on the physical properties of sandstone. Understanding the nature of the anisotropy introduced by deformation bands is crucial in estimating three-dimensional properties of deformed sandstones from two-dimensional images. Porosity values have been extracted from low magnification images by applying a one-point correlation function to the binary BSE images of both bands and outside bands. Specific surface area of the pore-grain interface has been estimated using a two-point correlation function and employing images with different magnification. The details of three different approaches for calculating specific surface area will be described in the result section. Finally specific surface area and porosity values were used to estimate the permeability using empirical relations such as the Kozeny-Carman relation. The estimated permeability values are compared to plug measurements.

2. Theoretical framework

Rocks are usually considered as composite materials composed of at least two phases; solids and pores. The properties of composite materials depend on the properties, amount and spatial distribution of each phase. Some properties, such as the elastic modulus and permeability, are functions of pore phase microstructure. The statistical distribution of the relative locations of the microstructural features of interest represents their spatial arrangement.

N-point correlation functions are important statistical descriptors that are useful for characterizing the spatial arrangement and heterogeneity of microstructural geometry [e.g. Debye et al., 1957; Corson, 1974; Gokhale, 2004; Cule and Torquato, 1999]:

$$S_n^{(i)}(r_1, r_2, ...r_n) = < (f^{(i)}(r_1) f^{(i)}(r_2) ... f^{(i)}(r_n)) > \qquad (1)$$

Equation 1 describes the volume average over the spatial positions of r. N-point correlation functions contain statistical information about the arrangement of the constituents in a composite material by measuring the probability of certain simple geometrical arrangements of the constituents.

The basic information on volume composition and interfacial surface area is contained in the lowest-order correlation functions [Cule and Torquato, 1999]. The one-point (S_1) and two-point (S_2) pore-pore correlation functions are given by

$$S_1(r) = < f(r) > \qquad (2)$$

$$S_2(r) = < f(r+x) f(r+y) > \qquad (3)$$

Two properties of the two-point correlation function can be derived from equations 4 and 5:

$$S_2(r) = S_1(r) = \phi \quad (x, y) \to 0 \qquad (4)$$

$$\lim_{r \to \infty} S_2(r) = \phi^2 \qquad (5)$$

$S_2(r)$ has the characteristic asymptotic behavior [e.g., Cule and Torquato, 1999]. Grain and pore phases of deformed sandstone occupy different spatial positions. In such a two-phase (grain-pore) system of volume v each phase occupies a subvolume v_g (for grains) and subvolume v_p (for pores), and a characteristic or indicator function can be defined as follows:

$$f(\vec{r}) = \begin{cases} 0 & r \in v_g \\ 1 & r \in v_p \end{cases} \qquad (6)$$

The pore one-point correlation function, S_1, gives information about the volume fraction of the two phases represented by an image consisting of M by N pixels [Garboczi et al., 1999]

$$S_1 = \phi = < f_{(i,j)} > = \frac{1}{MxN} \sum_{ij} f_{(i,j)} \qquad (7)$$

i=1, 2, 3,... M and j=1, 2, 3,…N

The pore-pore two-point correlation function, $S_2(x,y)$, describes the probability that two points with a specified distance apart (a line) are both in pore phase. It is defined by

$$S_2(x,y) = < f_{(i,j)} f_{(i+x,j+y)} > = \frac{1}{MxN} \sum f_{(i,j)} f_{(i+x,j+y)} \qquad (8)$$

We assume that the system is translational invariant so only the difference between the two pixels is important, not their absolute positions. Furthermore, $S_2(x,y)$ can be calculated using Fourier transform methods. We have used the following equation [Garboczi et al., 1999] to calculate the two-point correlation function:

$$S_2(x,y) = \sum_{i=1}^{M-x} \sum_{j=1}^{N-y} \frac{f_{(i,j)} f_{(i+x,j+y)}}{(M-x)(N-y)} \qquad (9)$$

The equation shows the two-point correlation function for an MxN matrix (for example a 2D image of faulted sandstone) in a Cartesian coordinate system.

2. 1. Deformation band induced anisotropy

Characterization of the microstructure of anisotropic porous media has not been explored in much detail and is an important new area within the field of rock physics. The development of more accurate methods that relate anisotropy to rock properties such as permeability is of high importance. Although such applications are more difficult in general, correlation functions may also be applied to anisotropic random media [Berge et al., 1997].

2D images of thin sections from deformed sandstone have been used in this study. Figure 1 shows typical deformation bands at three different scales: outcrop scale, plug sample scale, and at the microscale represented by a photomicrograph. It is obvious from these pictures that the strain localization represented by the deformation bands adds anisotropy to the sandstone. An anisotropic spatial correlation function of a random porous medium could be used to compute the specific surface area by first performing

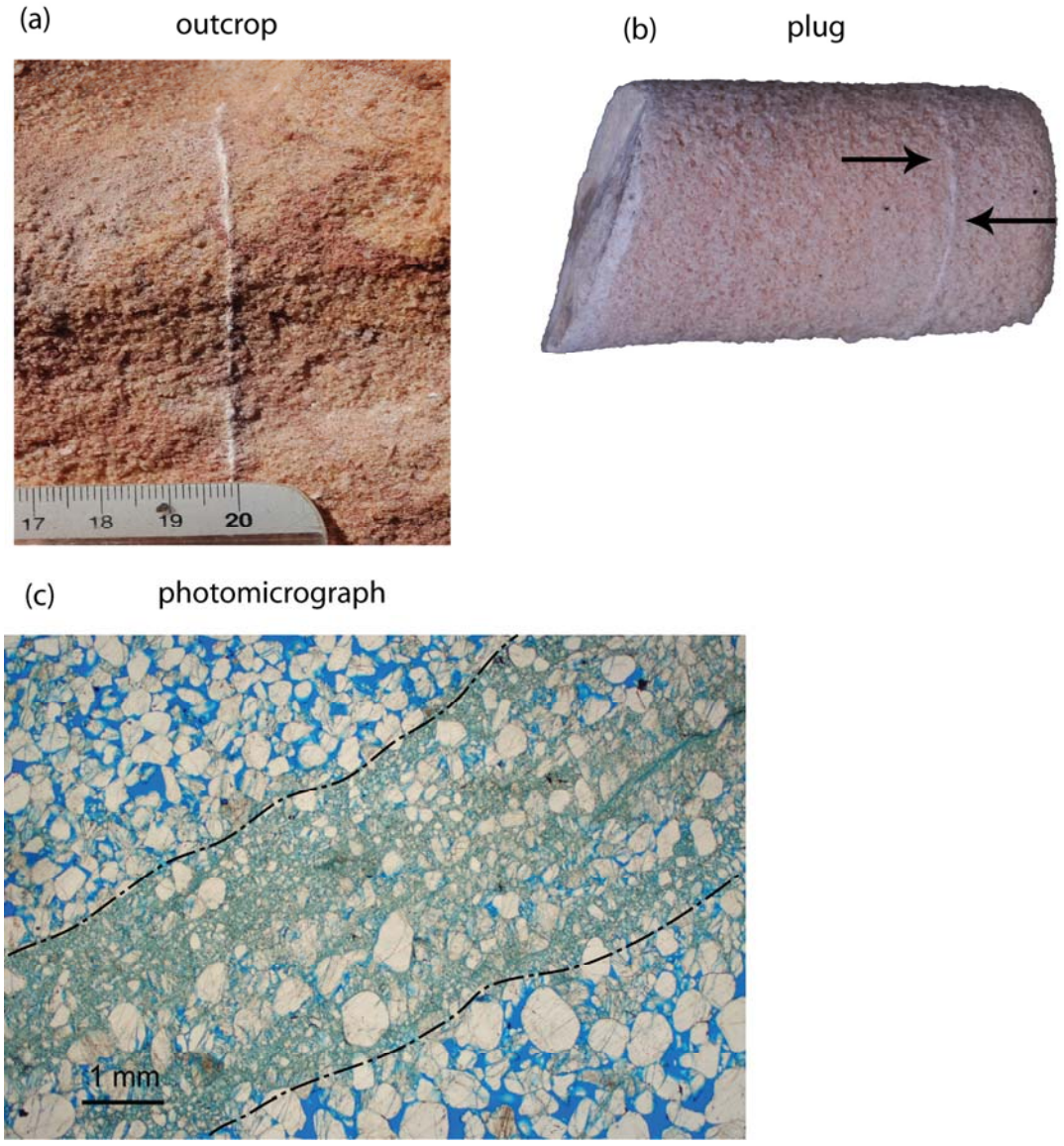

Figure 1. Deformation bands in (a) outcrop, scale bar is in centimeters (b) plug (length of the plug is 2.54 cm/1 inch) and (c) *under* optical microscope.

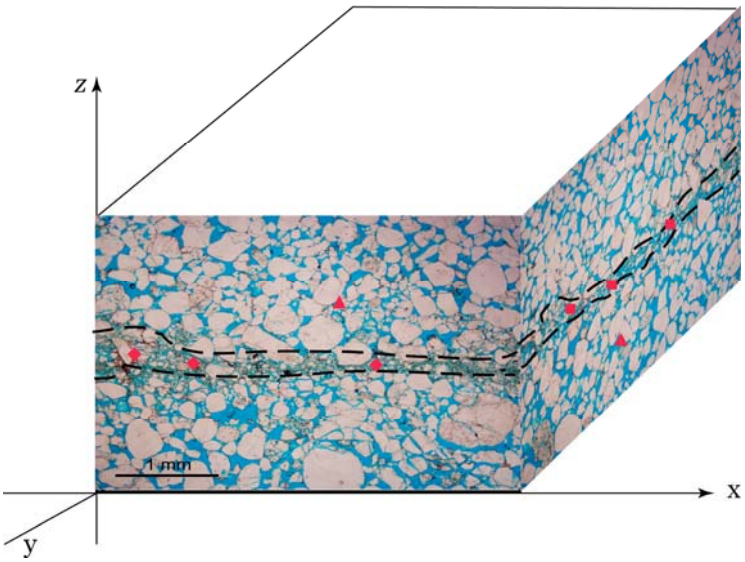

Figure 2. Photomicrographs from two perpendicular thin sections from one single band from sample LD-6 (Sinai, Egypt) that show variation of microstructure along the band in the xz plane and yz planes. The symbols on the Figure correspond to the symbols in Figure 7, which show the approximate location of measured data.

a three-dimensional average and then taking the first derivative with respect to the lag at the origin. However, by using 2D images and an understanding of the nature of anisotropy, planar radial average can be calculated instead [Berryman, 1998]. Therefore we first calculated the two-point correlation function in a Cartesian coordinate system using Equation 9. Then we calculated the planar radial average using 2D bilinear interpolation method and the following equation to convert the Cartesian coordinate system to polar coordinate system.

$$S_2(r) = \frac{1}{2r+1}\sum_{l=0}^{2r} S_2(r, \frac{\pi l}{4r}) \qquad (10)$$

Understanding the nature of anisotropy with regard to petrophysical properties (porosity, permeability) induced by deformation is crucial in estimating three-dimensional properties of deformed sandstones from two-dimensional images. There are both macro- and microscopic aspects of the permeability-related anisotropy caused by deformation bands. Macroscopically, individual deformation bands are only around one

millimeter thick and up to a hundred meters long, across which fluid flow is reduced because of the permeability contrast between the band and their host rock. This aspect has been investigated using plug measurements in the laboratory and mini-permeameter in the field [e.g. Antonellini and Aydin, 1994; Sigda et al., 1999; Shipton et al., 2002]. While this aspect regards variations across the band, i.e. in the z direction in Figure 2, microscopic variations within the band may occur in the xy-plane. In order to investigate these microscale variations we have prepared thin sections from two perpendicular sections (xz and yz planes) through a deformation band (Figure 2).

Berryman [1998] assumes that if the random variations of the properties occur only along the z axis, the surface normal vector is uniformly distributed and lies in the same plane as *r*. Therefore, the specific surface area (i.e. the total area of the pores divided by total volume of the porous media) can be calculated using:

$$S'_{2\,zx}(0) = -\frac{s}{\pi} \qquad (11)$$

However, this assumption is not always valid since both microstructure and physical properties may vary along deformation bands (Figure 2).

If we consider the deformed sandstone to be anisotropic in three dimensions, then the normal vector does not necessarily lie in the plane of *r*. In this case the specific surface area is given by [Berryman, 1998]:

$$S'_2(0) = -\frac{s}{4} \qquad (12)$$

Since we have identified variations in microstructural features such as grain size and pore space distribution along the band, Equation 12 provides a better estimate of the specific surface area from two point correlation functions than Equation 11, as discussed in more detail in the result section.

2.2. Image processing and spatial correlation functions

The selected BSE images are imported as unsigned 8-bit integer with a gray-scale intensity range from 0 to 255 and the pixel values clustered within this range. The spatial resolution of the image indicates the size of the pixels, with high resolution implying a small pixel size. Both resolution and magnification of the image are important in capturing the microstructural properties of the rocks, as discussed in the result section.

Each image includes a matrix of M by N pixels. If there is noise in the data, isolated pixels can be removed by filters such as a median filter. In order to be able to use the indicator function (Equation 6) to characterize the microgeometry of the samples, the color intensity range should be limited to two pixel values representing the two phases of the medium. The intermediate pixels between white and black pixel values in the gray-scale images have proportions of black and white in their areas. When a threshold shade of gray is chosen, all pixels with grays above this threshold are white (grains) and all below are black (pores). Two methods have been used to calculate the threshold value to generate the binary image. The resulting binary image is evaluated by visual inspection and compared to the original BSE image to get the best estimate of the threshold. The two methods are:

1. MATLAB built-in function (imhist): The function uses Otsu's method [1979], which chooses the threshold to minimize the intraclass variance of the black and white pixels.
2. Manual selection: The histogram of intensity range (0 to 255) versus frequency of each intensity value has been used to select the threshold value manually.

The binary image has pixel value ‘0’ in the pore space and ‘1’ in the grain space. Since we are interested in void correlation functions, the binary image has been reversed to have ‘1’ for voids and ‘0’ for grains. Then we define a function $f_{(i,j)}$ that is zero for grains and one for pores, and (i, j) indicates the position of pixels in the image. Figures 3a and 3b show an original gray-scale image and its reversed binary image (pores white and grains black). One point correlation function has been calculated for the reverse binary image using Equation 7.

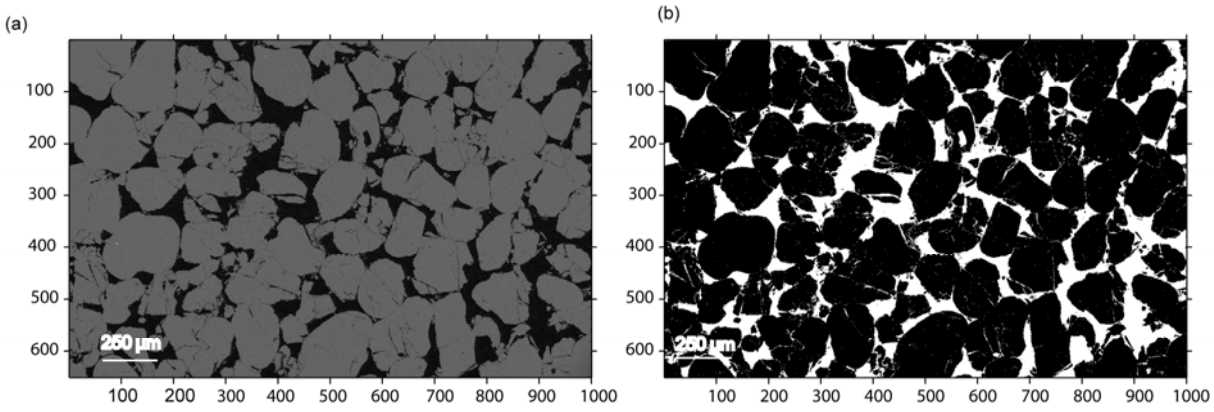

Figure 3. BSE image from outside band (host rock); (a) gray-scale image (b) reversed binary image obtained from the image shown in Figure 3a.

In this work, Equations 9 and 10 have been used in a function that is written in MATLAB to calculate the two-point correlation function for the reversed binary image. Finally Equation 12 has also been used to estimate the specific surface area from two-point correlation functions. Figure 4 shows the anisotropic two-point correlation function variations versus r. The two properties of the correlation function (Equations 4 and 5) and its asymptotic behavior are also shown in Figure 4.

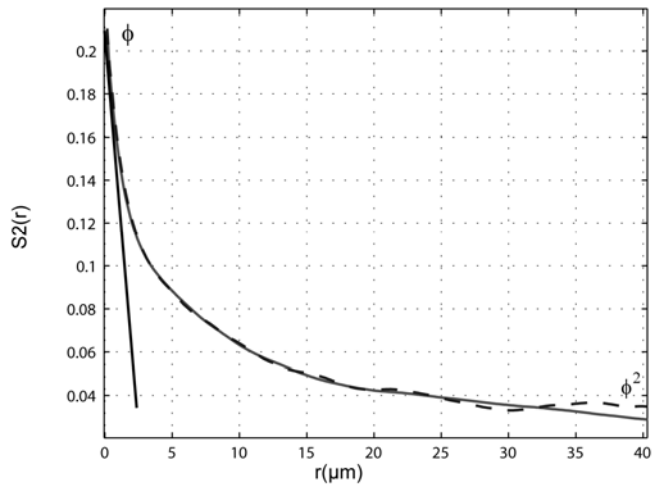

Figure 4. Normalized two-point correlation function versus distance (chosen along the image). The solid line shows the slope near the origin. Note the properties that can be obtained from this function. The maximum value at the origin is equal to porosity and the asymptotic value corresponds to φ^2.

2.3. Permeability and Kozeny-Carman relation

In order to estimate permeability we use a modified version of the Kozeny-Carman relation developed by Paterson [1983] and Walsh and Brace [1984]. Here, pores in the porous media are considered to be tubular. We then have that

$$k = \phi^2 / cFs^2 \qquad (13)$$

where ϕ is the porosity and c is a constant related to pore geometry that is equal to 2 for porous materials (assuming that pores have circular cross-sections) and F is the formation factor and has an exponential relationship with porosity [Archie 1942];

$$F = \phi^{-m} \qquad (14)$$

Furthermore, s is the specific surface area of the tubes. Archie [1942] defined an empirical relationship between electrical properties and formation factor for rocks. Later Wyllie [1952] developed the relationship between formation factor and other properties of rocks, such as porosity. In this relation the exponent m is a cementation factor and it varies between 1.5 for poorly consolidated sandstones and 2 for well consolidated sandstones [Brace, 1977; Sen et al., 1981; Wong et al., 1984; Blair et al., 1996]. We used 1.8 for our moderately consolidated sandstones. The computed porosities and specific surface areas from spatial correlation functions are used to estimate permeability using Equation (13).

3. Results

The size range resolvable from back scatter images depends on the magnification and resolution of the image. We have used BSE images (1024 × 768) with variety of magnifications, i. e. from 155X up to 2.58 KX. It is important to consider the effect of magnification on the calculated one- and two-point correlation functions. Based on previous studies [e. g. Blair et al., 1996], low magnification images (images which include 10-100 grains) seem to be appropriate for calculating one-point correlation functions (porosity), since they cover a bigger area of the sample than high magnification images and therefore are more representative. It has also been verified that laboratory measured porosity are in agreement with the estimated values from low magnification images. On the other hand, high magnification images are more suitable for obtaining a

two-point correlation function and hence specific surface area of the pore-grain interface [e.g. Blair et al., 1996].

Having accepted Blair et al's [1996] concept, we use low magnification images that cover the whole area of interest for porosity estimates from both inside and outside the band. To calculate specific surface area outside of the band by means of the two-point correlation function, we use a high magnification image. Cataclastic deformation bands have wide range of grain size and pore geometry. Therefore it is a challenge to pick the appropriate magnification to assess the accurate specific surface area of the pores in these bands.

Table 1 shows the information related to the samples that have been used in this study. Figure 5 shows five BSE images from sample Wk-01 from Sinai, Egypt at different magnifications as examples. Figure 5a illustrates an overview of the whole thin section from sample Wk-01, which has a deformation band in the middle (Table 1).

Table 1 . Description of the samples of the thin sections used in this study

sample	Grain size	Mineralogy	Type of band	Formation	Location	Coordinates
UT	fine	Quartz arenite	Cataclastic band with quartz dissolution	Entrada Sst.	San Rafael Desert, Utah, USA	0525998-4271679
CNM	fine	Quartz arenite	Cataclastic band with quartz dissolution	Navajo Sst.	Colorado Nat'l Mon., USA	4332902-695343
V	Fine to medium	Quartz arenite	Cataclastic band with some quartz dissolution	Moab Mbr.	Hidden Canyon Utah, USA	4285800-605825
WK-01	medium	Quartz arenite	Cataclastic band	Nubian Sst.	Sinai, Egypt	0523668-3219513
Wk-08	medium	Quartz arenite	Cataclastic band	Nubian Sst.	Sinai, Egypt	0523668-3219513
I	medium	Quartz arenite	Cataclastic band with some iron oxide cement	Nubian Sst.	Sinai, Egypt	-
LD-6A, B	medium	Quartz arenite	Cataclastic bands with some iron oxide cement	Nubian Sst.	Sinai, Egypt	-

By increasing the magnification (Figure 5c, 5d, 5e, which have been used for calculation of specific surface area) only a small part of a deformation band is perceptible and hence the calculated specific surface area cannot be correct. Our research shows that in order to capture the complex microgeometry of deformation bands we need several high-resolution BSE images across the band. In order to verify this idea and examine the two-point void correlation function sensitivity to the magnification of the images, a database from our measurements for deformation bands, using images with different magnifications from deformed sandstone is provided (Table 2, Figure 6). We applied three different approaches:

1. First we calculated the specific surface area of the pores from an image with a low magnification that covers the entire thickness of the band. We have also used this image for porosity estimation since it includes the wide variety of the grain and pore size in the deformation bands (squares in Figure 6 show the calculated permeability using this approach, Table 2).
2. In a second approach, we followed Blair et al.'s (1996) concept and used one high magnification image from a small part of the band to calculate specific surface area of the pores (triangles in Figure 6 show the calculated permeability using this approach, as listed in Table 2).

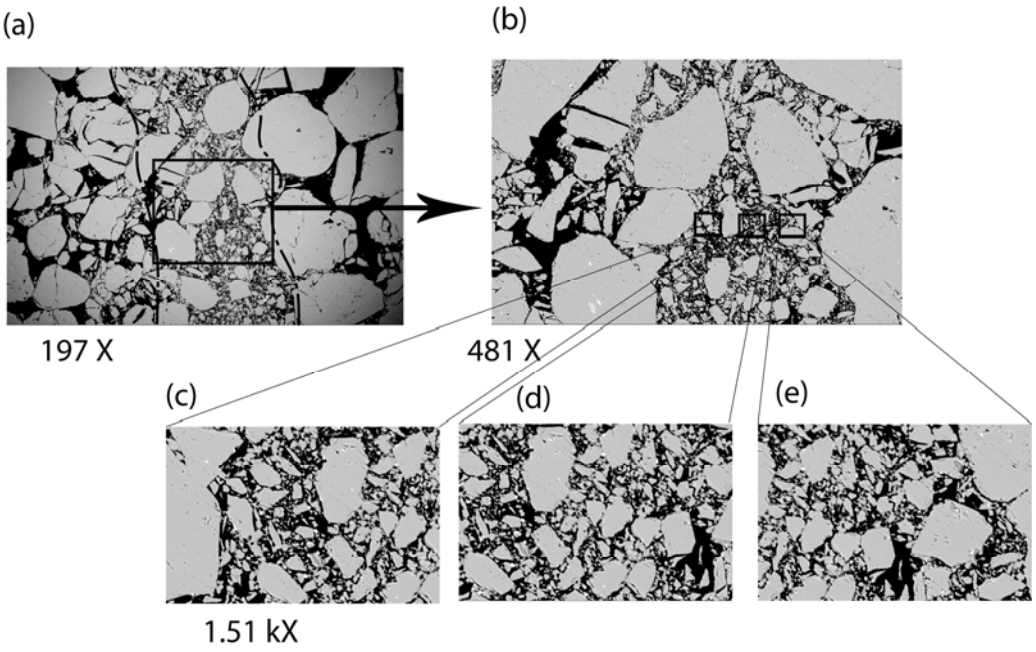

Figure 5. (a) BSE image from deformed sandstone with a central deformation band. (b) Low magnification BSE image from the band that covers the entire width of the band and has been used for porosity estimation of the band. (c), (d), (e) High-magnification BSE images taken across the band that cover the entire width of the band and have been used for calculation of two point correlation functions and hence average of the specific surface area.

3. In a third approach, several high magnification images were taken across the band to cover the entire thickness of the band. Then the average specific area for the entire band was estimated using specific surface areas obtained for the different

images (diamonds in Figure 6 show the calculated permeability using this method, Table 2).

The permeability values calculated by using the first approach are always higher than those from the next two approaches. We can classify our results into two different groups.

1. In samples “Wk-01”, “Wk-08” and “I” from Sinai, the permeability obtained from averaging the specific surface area (approach 3) are lower than the results from the first approach but higher than the values from the second approach.
2. In sample “UT”, “CNM” and “V” from Utah, the permeability from approach 3 are lower than values obtained from approaches 1, and 2.

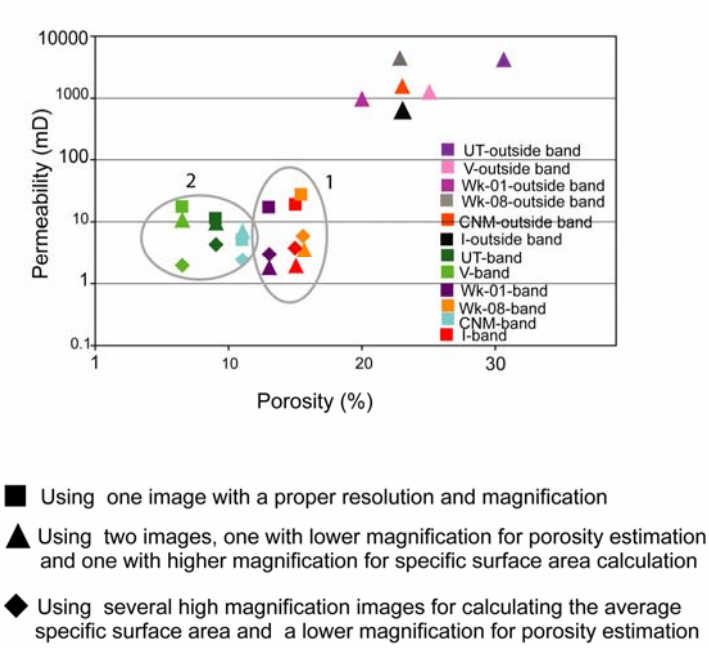

Figure 6. Permeability versus porosity as estimated by using the image processing method described in this article. Three different approaches have been applied on the deformation bands. For outside the bands, the approach #2 has been used. The method has been applied on a single image with appropriate magnification (squares, approach #1) for both porosity and specific surface area estimation, and on two images, the pervious image for porosity estimation and a high magnification image for estimation of specific surface area (triangles, approach #2). The diamonds are related to the permeability estimated from calculated average specific surface area using several high magnification images that cover the entire width of the deformation band (approach #3). Note the contrast in porosity and permeability within and outside of the band and also the classification of data for deformation bands into two groups. For more detail see Figure 5 and Table 2.

Figure 6 also illustrates that both porosity and permeability have been reduced within the bands. The highest porosity reduction was found for sample UT, where porosity is reduced from ~30% outside the band to ~10% within the band and permeability is decreased up to three orders of magnitude. This variation comes from the first source of anisotropy (macroscopic aspect) induced by deformation band that has been stated in section 2.1.

Table 2 Calculated specific surface area and permeability data using the three different approaches discussed in the text;

sample	Approach	Specific Surface Area (μ)-1	Permeability (mD)
UT-host	2	0.039	4010
Wk-host	2	0.027	1780
Wk-08-host	2	0.022	4301
V-host	2	0.048	1246
CNM-host	2	0.054	756
I-host	2	0.059	626
UT-band	1	0.084	11
UT-band	2	0.091	9
UT-band	3	0.124	4
Wk-01-band	1	0.13	16
Wk-01-band	2	0.405	1.7
Wk-01-band	3	0.349	3
Wk-08-band	1	0.178	17
Wk-08-band	2	0.31	5
Wk-08-band	3	0.386	6
V-band	1	0.054	20
V-band	2	0.07	13
V-band	3	0.1	2
CNM-band	1	0.15	6.9
CNM-band	2	0.17	5
CNM-band	3	0.217	2
I-band	1	0.16	18
I-band	2	0.6	1.7
I-band	3	0.585	2.2

To quantify the microscopic aspect of anisotropy along deformation bands, we have estimated porosity and permeability along one single deformation band (Sample LD-6 from Sinai, Egypt) in two perpendicular thin sections (Figures 2 and 7). We have applied our third approach to calculate permeability for the deformation band in this sample. Porosities in the xz-plane (diamonds in Figure 7) are smaller than porosities in the yz-

plane (about 15% differences). However, permeability values in the xz-plane are up to two orders of magnitude lower than those in the yz-plane.

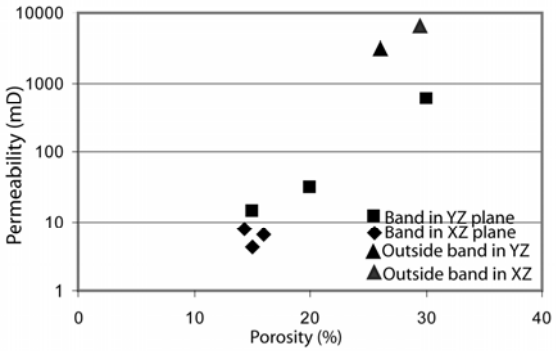

Figure 7. Porosity and permeability obtained from two perpendicular thin sections (xz and yz, see Figure 2) from sample LD-6 (Sinai, Egypt). Note the variations along the band.

We compared our estimated porosities and permeabilities to laboratory measured data obtained from plugs of the same samples. Laboratory measurements of absolute permeability usually involve the direct application of Darcy's law, based on the measurements of individual variables such as flow rate, pressure drop, and sample dimension. Most laboratory measurements are carried out at samples with well-defined geometry, such as cylindrical core plugs, which are generally 2.54 or 3.8 cm (1 or 1.5 inch) in diameter with length varying from 5 to 10 cm (2 to 4 inches) [Dandekar, 2006]. Our estimated porosity and permeability for deformation bands are lower than the laboratory data, regardless of the choice of image processing approach (Figure 8).

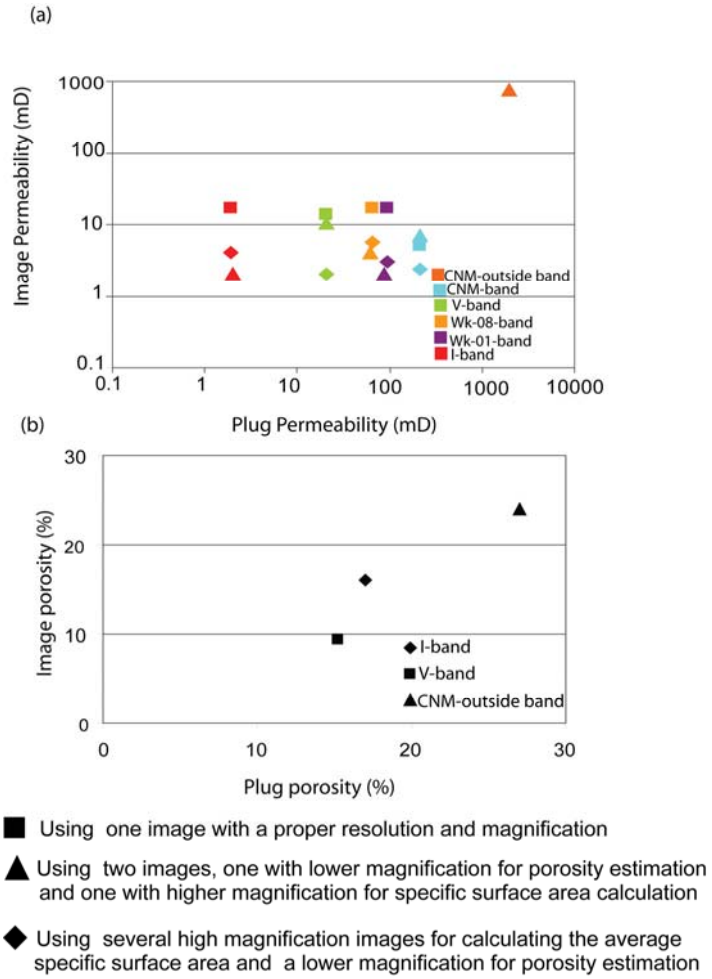

Figure 8. (a) Comparison of laboratory measured and our estimated permeability (b) and porosity. The estimated values are seen to be slightly lower.

4. Discussion and conclusions

Since deformation bands are small-scale structures with about 1 millimeter thickness it is a challenge to obtain their internal properties precisely. Both field and laboratory approaches have their limitations and uncertainties. The thin-section based image analysis technique presented here makes it possible to estimate the properties of the bands themselves. The practical importance of this technique has been demonstrated by combining the measured values of porosity and specific surface area with a Kozeny-Carman relation to obtain estimates of fluid permeability. The main cause of the errors in image processing methods is the discrepancy between thin sections and the actual rock samples; that is, a thin section is only a small part of the rock and can give slightly different statistical parameters [Keehm et al., 2004]. However, this is not the case for deformation bands because of their small thickness. Therefore, image processing technique through thin section analysis is suitable for extracting microstructural information from deformation bands.

In the image analysis technique, the effect of magnification and resolution of the images on the calculated specific surface areas has been investigated. We have resolved the sensitivity of the image processing method to the resolution of the image by using high-resolution images that provide insight into more complex microgeometries. In order to calculate specific surface area Blair et al. [1996] used only one high magnification image from the undeformed sample. Our study shows that a high magnification image is not appropriate for estimating the properties of deformation bands with a relatively wide range of grain and pore sizes. Due to cataclasis and other deformation processes, the microgeometry of most deformation bands is complex. Hence it makes the use of a single high-magnification image that captures only a small area of the anisotropic media inappropriate. To examine the sensitivity of specific surface area in the deformation band to the magnification of the image, we have proposed three approaches. The first uses one low magnification image that covers the whole band, the second applies one high magnification image that contains a small part of the band (Blair et al's [1996] method) and finally the third approach combines several high magnification images in order to cover the thickness of the band. Permeability values obtained from the third approach are different from the values calculated from first and second approaches (Figure 6).

The difference between the two groups of data in Figure 6 can be ascribed to the deformation mechanisms involved during the initiation and development of the bands. In the first group (samples from Sinai), only cataclasis is observed, while in the second group (samples from Utah), both cataclasis and pressure chemical dissolution are present.

We have tested Berryman's [1998] concept on stationary and anisotropic random porous media for deformed sandstones to quantify the permeability variations along the deformation band using 2D images from thin sections with different orientations. We show that the anisotropic deformation bands are not two-dimensional, i.e., the random variations occur both in the xz and yz planes (Figure 2). The main purpose of using 2D images with different orientation is to investigate porosity and permeability variations in different directions and consequently quantifying the porosity and permeability anisotropy induced by deformation bands. We have identified deformation-induced anisotropy in properties such as porosity and permeability in deformed sandstones. This anisotropy occurs at both macro- and microscopic scales in the deformation bands. In this study we point out the microscopic aspect of anisotropy along deformation bands. Based on the presented results (Figure 7), the permeability changes along the band are substantial and the difference is almost two orders of magnitude in the two directions. The permeability values form two different clusters, with higher porosity and permeability in the yz plane. Since deformation bands are long and introduce discontinuities and compartmentalization to fluid reservoirs, studying their microstructure and variations along the bands is significant.

We have used a modified version of Kozeny-Carman relation to calculate permeability. In order to calculate the formation factor, the exponential relationship between formation factor and porosity obtained from an empirical relationship introduced by Archie [1942] was used. Based on the previous studies on the formation factor of sandstones, we have assumed the exponent m in Equation 16 to be equal to 1.8 for our moderately consolidated sandstones. We think the results would be more accurate if we use the lab-measured formation factor for the deformed sandstones in this equation. Our results show that both porosity and permeability decrease as a result of cataclasis and quartz dissolution in the band, but permeability changes are higher up to three orders of magnitude. This can be explained by the increased specific surface area in the band due to the presence of the crushed grains.

Understanding the details of microstructure requires calculation of all correlation functions, but since we have estimated one- and two-point correlation functions (lower

order correlation functions) the estimated permeability values are in the range of possible values. This range is referred to as conventional improved bounds in contrary to rigorous bounds [Torquato 2000].

The difference between plug measurements and our calculated permeability and porosity can be explained by the sample-size limitation inherent to the plug measurements, in which it is difficult or impossible to get the properties of a millimeter-thick deformation band. The laboratory-measured data represent the average properties of the band and its host rock. The method demonstrated here represents a means of finding and mapping variations in permeability along as well as across narrow zones such as deformation bands. This opens new opportunities for research on how deformation bands and similar features affect fluid flow in three dimensions.

Notations

S_n $n = 1,2,...$ N-point correlation function.

r Spatial positions in 2D images.

$f(r)$ Characteristics or indicator function equal to 1 or 0 depending on the position *r*.

ϕ Porosity.

$S_2(x, y)$ Two-point correlation function for distance in Cartesian coordinates

$S_2(r, \theta)$ Two-point correlation function for a distance in polar coordinates.

i, j Pixel positions in 2D BSE images.

k Permeability.

c Constant related to pore geometry.

F Formation factor.

s Specific surface area.

m Archie's cementation factor.

v_g Grain volume.

v_p Pore volume.

Acknowledgements

This study was completed in the frame of Fault Facies Project at the Centre for Integrated Petroleum Research, University of Bergen, and supported by Norwegian Research Council, Statoil, Conoco-Philips, and Statoil. Thanks are due to Alvar Braathen for scientific discussions. Thanks go to Egil Erichsen for help with the SEM analyses and also to Atle Rotevan, Eivind Bastesen, Tore Skar and Silje S. Berg for participating in the collection of some of the samples used in this work.

References

Adler, P. M. (1992), Porous media: Geometry and transport, 544 pp., Butter-worth-Heinemann, Newton, Mass.

Antonellini, M. and A., Aydin (1994), Effect of faulting on fluid flow in porous sandstones: petrophysical properties, AAPG Bull., 78, 355-377.

Archie, G. E. (1942), The electrical resistivity log as an aid in determining some reservoir characteristics, Trans. Am. Ins. Min. Metall. Pet. Eng., 146, 54-62.

Aydin, A., R. I., Borja, P. Eichhubl (2006), Geological and mathematical framework for failure modes in granular rock, Journal of Structural Geology, 28, 83-98.

Bense, V. F., E. H., Van den Berg and R. T., Van Balen (2003), Deformation mechanisms and hydraulic properties of fault zones in unconsolidated sediments; the Roer Valley Rift System, The Netherlands. Hydrogeology Journal, 11, 319-332.

Bakke, S., P. E. Øren (1997), 3-D Pore-scale modelling of sandstones and flow simulations in the pore networks, SPE 35479, 2.

Berge, P. A., J. G., Berryman, S. C., Blair, C., Pana (1997), Scalar properties of transversely isotropic Tuff from images of orthogonal cross sections, UCRL-JC-Lawrence Livermore National Laboratory, Livermore, California 94551-9900.

Berryman, J. G. (1985), Measurement of spatial correlation functions using image processing techniques. J. Appl. Phys., 57, 2374-2384.

Berryman, J. G. (1987), Relationship between specific surface area and spatial correlation functions for anisotropic porous media. J. Math. Phys., 28, 244-245.

Berryman, J. G. (1998), Planar spatial correlations, anisotropy, and specific surface area of stationary random porous media, J. Appl. Phys., 83 (3).

Blair, S. C. and J. G., Berryman (1991), Estimates of permeability and relative permeability for sandstone using image analysis of cross sections, in J. C. Roegiers, Rock Mechanics as a Multidisciplinary Science, Proceedings of the 32nd U.S. Symposium on Rock Mechanics, A. A. Balkema, Rotterdam, 365-374.

Blair, S. C., P. A., Berge and J. G., Berryman (1993), Two-point correlation functions to characterize microgeometry and estimate permeability of synthetic and natural sandstones, Lawrence Livermore National Laboratory, Livermore, California Rep. UCRL-LR-114182.

Blair, S. C., P. A., Berge and J. G., Berryman (1996), Using two-point correlation functions to characterize microgeometry and estimate permeabilities of sandstones and porous glass, J. Geophys. Res., 101(B9), 20359-20375.

Brace, W. E. (1977), Permeability from resistivity and pore shape. J. Geophys. Res., 82, 3343-3349.

Corson, P. (1974), Correlation functions for predicting properties of heterogeneous materials, I, Experimental measurements of spatial correlation functions in multiphase solids, J. Appl. Phys., 45, 3159-3164.

Cule, D. and S. Torquato (1999), Generating random media from limited microstructural information via stochastic optimization, J. Appl. Phys., 86(6).

Dandekar, A. Y. (2006), Petroleum reservoir rock and fluid properties, 460 pp., CRC Press, Taylor and Francis Group.

Debye, P., H. R., Anderson Jr. and H., Brumberger (1957), Scattering by an inhomogeneous solid, II, The correlation function and its application, J. Appl. Phys., 28, 670-683.

Doyen, P. M. (1988), Permeability, conductivity, and pore geometry of sandstone, J. Geophys. Res., 93, 7729-7740.

Du Bernard, X. D., P., Eichhubl, and A., Aydin (2002), Dilation bands: A new form of localized failure in granular media, Geophysical Research Letters 29(24), 2176.

Ehrlich R., S. K. Kennedy, S. J., Crabtree and R. L., Cannon (1984), Petrographic image anlysis: I. Analysis of reservoir pore complexes, Journal of Sedimentary Petrology, 54, 1515-1522.

Fisher, Q. J. and R. J., Knipe (2001), The permeability of faults within siliciclastic petroleum reservoirs of the North Sea and Norwegian Continental Shelf, Marine and Petroleum Geology, 18, 1063-1081.

Flodin, E., A., Aydin, L.J., Durlofsky, B., Yeten (2001), Representation of fault zone permeability in reservoir flow models, Presented at the society of Petroleum Engineers Annual Technical Conference and Exhibition, New Orleans, Louisiana (SPE paper 71671), 10 pp.

Flodin, E., M., Gerdes, A., Aydin and W. D., Wiggins (2005), Petrophysical properties and sealing capacity of fault rock, Aztec sandstone, Nevada, in R. Sorkhabi and Y. Tsuji, eds., Faults and fluid flow, and petroleum traps, AAPG Memoir 85, 197-217.

Fossen, H., R. A. Schultz, K., Mair and Z. K. Shipton (2007), Deformation bands in sandstones - a review, Journal of Geological Society, London, 164, 754-769.

Garboczi, E. J., D. P., Bentz and N. S., Martys (1999), Digital images and computer modelling. Experimental methods in the physical sciences, Methods in the Physics of Porous Media, Chapter 1, Academic Press, San Diego, CA. 35, 1-41.

Gibson, R. G. (1998), Physical character and fluid-flow properties of sandstone-drived fault zones, Geological Society, London 127, 83-97.

Gokhale, A. M. (2004), Experimental Measurements and Interpretation of Microstructural N-Point Correlation Functions, Microsc. Microanal., 10 (Suppl 2), 736-37.

Hesthammer, J. and H. Fossen (2001), Structural core analysis from the Gullfaks area, northern North Sea, Marine and Petroleum Geology 18, 411-439.

Jamison, W. R. and D. W., Stearns (1982), Tectonic deformation of Wingate Sandstone, Colorado National Monument, AAPG Bull., 6, 2584-2608.

Jourde, H., E. A., Flodin, A., Aydin, L. J., Durlofsky and X-H., Wen (2002), Computing permeability of fault zones in eolian sandstone from outcrop measurements, AAPG Bull., 86(7), 1187-1200.

Keehm, Y., T., Mukerji, A., Nur (2004), Permeability prediction from thin sections: 3D reconstruction and Lttice-Boltzmann flow simulation, Geophys. Res. Let., 31, L04606.

Keehm, Y., K., Sternlof, T., Mukerji (2006), Computational estimation of compaction band permeability in sandstone. Geosciences Journal, 10, 4, 499-505.

Knipe, R. J., Q. J., Fisher, G., Jones, M. B., Clennell and A. B., Farmer (1997), Fault seal analysis: Successful methodologies, application and future directions, in P. Moller-

pederson and A. G: Koestler. Hydocarbon seals: Importance for exploration and production. NPF Special Publication, 7, 15-40.

Koplik, J., C., Lin, M., Vermette (1984), Conductivity and permeability from microgeometry, J. Appl. Phys., 56, 3127-3131.

Kwon, O., B. T., I. G., Ngwenya, Main, S. C., Elphick (2005), Permeability evolution during deformation of siliciclastic sandstones from Moab, Utah, in R. Sorkhabi and Y. Tsuji eds., Faults, Fluid flow, and petroleum traps. AAPG Memoir, 85, 219-236.

Lothe, A. E., R. H., Gabrielsen, N., Larsen and B. T., Bjørnevoll (2002), An experimental study of the texture of deformation bands: effects on porosity and permeability of sandstones, Petroleum Geosciences, 195-207.

Martys, N. and E. J., Garboczi (1992), Length scales relating the fluid permeability and electrical conductivity in random two-dimensional model porous media, Phys. Rev., B 46, 10.

Ogilvie, S. R., Paul, W. J. Glover (2001), The petrophysical properties of deformation bands in relation to their microsturcture. Earth and Planetary Science Letters, 193, 129-142.

Otsu, N. (1979), A threshold selection method grey-level histogram, IEEE Transactions on Systems, Man and Cybernetics, 9(1), 62-66

Paterson, M. S. (1983), The equivalent channel model for permeability and resistivity in fluid-saturated rock- A reappraisal, Mech. Mater., 2, 345-352.

Pittman, E. D. (1981), Effect of fault-related granulation on porosity and permeability of quartz sandstones, Simpson Group (Ordovician) Oklahoma, AAPG Bull., 65, 2381-2387.

Sen, P. N., C., Scala and M. H., Cohen (1981), A self-similar model for sedimentary rocks with application to the dielectric constant of fused glass beads, Geophysics 46, 781-795.

Shipton, Z. K., J. P., Evans, K. R., Robeson, C. B., Forster and S., Snelgrove (2002), Structural heterogeneity and permeability in eolian sandstone: Implications for subsurface modeling of faults, AAPG Bull., 86(5), 863-883.

Sigda, J. M., L. B., Goodwin, P. S., Mozely, and J. L.,Wilson (1999). Permeability Alteration in small-displacement faults in poorly lithified sediments: Rio Grande, Central New Mexico in Faults and subsurface fluid flow in the shallow crust, Geophysical Monograph 113, American Geophysical Union.

Sternlof, K. R., J. R., Chapin, D. D., Pollard and L. J. Durlofsky (2004), Permeability effects of deformation band in arrays in sandstone. AAPG Bull., 88, 9, 1315-1329.

Torquato, S. and M. D., Rintoul (1995), Effect of the interface on the properties of composite media, Phys. Rev. Lett., 75, 4067-4070.

Van der Marck, S. C. (1993), Comment on" using two-point correlation functions to characterize microgeometry and estimate the permeabilities of sandstones and porous glass" by Stephan Blair, Patricia Berge, and James G. Berryman. J. Geoph. Res. 102(B11), 24811-24812.

Walsh, J. B. and W. F., Brace (1984), The effect of pressure on porosity and the transport properties of rock, J. Geophys. Res., 89, 9425-9431.

Walsh, J. J., J., Watterson, A., Heath, P. A., Gillespie and C., Childs (1998), Assessment of the effects of sub-seismic faults on bulk permeabilities of reservoir sequences. Geological Society, London, Special publication, 127, 99-113.

White, J., A., R. I., Borja, J. T., Fredrich (2006), Calculating the effective permeability of sandstone wit multiscale lattice Boltzmann/finite element simulations. Acta Geotechnica, 1, 195-209.

Wissler, T. M. (1987), Sandstone pore structure: A quantitative analysis of digital SEM images, PhD. thesis, Mass. Inst. of Technol., Cambridge.

Wong, P. Z., J., Koplik and J. P., Tomanic (1984), Conductivity and permeability of rocks, Phys. Rev., B 30.

Wyllie, M. R. J. (1953), Formation factors of unconsolidated porous media: influence of particle shape and effect of cementation, Trans. AIME 198, 103-110.

Yeong, C. L. Y. and S., Torquato (1998), Reconstructing random media, Phys. Rev., E 495-506.

Paper 4

Torabi, A., and Fossen, H., 2007. Spatial variation of microstructure and petrophysical properties of deformation bands. Under review in Journal of Structural Geology.

Spatial variation of microstructure and petrophysical properties of deformation bands

Anita Torabi, Haakon Fossen

Department of Earth Science, University of Bergen, and Centre for Integrated Petroleum Research, Post Box 7800, 5020 Bergen, Norway

Corresponding author: Anita Torabi, anita.torabi@cipr.uib.no

Abstract

A series of deformation bands from various sandstones deformed at different depths have been studied with respect to microstructural and petrophysical variations. We have found that the internal microstructure of many deformation bands varies along the bands at the cm or even mm scale. The variations can result in variations in petrophysical properties such as porosity and permeability. In the examples explored, porosity varies by up to 18% and permeability by up to two orders of magnitude within deformation bands. Such petrophysical variations are found in different types of deformation bands, but the range depends upon the deformation mechanisms, in particular on the degree of cataclasis and dissolution in cataclastic and dissolution bands, and on the phyllosilicate content in disaggregation bands. Moreover, the grain size distributions change along the bands with regard to the degree of cataclasis. Furthermore, the increased specific surface area of the pore-grain interface as a result of cataclasis in the cataclastic bands causes more permeability reduction compare to other types of deformation bands. Phyllosilicate content can also influence the thickness of the phyllosilicate bands. However, there is no apparent correlation between thickness and intensity of cataclasis in the studied cataclastic deformation bands.

1. Introduction

Deformation bands are localized deformed microstructures that form in highly porous rocks and sediments. They are commonly found in faulted sand and sandstone (e.g. Aydin, 1978; Pittman, 1981; Jamison and Stearns, 1982; Underhill and Woodcock, 1987; Knipe, et al., 1997, Fossen et al., 2007). Their internal characteristics have the

potential of changing the petrophysical properties of reservoirs dramatically and thus affect the choice of production strategy of oil and gas fields (Fisher and Knipe, 2001; Hesthammer and Fossen, 2001; Ogilvie and Glover, 2001).

Deformation bands form by different deformation mechanisms (Fossen et al., 2007). Disaggregation bands result from granular flow at shallow burial depth that involves rolling, sliding and rotation of sand grains. These bands do not usually affect the petrophysical properties of the deformed sandstone significantly (e. g. Rawling and Goodwin, 2003). Phyllosilicate bands are a special subgroup of disaggregation bands that form by granular flow in sand or sandstone where the phyllosilicate content exceeds 10-15% (Knipe et al., 1997). Phyllosilicate bands cause up to several orders of reduction in permeability according to plug measurements reported by Fisher & Knipe (2001). Cataclastic deformation bands are characterized by grain fracturing, crushing and abrasion (cataclasis). Individual cataclastic bands are typically reported to reduce porosity of the deformed sandstone by one and permeability by three orders of magnitude as compared to their host rock (Antonellini and Aydin, 1994). Dissolution and cementation bands form where dissolution or cementation is the dominant deformation mechanism. A dissolution band typically consists of tightly packed quartz grains with little or no indication of fracturing of the grains (Gibson, 1998). Dissolution and quartz cementation have been suggested as an explanation for poor reservoir performance in North Sea reservoirs located at >3 km depth (Hesthammer et al., 2002).

Single deformation bands are typically about one millimeter thick and up to a hundred meters long. They can grow into clusters of deformation bands in which faults can initiate, as envisaged by Aydin and Johnson (1978). Clusters of bands can accumulate several hundred bands over a zone less than a meter wide (Johansen and Fossen, in press), in which case the zone can be several hundred meters long. They can also form and grow in the damage zone of an existing fault, for instance as a response to geometric complications during fault slippage (e.g. Rykkelid and Fossen, 2002).

Since deformation bands and deformation band zones are long enough to compartmentalize reservoirs, their physical properties have been devoted attention by a number of previous workers (e.g. Aydin 1978; Pittman, 1981; Jamison and Stearns, 1982; Underhill and Woodcock, 1987; Knipe, 1997; Gibson, 1998; Fisher and Knipe, 2001). However, variations in porosity and permeability, related to microstructural variations within deformation bands, have been given little or no attention in the existing literature (cf. Fossen and Bale, 2007). The typical reported cataclastic deformation bands

of the Colorado Plateau, as described by Aydin (1978), Aydin & Johnson (1978, 1983) and Davis (1999), form where mechanical grain fracture is the dominant deformation mechanism. These authors described deformation bands as consisting of a central cataclastic core within a volume of compacted rock. Variation of microstructure across the band has also been studied through experimental work (e.g. Agung et al., 2004). Sharp boundary shear zones produced at high level of stress in ring shear experiments (Torabi et al., 2007) show zonation comparable to the microstructural variation reported by Aydin (1978). In these experiments, porosity varied from ~24% in the host rock down to ~17% in the margin and to ~12% within the central part of the shear zone (Torabi et al., 2007). Furthermore, variations in microstructure, and therefore in porosity and permeability along the band, must be addressed when their effect on fluid flow is considered.

While microstructural variations along as well as across deformation bands are easily studied under the microscope, their internal permeability structure is difficult to assess by means of classical methods. In general, image processing methods can be used to characterize the microstructure of rocks and provide a quantitative means for understanding the dependence of physical properties on pore structure (Ehrlich et al., 1984; Wissler, 1987; Koplik et al., 1984; Doyen, 1988; Blair et al., 1996, Bakke and Øren, 1997; Keehm et al., 2004; 2006; White et al., 2006; Wu et al., 2006). In the present study we use an image processing method especially designed for the purpose of estimating porosity and permeability within deformation bands (Torabi et al., in review). In order to see the effect of grain size on microstructure of the bands, we describe the grain size distributions in the measured locations in the host rock and within the bands. We first exemplify different types of deformation bands with respect to their deformation mechanism from different localities around the world that show variations in thickness, microstructure and properties such as porosity and permeability along the band and then present a case study from the Entrada Sandstone (Utah, USA) to show variations along deformation bands as they cross layers of different grain size and porosity.

2. Methodology

Traditionally, laboratory-based plug and mini-permeameter data represent one-dimensional properties of deformation band and its host rock. Image processing methods, on the other hand, provide a means to estimate porosity and permeability on the micro-scale, and to map out the variations in properties along as well as across deformation bands. In the current project, polished thin sections of faulted sandstones have been studied by optical and scanning electron microscope and high-resolution Backscattered electron (BSE) images have been taken. Porosity and permeability have been estimated using spatial correlation functions and a modified version of Kozney-Carman relation (Torabi et al., in review). In the image processing method, we make a binary image from the selected high-resolution gray-scale BSE image by choosing an appropriate threshold. The binary image has been reversed to have '0' pixel value in the grain space and '1' in the pore space. The binary image ($f(ij)$) is represented by a $M \times N$ matrix. The one point correlation function (Eq. 1) is applied to the binary image (S_1), which gives information about the volume fraction of the two phases i.e. pore and grain is (Garboczi et al., 1999):

$$S_1 = \phi = < f_{(i,j)} > = \frac{1}{MxN} \sum_{ij} f_{(i,j)} \qquad (1) \qquad i = 1,2,...M; \qquad j = 1,2,...N$$

This function gives the porosity. The next step is to calculate the pore-pore two point correlation function, $S_2(x,y)$ for the binary image by using Eq. 2, that is the probability that two points with a specified distance apart (a line) are both in pore phase (Berryman 1986; Torquato, 1999).

$$S_2(x,y) = < f_{(i,j)} f_{(i+x,j+y)} > = \frac{1}{MxN} \sum f_{(i,j)} f_{(i+x,j+y)} \qquad (2)$$

The specific surface area (Eq. 3) of the pore-grain interface is calculated from the two-point correlation function (Berryman, 1998). We calculated permeability by using a modified version of the Kozeny-Carman relation (Eq. 4), where ϕ is the porosity and c is a constant related to pore geometry that is equal to 2 for porous materials assuming circular cross section for pores, F is the formation factor and has an exponential relationship with porosity (Archie, 1942);

$$S_2'(0) = -\frac{s}{4} \qquad (3)$$

$$k = \phi^2 / cFs^2 \qquad (4)$$

Grain size distributions have been analyzed from binary images of high resolution BSE images using ImageJ software. The obtained grain size areas were calibrated in square micrometers by setting the real scale on the images. The grain size distributions are presented as exceedence frequency plots for all the thin sections. Exceedence Frequency (EF) of a particular value of a measured variable is defined as the number of data with values greater than that value, divided by the total number of the data (Torabi et al., 2007).

3. Results from thin section study

In this section we quantify the spatial variation of grain size, porosity and permeability within the deformation bands through microstructural study of: (i) different types of deformation bands associated with different deformation mechanisms and (ii) deformation bands from the Entrada Sandstone from San Rafael Desert, Utah, to show the effect of initial grain size and porosity on properties of the bands where they cross different layers.

3.1. Deformation bands and deformation mechanisms

Deformation mechanisms in porous sand and sandstones depend on factors such as mineralogy, grain size, shape, sorting, cementation, porosity and state of stress and strain (Fossen et al., 2007). Different mechanisms produce bands with different petrophysical properties, and the primary mechanisms are (1) granular flow; (2) cataclasis; (3) dissolution and cementation (Fossen et al., 2007). In general, granular flow characterizes deformation of sand and sandstone at shallow depths.

Figure 1a shows a deformation band formed by granular flow, identified as a phyllosilicate band on the right-hand side of the image. The sandstone sample was taken from the Brent Group in the North Sea Huldra Field. The sample is from 3701 m depth, but formed at less than a few hundred meters burial during the late Jurassic North Sea

rifting event. There are changes in porosity and permeability both along and across the band as its phyllosilicate (mica) content varies (Fig. 1a); the phyllosilicate content is so low in the left half of the band that it is difficult to trace. On the other hand, the band is thicker in the right part where the phyllosilicate content is high.

The highest porosity and permeability values were obtained in the host rock where the phyllosilicate content is low (21% and 210 mD, respectively) and within the left (non-phyllosilicate) part of the band (22% and 133 mD). Hence, there is no porosity contrast, and the permeability contrasts is insignificant in the left portion of the band in Fig. 1a. This stands in stark contrast to the phyllosilicate-rich right-hand part of the band (11% and 0.4 mD) where permeability has been reduced by almost three orders of magnitude (Fig. 1a, 2). Grain size distributions for host rock and within the phyllosilicate-poor left part of the band are almost identical, suggesting that this part of the band is a disaggregation structure. We have not analyzed the grain size in the phyllosilicate-rich portion of the band. This example complies with previous findings that phyllosilicate content controls the permeability across disaggregation bands (e.g. Fisher and Knipe, 2001). More importantly, this also demonstrates how variations in phyllosilicate content of the host rock impose rapid variations in relative permeability and porosity between the host rock and the deformation band.

The second example is from the Entrada Sandstone of the San Rafael Desert, Utah, USA. The approximate burial depth at the time of deformation was around 3 km (Aydin, 1978; Davatzes, et al., 2003). The sampled sandstone is fine-grained, well sorted, and exhibits dissolution at quartz grain-contact points within the band (Fig. 1b). However, thin section studies have not revealed any quartz overgrowth in this sample. Further, the microstructure of the band is different from the classical deformation bands studied by Aydin (1978) at the same locality. Due to the dissolution and mild cataclasis in the band, the initial grain size as well as porosity and permeability have been reduced (Fig. 1b, 2).

The grain size distributions along the band are almost identical, except for location number 2, which belongs to the thickest part of the band and has the lowest porosity (Fig. 1b). Also, the permeability changes along the band in this example. The permeability contrast to the adjacent host rock varies from one order (minimum reduction) to three orders of magnitude, as shown in Figs. 1b and 2. Apart from location No.2 in the band, the porosity and permeability changes do not correlate with variations in band thickness, e.g. locations No. 5 and 6 show approximately the same thickness

while location 5 has a porosity value twice that of No. 6 and a permeability that is higher by two orders of magnitude.

The third and fourth thin sections are from medium grained and poorly sorted Nubian sandstone (Wadi Khaboba, Sinai, Egypt). The maximum burial depth at the time of faulting was about 1.5 km (Du Bernard et al., 2002; Rotevatn et al., 2007). Both sections were prepared perpendicular to each other from the same sample. They show variation in microstructure along the band in both directions, related to the intensity of cataclasis and amount of iron oxide cement. This affects the grain size distributions, porosity and permeability (Fig. 1c, 1d).

For the host rock, there are differences in grain size distributions between LD-6A1 and LD-6A2. The estimated host rock porosity and permeability in LD-6A1 are 30% and 8945 mD, respectively; while the corresponding values for LD-6A2 are lower (26% and 4864 mD, respectively). Minimum porosity and permeability is found in a part of the band LD-6A1 characterized by intense cataclasis and iron oxide cement (6% porosity and 1.7 mD permeability). In the rest of the band (LD-6A1), porosity does not change and permeability changes are small. Overall porosity and permeability inside the band are lower in LD-6A1 than in LD-6A2, likely related to more intense cataclasis in LD-6A1. Both porosity and permeability change along the band in LD-6A2, but permeability changes are higher, ranging from 14 mD to 1238 mD, i.e. a variation of two orders of magnitude (Fig. 1d, 2). Contrary to petrophysical properties, band thickness remains almost constant for LD-6A2 sample. Moreover, the changes in thickness of the band in LD-A1 do not correspond to the degree of cataclasis and petrophysical properties measured along the band.

The last example is from a medium to coarse-grained and poorly sorted version of the Nubian sandstone from Sinai, Egypt. This sample is from the same locality as the sample in Figs. 1c and 1d, but shows intensive cataclasis and grain size reduction that vary along the band (Fig. 1e). The permeability has been reduced by up to 4 orders of magnitude, from very high permeability of in the host rock (19157 mD) down to 4 mD within the band (Fig. 2). The porosity changes from a maximum of 30% in the host rock to 17% within the band (Fig. 1e). Porosity and permeability measurements also show variations along the band with ranges from 28% to 17% and from 673 mD down to 4 mD, respectively (Fig. 1e).

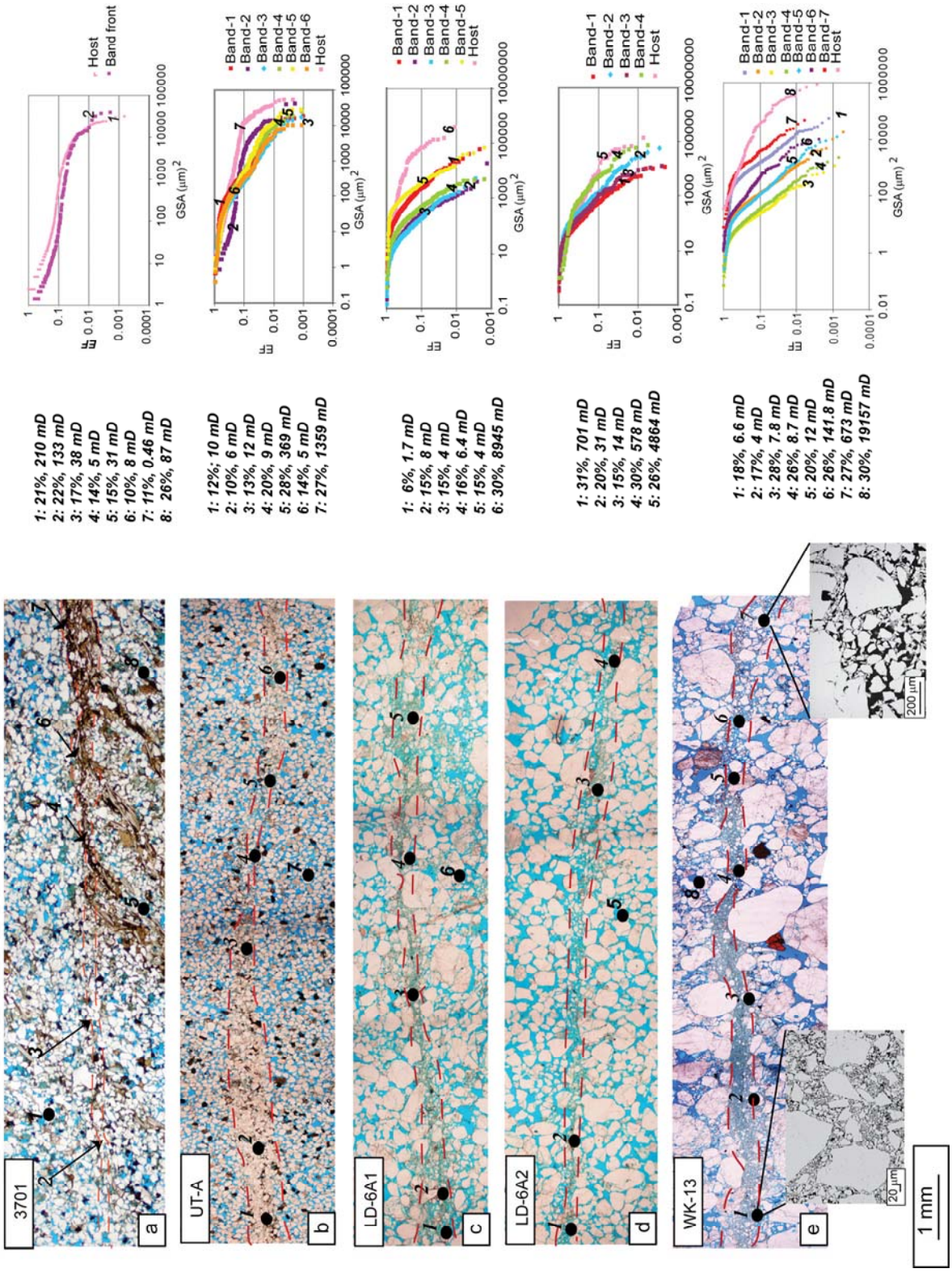

Fig.1. Photomicrographs of thin sections of deformation bands (left), porosity and permeability values for measured locations (middle) and plots of grain size distributions (right). On each photograph, the locations are noted. The numbers on the thin section images correspond to the numbers used in presentation of the porosity and permeability data and grain size distributions. (a) Phyllosilicate band (sample 3701); (b) dissolution band (sample UT-A); (c) cataclastic band (sample LD-6A1); (d) cataclastic band (sample LD-6A2); (e) cataclastic band (WK-13).

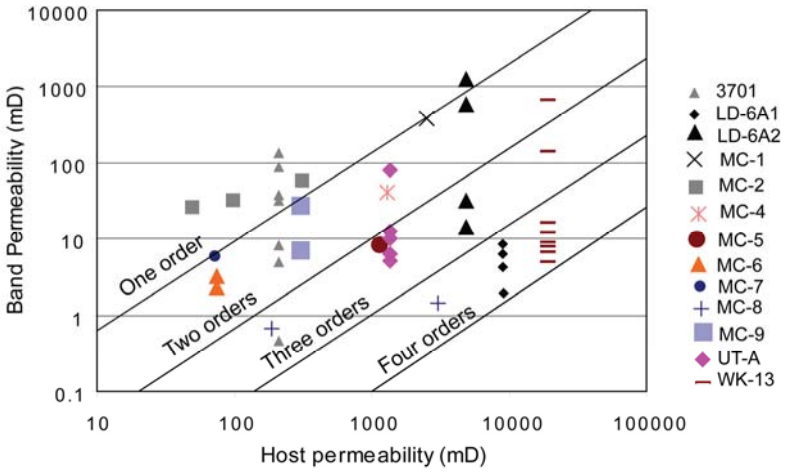

Fig.2. Plot of measured permeability values within deformation bands versus host rock permeability. Note to the reductions in permeability by up to four orders of magnitude in the deformation bands.

The grain size analyses show reduction of the grain size area in the band compare to the host rock (Fig. 1e), although the grain size area varies also along the band. Again, the thickness variation does not correlate with the change in microstructure and petrophysical properties (Fig. 1e). This is shown by the fact that the selected locations in the beginning and end of the band show similar thickness, but the grain size distribution and porosity and permeability values are different. High magnification images (Fig. 1e) reveal different microstructures and grain size distributions for these two parts implying different degree of cataclasis.

3.2. Effect of initial grain size and porosity

The influence of initial grain size and porosity of the host rock on the development of deformation band microstructure and properties were explored through a study of deformation bands that cross nine definable layers at the base of an eolian sand unit in the Entrada Sandstone in the San Rafael Desert, Utah, USA, (Fig. 3). The burial depth is thought to be around 3 km at the time of deformation (Aydin, 1978; Davatzes, et al., 2003). The grain size is generally fining upward through these layers, but detailed analyses show the grain size and porosity to change at the scale of a single thin section (Figs. 4 and 5).

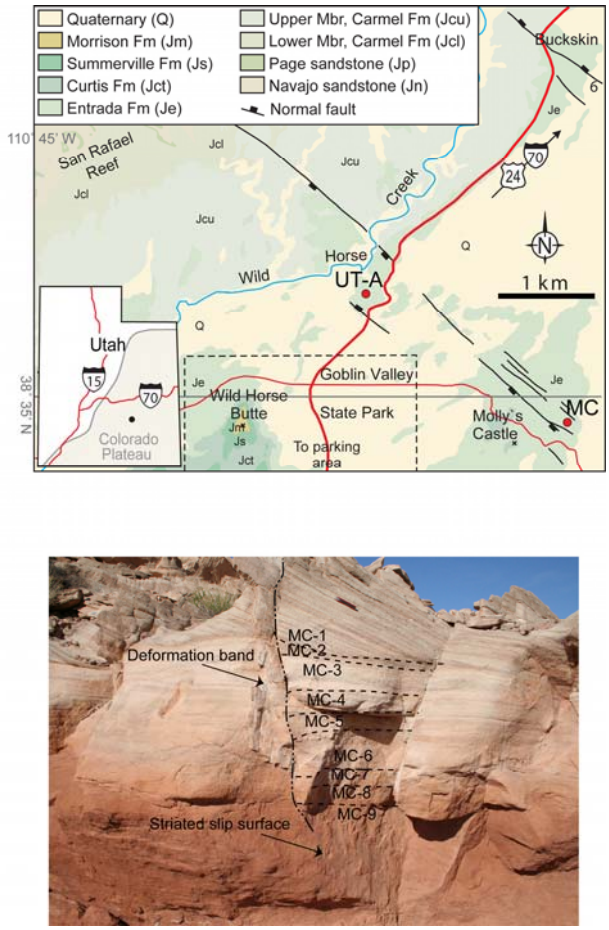

Fig.3. (a) Geologic map showing the studied locality in the San Rafael Desert, Utah, USA (MC) and the location for sample UT-A. Modified from Johansen & Fossen (in press). (b) A picture from the locality where the MC samples were taken. Knife on the picture is for scale.

In the upper layer (MC1 in Figs. 3 and 4a), the sandstone is medium-grained and well sorted. The grain size distribution is almost constant in the host rock but is reduced somewhat within the band due to mild cataclasis. The thickness of the band varies, especially on the right-hand side of Fig. 4a where the band is hard to define. Porosity changes from 25% in the host rock to 20% inside the band, while permeability decreases from 2517 mD to 384 mD, i.e. about one order of magnitude (Fig. 2).

In the thin section from the next layer (MC2 in Figs. 3 and 4b), the sandstone is very poorly sorted and has several fine-grained laminas. Cataclasis is the main deformation mechanism in this band. Contribution of the fine-grained laminas to the band locally reduces the grain size area of the band and affects porosity and permeability (Fig. 4b). Porosity and permeability do not change significantly from the fine-grained laminas in the host rock to the parts of the band containing the fine-grained laminas (Fig. 4b). On the contrary, the permeability of the coarse-grained host rock outside the band is one order of magnitude higher than the coarse-grained portion of the band (Fig. 2, 4b). It

is not easy to trace the band in the right hand side of the section in Fig. 4b, where it seems to be a zone of deformation with a somewhat lower porosity and permeability than its surroundings (Fig. 4b).

In layer MC3 (Fig. 3), the thin section only shows the deformed sandstone and therefore it is difficult to compare the grain size area, porosity and permeability within and outside the band (Fig. 4c). The grain size distribution is bimodal in that it contains a considerable amount of both fine and coarse grains (Fig. 4c). Porosity and permeability are lower than the estimated values from layers MC1 and MC2 (Fig. 4c), suggesting a higher degree of cataclasis in this sample.

The sandstone in the fourth layer (MC4 in Fig. 3) is poorly sorted and the grain size distribution both outside and inside the deformation band is bimodal (Fig. 4d). Porosity is slightly decreased whereas permeability is reduced by up to two orders of magnitude within the band as a result of mainly cataclasis (Figs. 2 and 4d). The band has a fairly constant thickness. The thin section from the fifth layer (MC5 in Fig. 3) shows the sandstone to be poorly sorted (Fig 4e). The band shows a fairly constant thickness and the grain size analysis reveals a bimodal distribution and also grain size reduction in the band (Fig. 4e). This reduction is related to the low to moderate amount of cataclasis. Similar to the previous bands, there are small porosity changes while permeability varies up to three orders of magnitude (Fig. 2, 4e).

In the thin section from layer MC6 (Fig. 5a), there are two branching bands in the left-hand part. The thin section shows a very poorly sorted sandstone with finer grain size areas around two bands. However, the grain size distributions along these bands are identical (Fig. 5a). The highest permeability reduction in these bands is one order of magnitude (Fig. 2). Porosity decreases from 20% down to 13% and 14% within the bands (Fig. 5a). The bands in this layer also show evidence of cataclasis. The thin section from layer MC7 (Fig. 5b) illustrates poorly sorted sandstone with a high content of iron oxide. The grain size has obviously been reduced (Fig. 5b) in the band. Furthermore, porosity is reduced by 2% and permeability by one order of magnitude compared to the host rock (Fig. 2). Both cataclasis and iron oxide cement are present in this band. In the sample from layer MC8 (Fig. 3), the sandstone is seen to be poorly sorted. The boundaries of the band are sharp and easily definable in the BSE images (Fig.5c).

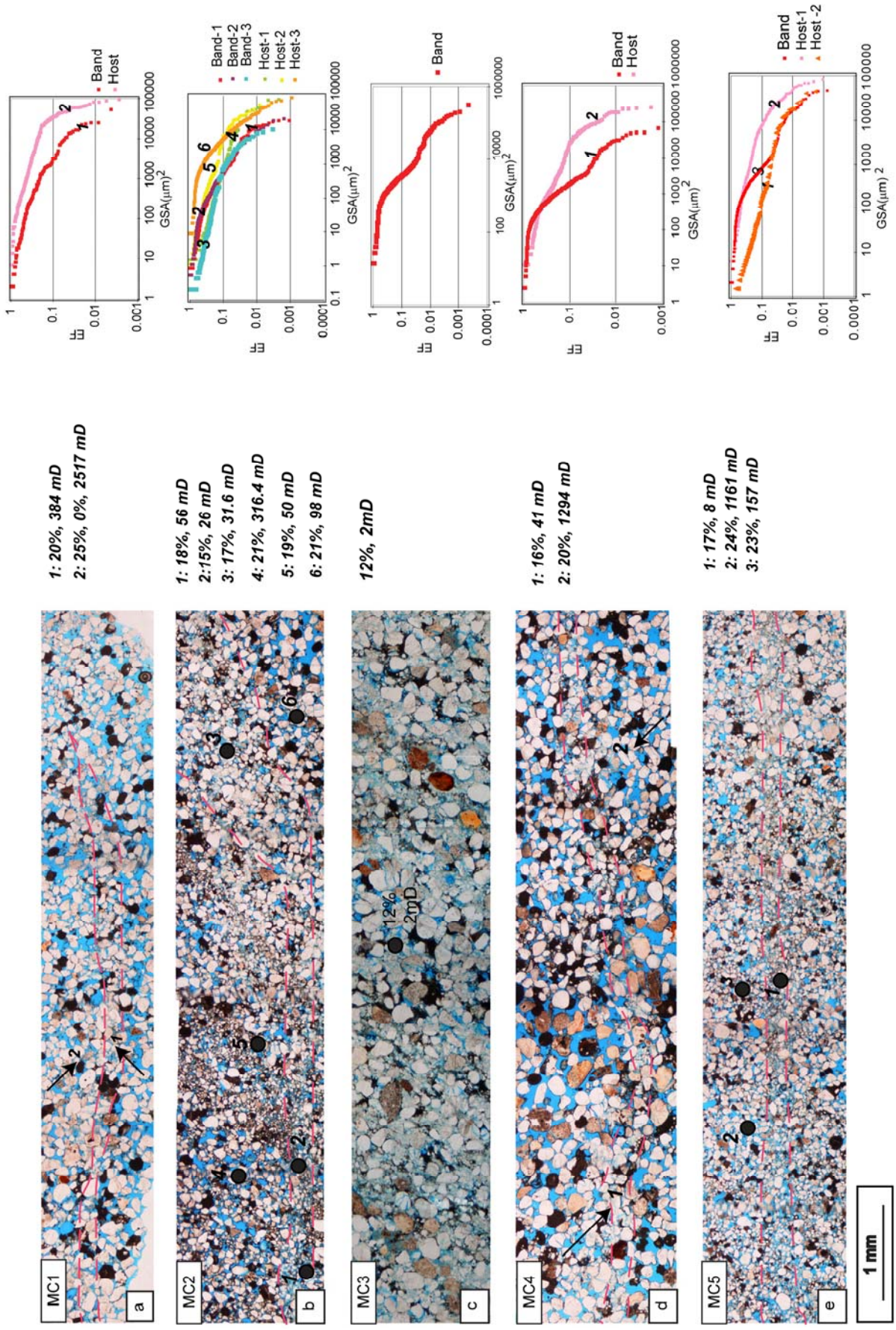

Fig.4. Photomicrographs of MC 1-5 thin sections (left), porosity and permeability values for measured locations (middle) and plots of grain size distributions (right). On each photograph, the locations are noted. The numbers on the thin section images correspond to the numbers used in the presentation of the porosity and permeability data and grain size distributions.

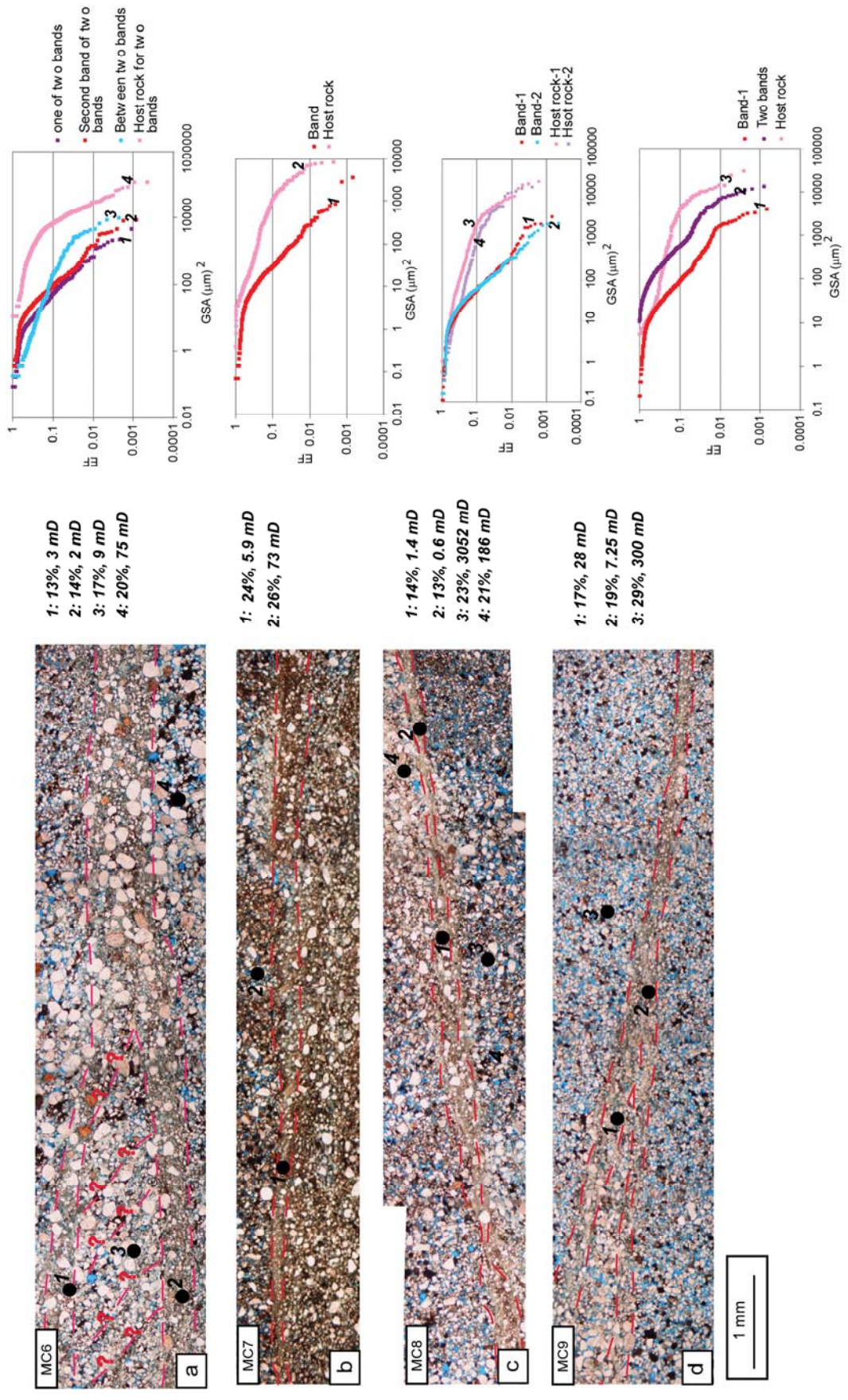

Fig.5. Same as Fig. 4, but for samples MC 6-9.

This can be explained by the intense cataclasis in this band. The grain size analysis (Fig. 5c) shows two different grain size distributions in the host rock. The one obtained from loc. 4 is finer than that from loc. 3 in Fig. 5c. As it is expected, porosity and permeability are higher in the coarse host rock than fine one. Two measured locations in the band show almost similar grain size distribution and porosity, whereas permeability is one order of magnitude lower in loc. 2 than loc. 1 (Figs. 2 and 5c).

In the section from layer MC9, two bands merge into a single thin band (Fig. 5d). The sandstone is fine-grained and poorly sorted. Grain size area is finer in the merged bands than in the individual branches (Fig. 5d). Porosity decreases by up to 12 % in the band compared to the host (Fig. 5d). Permeability is low outside the band, but still decreases by up to two orders of magnitude into the band (Fig. 2).

4. Discussion

Most previous workers address deformation bands and the reduction in permeability across them from a one-dimensional perspective. In this work we have explored how deformation bands show significant internal variations along the bands, by analyzing thickness, microtexture and petrophysical properties.

4.1. Band thickness

Experimental and numerical studies show that the thickness of shear deformation bands depends on grain size, grain angularity, and initial density and confining pressure (Bésuelle, 2001; Haied et al., 2000; Bied et al., 2002; Alsaleh, et al., 2006; Alshibli et al., 2006). The presence of coarse, non-fractured grains in the bands, e.g. the intact coarse grain in each of the bands in Figs. 1c, d and e, affects the thickness of the bands. The presence of intact coarse grains in the middle of cataclastic bands can be explained by the fact that selective fracturing of relatively large grains is favored at high confining pressures during shearing (Blenkinsop, 1991). For the examples presented here, the confining pressure may not be sufficient to cause fracturing of the largest grains. Our observations also show that the band is thicker where the mica content is high in the phyllosilicate band (Fig. 1a).

Numerical modeling of strain localization in granular material shows that shear band thickness tends to reduce as a result of increasing confining pressure (Alsaleh et al.,

2006; Alshibli, et al., 2006). Furthermore, the results from ring shear experiments reveal that increasing the level of normal stress (corresponding to confining pressure) can change diffuse boundary shear zone to sharp boundary ones implying reduction in their thickness (Torabi et al., 2007). In this light, the natural deformation bands studied here formed at different confining pressures. However, for each band confining pressure and bulk strain is basically constant at the scale of observation during the formation of the deformation bands. Rather, the variations in microtexture and degree of cataclasis along the bands can be ascribed to variations in strain within the bands, i.e. stronger strain localization implies more cataclasis. More exactly, in the studied samples the level of strain localization is not simply related to the thickness of the band. For instance, the two selected parts of the band in Fig. 1e have almost the same thickness but show different degree of cataclasis and hence different grain size and petrophysical properties.

4.2. Deformation mechanism

Initial porosity and grain size are important factors influencing the deformation mechanism (Wong et al., 1997; Flodin et al., 2003). The MC samples, collected from layers with different grain size and porosity, all show clear evidence of cataclasis, but the degree of cataclasis changes from one layer to the next based on grain size analyses (Figs. 4, 5).

The effect of phyllosilicate content and cement on deformation mechanism during the deformation of granular material has received attention (e.g. Trent, 1989; Yin and Dvorkin, 1994; Antonellini et al., 1994; Flodin et al., 2003). Antonellini et al. (1994) reported that deformation band tends to be narrow and localized where the host rock phyllosilicate content is high. They also found that the thickness of the phyllosilicate bands depends on the amount of offset they accommodate. However, the offset in the phyllosilicate band in Fig. 1a can be considered to be constant at the scale of the thin section, thus eliminating this effect in our examples. Rather, the porosity and permeability reduction found in the phyllosilicate band in Fig. 1a depend on the continuity and phyllosilicate content of the band: the porosity and permeability values are lower where the band has higher phyllosilicate content. This is well illustrated by location No.7 in Fig. 1a, which has 11% porosity and 0.4 mD permeability.

Cemented granular material are found to be more resistant to grain crushing as compared to the same uncemented material for the same loading and confining pressure

(e.g. Trent, 1989; Yin and Dvorkin, 1994). Quartz dissolution and iron oxide cement in deformation bands hinder cataclasis by increasing the bounding surface of the grains and hence distributing the contact forces over a larger area (e.g. bands in Fig. 1b, 1c, 1d). On the other hand, iron oxide also can reduce the friction between grains, promoting grain boundary sliding (Underhill and Woodcock, 1987).

The timing of deformation relative to any chemical dissolution and cementation is also important (e.g., Eichhubl et al., 2006). Dissolution and cementation decrease porosity and permeability in the band (Figs. 1, 4 and 5) and post-deformational dissolution can clearly be variable along bands. Our observations show that dissolution hinders cataclasis and thereby the mild cataclasis in the studied dissolution bands makes its microstructure different from classical deformation bands reported from the same area in San Rafael Desert, Utah, provided that the dissolution is not post-kinematic.

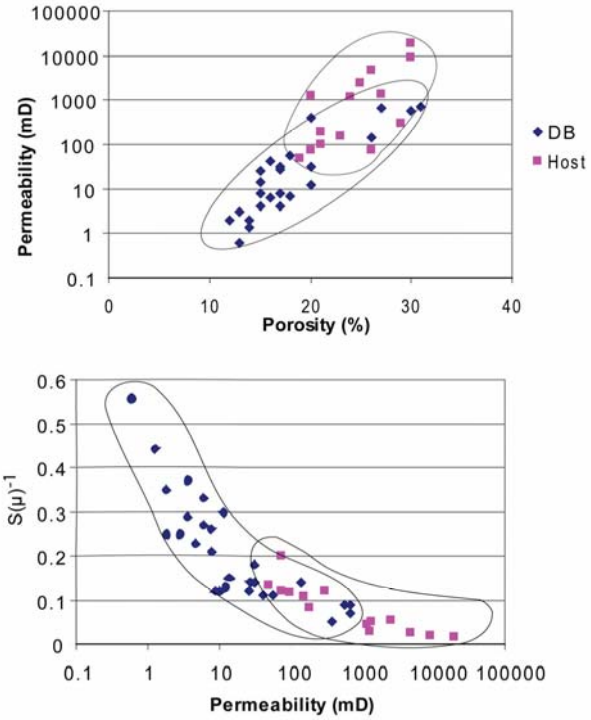

Fig.6. (a) porosity-permeability relationship in the studied cataclastic deformation bands and their host rock; (b) relationship between (s) specific surface area of the pore-grain interface and permeability for the deformation bands and their host rock; Higher specific surface area implies lower permeability values. Note to the different trends for bands and the host rocks in both plots.

We have investigated the relationship between porosity and permeability in the cataclastic deformation bands and their host rock. It has been suggested before that there

is no direct relationship between porosity and permeability because permeability depends on the connectivity of pores (Dandekar, 2006). By comparing the porosity-permeability data for the cataclastic deformation bands investigated in this study (Figure 6a) we see a clear relationship between the two. The relationship between porosity and permeability is less well-defined for host-rock data (Figure 6a), but a comparison indicates that host rock permeability is higher than deformation band permeability for the same porosity value. Although more data would be needed to quantify this difference, it can be explained in terms of the different processes involved: The microstructure of the host rock is controlled by sedimentary processes and compaction, while that of the cataclastic bands is very much the result of grain crushing, which results in more angular grains and a different grain size distribution (Figs. 1, 4, 5). As a consequence of cataclasis, the specific surface area of pore-grain interface increases (s is calculated from Eq. 3 in the methodology section, see Fig.6b). Therefore, the increased s as result of cataclasis causes more reduction in permeability.

The effect of mean grain size, sorting and porosity on permeability of unconsolidated media through another version of Kozeny-Carman relationship has been previously addressed by Panda & Lake, 1994. They have shown that permeability is sensitive to porosity, mean grain size and sorting for permeabilities higher than 1 Darcy. Moreover, variations in mean grain size contribute more to permeability changes than do variations in porosity or sorting. Our results for the Cataclastic deformation bands with lower permeability values are in agreement with their conclusions.

The present work opens new horizons into detailed understanding of the permeability structure of deformation bands. In order to understand the relationship between deformation mechanism within deformation bands on one side and their microstructure and petrophysical properties on another side, we need to study appropriate experimental and numerical analogues. Examples of other types of deformation bands, such as dilation and compaction bands, have to be studied to investigate the effect of shear in localization, thickness and property variation within the bands.

4.3. Implications for fluid flow

Variations in petrophysical properties along deformation bands influence their role in a petroleum reservoir setting. Deformation bands can act as both conduits and barriers on

microscopic scale, although the latter is more common. The rapid variation in properties along bands even on mm and cm scale, implies that deformation bands may not hold any significant pressure difference along them and probably do not contribute to the sealing capacity of faults, as argued by for example Harper and Lundin (1997). On the other hand, cataclastic bands can affect the petrophysical characteristics of the reservoirs in a production situation, although their influence on productivity strongly depends on the cumulative thickness of the bands as well as their internal reduction in permeability (Fossen & Bale, 2007). Plug permeability measurements across cataclastic bands and dissolution/cementation bands show several orders of variation (Fossen et al., 2007 and references therein). We suggest that the lateral variations in porosity and permeability documented through the image analyses in the current work could explain at least some of this scatter.

Disaggregation bands are effective baffles to fluid flow only if the phyllosilicate content is high and evenly distributed throughout the host rock, which is not generally the case. Hence, the variation in permeability values related to the phyllisilcate content in the band, as exemplified by Fig. 1a, can explain the wide variation in reported permeability values for this type of bands (e.g., Fisher and Knipe, 2001). Thus, different types of deformation bands (cataclastic and non-cataclastic) show spatial variations in petrophysical properties even at the cm-scale, suggesting that different factors control these variations in each case. We have demonstrated how variations in mineralogy, notably phyllosilicate content, can cause significant spatial changes in permeability along disaggregation bands. Secondary cementation can also be variably developed, for instance as a function of clay mineral distribution. The variations documented in cataclastic bands are enigmatic, and more research is required to understand and predict these variations.

5. Conclusions

1. Deformation bands can show rapid variations in microstructure that cause variations in porosity and permeability along the strike and dip of the bands.
2. These variations occur in disaggregation bands, dissolution/cementation bands and cataclastic bands. In particular, the local phyllosilicate content control disaggregation bands in phyllosilicate-bearing sandstones.

3. Our results show that permeability can change from one up to two orders of magnitude over a short (mm-scale) distance within a single band.
4. Phyllosilicate content influences the thickness of the band, i.e. higher phyllosilicate content implies a thicker band.
5. No simple relationship between thicknesses and intensity of cataclasis can be detected in the studied cataclastic deformation bands.
6. The widely scattered distribution of previously reported porosity and permeability data for both phyllosilicate and cataclastic bands is likely caused by the observed spatial variation in petrophysical properties of individual bands. Permeability variations along deformation bands make them unlikely to contribute to the sealing properties of faults. Therefore, we predict they have a restricted influence on hydrocarbon production in most cases.
7. The porosity-permeability relationship in the cataclastic bands is affected by cataclasis and the resulting reduction in size, sorting and roundness of the grains caused by this mechanism. Statistically, this results in lower permeability in the band than in undeformed sandstone of identical porosity.

Acknowledgements

We are grateful to the sponsors of the Fault Facies project (Norwegian Research Council, StatoilHydo, Conoco-Philips) at Centre for Integrated Petroleum Research at the University of Bergen. Thanks to Behzad Alaei for scientific advice in the image processing work. Alvar Braathen is appreciated for comments on an earlier version of the manuscript.

References

Agung, M. W., Sassa, K., Fukuoka, H., Wang, G., 2004. Evolution of shear zone structure in undrained ring-shear tests. Lanslides 1, 101-112.

Alshibli, K. A., Alsaleh, M. J., Voyiadjis, G. Z., 2006. Modelling strain localization in granular materials using micropolar theory, numerical implementation and verification, Int. Anal. Mech. Geomech., 30, 1525-1544.

Alsaleh, M. I., K. A., Alshibi, G. Z., Voyiadjis, 2006. Influence of micromaterial heterogeneity on strain localization in granular materials, International Journal of geomecahnics, Vol. 6, Issue 4, pp. 248-259

Antonellini, M. and Aydin, A., 1994. Effect of faulting on fluid flow in porous sandstones: petrophysical properties, AAPG Bull., 78, 355-377.

Archie, G. E., 1942. The electrical resistivity log as an aid in determining some reservoir characteristics. Trans. Am. Ins. Min. Metall. Pet. Eng., 146, 54-62.

Aydin, A., Johnson, A. M., 1978. Development of faults as zones of deformation bands and slip surfaces in sandstone. Pure and Applied Geophysics, 116, 931-942.

Aydin, A. & Johnson, A. M., 1983. Analysis of faulting in porous sandstones, Journal of Structural Geology 5, 1, 19-31.

Aydin, A., 1978. Small faults formed as deformation bands in sandstone. Pure and Applied Geophysics 116, 913-930.

Bakke, S., Øren, P. E. 1997. 3-D Pore-scale modelling of sandstones and flow simulations in the pore networks, SPE 35479, 2.

Berryman, J. G., 1985. Measurement of spatial correlation functions using image processing techniques. J. Appl. Phys., 57, 2374-2384.

Berryman, J. G., 1998. Planar spatial correlations, anisotropy, and specific surface area of stationary random porous media, J. Appl. Phys., 83 (3).

Blair, S. C., Berge, P.A. & Berryman, J. G., 1996. Using two-point correlation functions to characterize microgeometry and estimate permeabilities of sandstones and porous glass, J. Geophys. Res., 101(B9), 20359-20375.

Blenkinsop, T. G., 1991. Cataclasis and process of particle size reduction. PAGEOPH 136 (1).

Bésuelle, P., 2001 Evolution of strain localization with stress in sandstone: Brittle and semi-brittle regimes, Phys. Chem. Earth, 26, 101-106.

Davis, G. H., 1999. Structural geology of the Colorado Plateau region of Southern Utah. Geological Society of America, Special Papres, 342.

Davatzes, N. C., Aydin, A., Eichhubl, P., 2003. Overprinting faulting mechanisms during the development of multiple fault sets in sandstone, Chimney Rock fault array, Tectonophysics, 363, 1-18.

Doyen, P. M., 1988. Permeability, conductivity, and pore geometry of sandstone, J. Geophys. Res., 93, 7729-7740.

Dandekar, A. Y., 2006. Petroleum reservoir rock and fluid properties, 460 pp., CRC Press, Taylor and Francis Group.

Ehrlich R., Kennedy, S. K., Crabtree, S. J. & Cannon, R. L., 1984. Petrographic image anlysis: I. Analysis of reservoir pore complexes, Journal of Sedimentary Petrology, 54, 1515-1522.

Fisher, Q. J. & Knipe, R. J., 2001. The permeability of faults within siliciclastic petroleum reservoirs of the North Sea and Norwegian Continental Shelf. Marine and Petroleum Geology, 18, 1063-1081.

Fossen, H., Schultz, R. A., Mair, K. and Shipton, Z., 2007. Deformation bands in sandstones- a review, Journal of Geological Society, London, 164, 755-769.

Fossen, H. & Bale, A., 2007. Deformation bands and their influence on fluid flow. AAPG Bulletin, December issue in press.

Garboczi, E. J., Bentz, D. P. & Martys, N. S., 1999. Digital images and computer modelling. Experimental methods in the physical sciences, Methods in the Physics of Porous Media, Chapter 1, Academic Press, San Diego, CA. 35, 1-41.

Gibson, R. G., 1998. Physical character and fluid-flow properties of sandstone-drived fault zone. Geological Society London, Special Publication 127, 83-97.

Haied, A., Kondo, D., Henry, J. P., 2000. Strain localization in Fontainbleau Sandstone. Mechanics of Cohesive-Frictional Materials, 5, 239-253.

Harper, T. R. & Lundin, E. R., 1997. Fault seal analysis: reducing our dependence on empiricism. In: Möller-Pedersen, P. & Koestler, A. G. (eds) Hydrocarbon seals-Importance for Exploration and Production. Norwegian Petroleum Society, Special Publication 7, 149-165.

Hesthammer, J. & Fossen, H., 2001. Structural core analysis from the Gullfaks area, Northern North Sea. Marine and Petroleum Geology 18, 411-439.

Hesthammer, J., Bjørkum, P. A. & Watts, L., 2002. The effect of temperature on sealing capacity of faults in sandstone reservoirs: Examples from the Gullfaks and Gullfaks Sør fields, North Sea. AAPG Bulletin.

Jamison, W. R., Stearns, D. W., 1982. Tectonic deformation of Wingate Sandstone, Colorado National Monument. AAPG Bulletin, 66, 2584-2608.

Johansen, T. E. S., Fossen, H. 2008. Internal deformation of fault damage zones in interbedded siliciclastic rocks. Geological Society, London Special Publications, in press.

Keehm, Y., Mukerji, T. & Nur, A., 2004. Permeability prediction from thin sections: 3D reconstruction and Lttice-Boltzmann flow simulation, Geophys. Res. Let., 31, L04606.

Keehm, Y., Sternlof, K., Mukerji, T., 2006. Computational estimation of compaction band permeability in sandstone. Geosciences Journal, 10, 4, 499-505.

Knipe, R. J., Fisher, Q. J. & Clennel, M. R., et al.,1997. Fault seal analysis: successful methodologies, application and future directions. In: Møller- Pedersen, P. & Koestler, A.G. (eds) Hydrocarbon Seals: Importance for Exploration and Production. Norwegian Petroleum Society Special Publication, 7, 15–40.

Koplik, J., C., Vermette, L. M., 1984. Conductivity and permeability from microgeometry, J. Appl. Phys., 56, 3127-3131.

Ogilvie, S. R. & Glover, Paul, W. J., 2001. The petrophysical properties of deformation bands in relation to their microstructure; Earth and Planetary Science Letters, 193, 129-142.

Panda, M., N. & Lake, L. W., 1994. Estimation of single-phase permeability from parameters of particle-size distribution, AAPG Bulletin, 78, 7, 1028-1039.

Pittman, E. D., 1981. Effect of fault-related granulation on porosity and permeability of quartz sandstones, Simpson Group (Ordovician) Oklahoma. AAPG Bulletin, 65, 2381-2387.

Rawling, G. C.& Goodwin, L. B., 2003. Cataclasis and particulate flow in faulted poorly lithified sediments, Journal of Structural Geology, 25, 3, 317-331.

Rotevatn, A., Torabi, A., Fossen, H., Braathen, A., 2007. Slipped deformation bands: a new type of cataclastic deformation bands in Western Sinai, Suez Rift, Egypt, Accpeted by Journal of Structural Geology.

Rykkelid, E. Fossen, H. 2002: Layer rotation around vertical fault overlap zones: observations from seismic data, field examples and physical experiments. Marine and Petroleum Geology, 19, 181-192.

Torabi, A., Braathen, A., Cuisiat, F., Fossen, H., 2007. Shear zones in porous sand: Insights from ring-shear experiments and naturally deformed sandstones. Tectonophysics, 437, 37-50.

Torabi A., Fossen, H., Alaei, B., 2007, Application of spatial correlation functions in permeability estimation of deformation bands in porous rocks. In review, Journal of Geophysical Research (Solid Earth).

Trent, B. C., 1989. Numerical simulation of wave propagation through cemented granular material, in AMD-101, Wave Propagation in Granular Media, eds. D. Karamanlidis and R. B. Stout, 9-15.

Underhill, J. R. & Woodcock, N. J., 1987. Faulting mechanisms in high porosity sandstones; New Red Sandstone, Arran, Scotland, In: Jones, M. E., Preston, R. M. F. (Eds.), Deformation of sediments and sedimentary rocks, Geological Society Special Publication, 29, 91-105.

White, J., A, Borja, R. I., Fredrich, J. T., 2006. Calculating the effective permeability of sandstone wit multiscale lattice Boltzmann/finite element simulations. Acta Geotechnica, 1, 195-209.

Yin, H. & Dvorkin, J., 1994. Strenght of cemented grains, Geophysical Research Letters 21, 10, 903-906.

Synthesis

Synthesis

This dissertation contributes to our detailed understanding of the microstructure of deformation bands and their related petrophysical properties. The papers presented in this dissertation address deformation bands, their microstructure, and evolution; and how they affect porosity and permeability (petrophysical properties) in porous sandstones. Here I synthesize the papers, discussing the findings reported in the individual papers with respect to each other. Implementation of such studies to the geological and simulation models for reservoirs can provide more realistic models. The ultimate goal is improved understanding of hydrocarbon flow within faulted reservoirs.

Progress on deformation band microstructure

We have compared experimentally-produced shear zones that resemble deformation bands to natural deformation bands, acknowledging that the deformation process is to some extent different in the ring-shear experimental apparatus than in natural deformation bands (Paper 1). The key difference is that in the ring-shear experiments the displacement and strain rate are far larger than in the natural setting. One can say that larger displacements in the experimental shear zones make them more comparable to faults than deformation bands. However, utilizing the ring-shear apparatus for deformation of highly-porous sand in a condition similar to shallow to medium burial depth and having the constrained thickness of the sample to the space between the rings, makes our comparison reasonable. In another word, the experimental shear zones have similar thickness to the single natural deformation bands.

We have identified variation in microstructure across experimental shear zones which are comparable to that seen in natural deformation bands (Paper 1). This variation has been previously addressed by a number of workers (e.g. Aydin, 1978; Aydin and Johnson, 1978, 1983; Gabrielsen and Aarland, 1990; Davis, 1999; Agung, 2004). The thin section microscopy studies of experimental shear zones produced by the ring-shear apparatus revealed the presence of three layers: a top layer, a central shear zone and a bottom layer (Paper 1).

The experimental shear zones were classified into two groups, *diffuse boundary shear zones* and *sharp boundary shear zones.* Diffuse boundary shear zone formed at low levels of normal stress and/or shear displacement, whereas sharp boundary shear zone formed at high normal stress and/or at high shear displacements. The sharp

boundary shear zone has not been previously reported from ring-shear experiments performed on sand or sandstone. The sharp boundary shear zones consist of margins of crushed and compacted grains around a more crushed and compacted central part which shows maximum reduction in particle size and significant porosity decrease. These shear zones are similar in microstructure to the classic deformation bands reported by Aydin (1978), which also have a compacted outer layer, but in which the deformation mechanism is mainly pore collapse.

The significant parameter that controls the transition from diffuse to sharp boundary shear zone is the transition of the grain fracturing mode from dominant flaking (e.g. Rawling and Goodwin, 2003; Paper 1) to dominant splitting. The transition occurs as a result of increasing the level of stress in the ring shear (similar to increasing the confining pressure in nature). This shift results in an increase in the D value (the power dimension of the grain size distribution fit). D has a good inverse correlation with the degree of cataclasis and grain size reduction (Blenkinsop, 1991; An & Sammis, 1994). However, the D values are relatively low in the experimental sharp boundary shear zone (D reaches a maximum of 1.5), suggesting that they have not reached the steady state particle size distribution (D~2.58).

Study of the effect of grain size on the frictional behavior of sand in the ring-shear experiments indicates that initial grain size has no influence on the deformation behavior at 5 MPa normal stresses (Paper 1; Kjelstad et al., 2002). On the other hand, Mair et al (2002) based on experiments from 5 MPa to 40 MPa stress, showed that grain characteristics, such as grain size distribution and roughness, have a clear effect on the frictional behavior of granular shear zones. In our ring-shear experiments, we have not investigated the effect of grain characteristics on experiments at more than 5 MPa.

Visual inspection of the experimental shear zones revealed that diffuse boundary shear zones are wider than sharp boundary ones (Paper 1). This is in agreement with results from numerical study of strain localization in granular material by for example Alsaleh (2006) and Alshibli et al. (2006). These studies showed that shear band thickness was found to decrease with increasing confining pressure. However, we have also demonstrated (Paper 4) that in natural deformation bands under constant confining pressure at the scale of a single deformation band, there is no simple relationship between thickness of the cataclastic deformation band and the degree of cataclasis within the band. The degree of cataclasis which is a factor of strain localization varies within Cataclastic deformation bands. Other factors that influence the thickness of deformation

bands during localization, such as grain characteristics, mineralogy, and initial porosity, need to be further investigated by both experimental and numerical studies. Besides, the research presented here shows there is a direct relationship between the thickness of the bands and the proportion of phyllosilicate (Paper 4).

Several of our studies have examined the spatial variation of deformation band microstructure, a topic which has received little or no attention in the literature. In this light, it is of interest that we show that a single band can change in thickness and microstructure over a short (mm-scale) distance. The variation in microstructure of the band implies that there is spatial variation in its petrophysical properties; this will be discussed further in the next sections.

A new type of deformation band has also been introduced through outcrop (Sinai, Egypt) and microscopy studies; here termed a *slipped deformation band* (Paper 2). Slipped deformation bands, characterized by a central slip surface, are different from conventional deformation bands (e.g. Aydin, 1978; Davatzes & Aydin 2003, Shipton & Cowie 2003, Johnson & Fossen in press). There is no compaction zone around the central part of the band in the slipped deformation bands from Sinai, Egypt. Therefore, in the slipped bands, the transition from the mildly-fractured background (host) rock to the band is sharp. We termed these individual tiny deformation bands "slipped deformation bands" because they can accumulate abundant shear strain and exhibit a slip surface. It is unclear how they form, but one plausible explanation can be found by the cam-cap model (e.g. Rudnicki & Rice, 1975; Rudnicki, 2002; Schultz & Siddharthan, 2005, Fossen et al., 2007; Holcomb et al., 2007). The background fracturing was probably induced during initial compaction as a result of overburden pressure, after which the deformation bands formed in a condition near simple shear-compaction in the field to the right-hand side of the cam-cap (Paper 2). The condition for localization of these bands is uncertain, but the parameters such as initial grain size and porosity should be significant.

Image processing technique for estimation of porosity and permeability

While microstructural variations along as well as across deformation bands are easily studied under the microscope, their internal permeability structure is difficult to assess by means of classical methods (e.g. permeability obtained from mini-permeameter and laboratory plug measurements). Mini-permeameter and laboratory plug measurements directly measure porosity and permeability for a band together with

its less deformed surrounding, whereas by application of image processing method, we are able to isolate the properties of only deformation band.

We have developed an image processing-based method which is applied on high resolution and -magnification images of thin sections. The image processing method applies statistical approaches such as spatial correlation functions to obtain porosity and specific surface area of the pore-grain interface from backscatter images of sandstone. In this method, we are able to catch the irregularities of the pore-grain interface, something that can not be done in other approaches such as process-based modeling by Bakke and Øren (1997), where they use an original BSE image of undeformed sandstone to obtain the grain size distribution and finally populate their model with a random spherical grain size distribution and use clay and cement to reach to the approximate angularity of the real grains.

We have used a similar approach to what Blair et al. (1996) used, but they applied that method on images from 2D thin sections of undeformed sandstone, which had simpler pore size distribution compared to deformation bands. Later on Keehm et al. (2004); and White et al. (2006) calculated effective permeability of compaction bands in sandstone through stochastic 3D porous media reconstruction and flow simulation using the Lattice Boltzman method. They used the calculated two-point correlation function of the 2D images (similar to what we calculate) to reconstruct their 3D model. Furthermore, they modeled compaction bands which lack cataclasis. Our research indicates that in order to capture the complex microgeometry of cataclastic deformation bands, we need to take several high magnification images that cover the entire width of the band and use these images to calculate an average specific surface area for the band.

We have resolved the problem of the sensitivity of specific surface area estimation to the resolution of the image (e.g. Keehm et al., 2004) by using high resolution images that provide insight into complex microgeometries. Implementation of image processing methods for deformation bands enables us to map out the variation in porosity and permeability across as well as along tiny deformation bands. Moreover, by applying this method on thin sections of different orientation, we can map out the properties of the band in different orientations (Papers 3 and 4).

Assessing the petrophysical properties of deformation bands

The macroscopic anisotropy across deformation bands and their influence on the petrophysical characteristics of petroleum reservoirs have been addressed before by

among others Antonellini and Aydin (1994), Sigda et al. (1999) and Shipton et al. (2002). The microscopic anisotropy in the properties along a deformation band has been described in Paper 3 of this thesis. Comparison of porosity and permeability estimates from image processing with direct measurements of porosity and permeability from plugs is not straightforward, as the scale of measurement is different. Comparison of our estimated values to lab-measured data shows that the estimated values are always lower than the lab-measured values. We ascribe this difference to the scale limitation (2.54 cm/1 inch) inherent when plug-sized samples are used to measure the properties of millimeter-wide bands.

Our results from image processing show that both porosity and permeability decrease in the studied cataclastic bands compare to the host rock, but the permeability reduction is substantial (up to four orders of magnitude). This is in agreement with lab-measured data (Papers 2, 3) and consistent with the studied cataclastic deformation bands exhibiting more grain crushing than compaction, reducing the grain size and increasing the specific surface area of the pore-grain interface. Hence, the permeability values decrease. In addition, the studied dissolution band (Paper 4) showed up to four orders of magnitude reduction in permeability. This can be also explained by increased specific surface area of the pore-grain interface as a consequence of touching grains.

This study describes new aspects of anisotropy in petrophysical properties such as porosity and permeability induced by deformation bands in the deformed sandstones in microscale. By using our developed image processing method, we have obtained several porosity and permeability measurements for a single band in one thin section, identifying permeability changes up to two orders of magnitude along the band (Paper 4). These changes are related to the variation in microstructure and grain size along the band, as described in the first section of this discussion. We suggest that lateral variations in porosity and permeability documented through image analyses presented in Papers 3 and 4 can explain at least some of the scatter in the porosity and permeability data reported in the literature.

Implications for fluid flow

The effect of deformation bands on fluid flow in a petroleum reservoir depends on the type of deformation band, which is linked to (i) their deformation mechanisms, (ii) their physical properties, and more importantly (iii) the variation of properties such as porosity and permeability across as well as along the bands. Our observations show that

cataclastic deformation bands can reduce absolute permeability values up to four orders of magnitude (Papers 3 and 4). In this sense, they are considered to be important for reservoir management, particularly where they appear in clusters in the damage zones of large faults. On the other hand, rapid spatial variation in properties along bands (Paper 4) implies that deformation bands may rarely be significant pressure barriers and thus probably do not contribute significantly to the sealing capacity of faults (e.g. Harper and Lundin, 1997). In the case of phyllosilicate bands, which are abundant in North Sea petroleum reservoirs, predicting their thickness and continuity is essential for planning oil and gas fields production (Fisher and Knipe, 2001; Hesthammer and Fossen, 2001; Ogilvie and Glover, 2001). Phyllosilicate bands can potentially seal hydrocarbon columns with heights of several hundred metres (Gibson, 1998). During reservoir development, it is important to consider the influence of diagenesis on the petrophysical characteristics of the reservoir, particularly concerning the effect of quartz cement in deep reservoir horizons (more than about 2 km). Finally, the effect of deformation bands on fluid flow in reservoirs depends on their spatial distributions and their abundance, which is beyond the scope of the presented work.

Limitations related to the current study

Research is perhaps always compromised by limitations of some kind, and this research is not an exception. There are limitations inherent both in the instruments applied and in the methods that have been used in this study. The limitations that are related to the individual steps of this research are as follows:

- Constraints imposed by the ring-shear apparatus limited the experiments to (i) a predefined shear surface, and (ii) higher shear displacement than it is required for the formation of deformation bands. Taken together, these make the comparison of experimental shear zones to natural deformation bands less straight forward; this is discussed further in Paper 1.

- The time-consuming segmentation process for grain size analysis and also the image processing for porosity, permeability estimations rely on the quality of the obtained binary image and the level of threshold that a backscatter image is assigned to (Papers 3, 4). A quality check should be done during binarizing images by comparing them to the original BSE images.

- In the Kozney-Carman relation, the constant *c* is considered to be equal to 2 for the pores with circular cross-sections. In order to calculate the formation factor we used an exponential relationship between porosity and formation factor (Archie, 1942). The results could be slightly different if we could measure the formation factors for the studied deformation bands (Paper 3).

Suggestions for future work

- Further investigation is also needed on the initiation and development of deformation bands in a wide range of sandstones with different mineralogy, initial grain size, and porosity.
- The presence of cement at the time of deformation affects the deformation processes and resulting deformation-band properties (e.g. Trent, 1989; Yin and Dvorkin, 1994). The effect of quartz cement on cataclasis and the significance of phyllosilicates on the initiation of quartz cement should be studied further.
- In order to better simulate the natural formation of deformation bands, performing experiments with fluid in the pore spaces (that is, undrained) is recommended. At low confining pressures and in the presence of fluids, minerals such as feldspar are deformed by chemical alteration rather than physical deformation.
- In order to document the detailed microstructure of deformation bands, especially when one is trying to build a 3D geological model, we suggest making thin sections at least in two perpendicular directions.
- High resolution X-ray microtomography can be used to characterize the 3D microgeometry of deformation bands if their resolution is sufficient for capturing the complex microgeometry of cataclastic bands. This type of study may add to our knowledge about deformation bands.
- In the case of slipped deformation bands (Paper 2) more field work is needed to find out whether this kind of band is common in other similar geological settings, and in sandstones with similar petrophysical properties. Besides, understanding the mechanism of formation of slipped bands requires theoretical work, triaxial analogue modeling, and developing their cam-cap model accordingly. The initial material properties, such as grain size and porosity, must be considered in such studies.

References

Agung, M. W., Sassa, K., Fukuoka, H., Wang, G., 2004. Evolution of shear zone structure in undrained ring-shear tests. Landslides 1, 101-112.

Antonellini, M. and Aydin, A., 1994. Effect of faulting on fluid flow in porous sandstones: petrophysical properties, AAPG Bull., 78, 355-377.

Archie, G. E., 1942. The electrical resistivity log as an aid in determining some reservoir characteristics. Trans. Am. Ins. Min. Metall. Pet. Eng., 146, 54-62.

Aydin, A., 1978. Small faults formed as deformation bands in sandstone. Pure and Applied Geophysics 116, 913-930.

Aydin, A. & Johnson, A.M., 1978; Development of faultz as zones of deformation bands and slip surfaces in sandstone. Pure and Applied Geophysics 116, 931-942.

Aydin, A. & Johnson, A. M., 1983. Analysis of faulting in porous sandstones, Journal of Structural Geology 5, 1, 19-31.

Davis, G. H., 1999. Structural geology of the Colorado Plateau region of Southern Utah. Geological Society of America, Special Papres, 342.

Davatzes, N. C., Aydin, A., 2003. Overprinting faulting mechanisms in high porosity sandstones of SE Utah. Journal of Structural Geology, 25, 1795-1813.

Fisher , Q. J. & Knipe, R. J., 2001. The permeability of faults within siliciclastic petroleum reservoirs of the North Sea and Norwegian Continental Shelf. Marine and Petroleum Geology, 18, 1063-1081.

Fossen, H., Schultz, R. A., Mair, K. and Shipton, Z., 2007. Deformation bands in sandstones- a review, Journal of Geological Society, London, 164, 755-769.

Gabrielsen, R. H. & Aarland, R. K., 1990. Characteristics of pre-syn-consolidation structures and tectonic joints and microfaults in fine- to medium-grained sandstones. Rock Joints. Balkema, Amsterdam, 45-50.

Gibson, R. G., 1998. Physical character and fluid-flow properties of sandstone-drived fault zone. Geological Society London, Special Publication 127, 83-97.

Harper, T. R. & Lundin, E. R., 1997. Fault seal analysis: reducing our dependence on empiricism. In: Möller-Pedersen, P. & Koestler, A. G. (eds) Hydrocarbon seals-Importance for Exploration and Production. Norwegian Petroleum Society, Special Publication 7, 149-165.

Hesthammer, J. & Fossen, H., 2001. Structural core analysis from the Gullfaks area, Northern North Sea. Marine and Petroleum Geology 18, 411-439.

Johansen, T. E. S. & Fossen, H. 2008: Internal deformation of fault damage zones in interbedded siliciclastic rocks. Geological Society, London, Special Publicatio, in press.

Ogilvie, S. R., Glover, P. W. J., 2001. The petrophysical properties of deformation bands in relation to their microstructure. Earth and Planetary Science Letters 193, 129-142.

Shipton, Z. K., Evans, J. P., Robeson, K. R., Forster, C: B., Snelgrove, S., 2002. Structural heterogeneity and permeability in eolian sandstone: Implications for subsurface modelling of faults. AAPG Bull. 86, 863-883.

Shipton, Z. K. & Cowie, P. A., 2003. A conceptual model for the origin of fault damage zone structures in high porosity sandstone. Journal of structural Geology, 25, 333-345.

Sigda, J. M., Goodwin, L. B., Mozely, P. S. & Wilson, J. L., 1999. Permeability alteration on small displacement faults in poorly lithified sediments: Rio Grande Rift, Central New Mexico. In: Faults and Subsurface Fluid Flow in the Shallow Crust (edited by Hanberg, W. C., Mozely, P. S., Moore, C. J., Goodwin, L. B.. Geophysical Monograph 113. American Geophysical Union, Washington DC, 51-68.

Trent, B. C., 1989. Numerical simulation of wave propagation through cemented granular material, in AMD-101, Wave Propagation in Granular Media, eds. D. Karamanlidis and R. B. Stout, 9-15.

Yin, H. & Dvorkin, J., 1994. Strenght of cemented grains, Geophysical Research Letters 21, 10, 903-906.

Appendix

```
% This program includes a series of functions that estimate the
%porosity and specific surface area from microscopic images of thin
%sections using statistical physics.

% Note: The authors assumes no responsibility whatsoever for the use of
% the program by other parties, and makes no guarantees, about its
%quality, or any other characteristic.

% Terms of use of this program

% 1) Use of this program by any for-profit commercial organization is
%expressly forbidden unless said organization is a Fault Facies Project
%sponsor.

% 2) A Fault Facies Project sponsor may use this program under the
%terms of the Fault Facies Project Sponsorship agreement.

% 3) A student or employee of a non-profit educational institution may
%use this program subject to the following terms and conditions:
% - this program is for research purposes only.
% - including it or any portion of it, in any software that will be
%resold is expressly forbidden.
% - transferring the program in any form to a commercial firm or any
%other for-profit organization is expressly forbidden.

% (1) The 1st step is reading thin section images into MATLAB.

 I=imread('image file'); %Image matrix has M rows and N columns
%(i=1,2,...M, j=1,2,...N).

 figure, imagesc(I),colormap(gray(256)), grid on;

% By using 'imagesc' function to display the thin section the data is
%scaled to use the full colormap.

figure,imshow(I),grid on; axis on
% imshow displays the grayscale image 'I' without scaling the data.

%========================================================================
% (2): The 2nd step is to choose part of the image for further work. By
% using 'grid on' and 'axis on' commands in the display functions, we
%can choose the matrix indices of the four corners forming the selected
%area inside the image 'I'.
% The following drawing shows the matrix range for the initial image
'I' %and the cropped image inside the initial image.
%
%        j=1                        j=N
%    i=1  |------------------------|
%         |                        |
%         |  |-----------------|   |
%         |  |                 |   |
%         |  |-----------------|   |
%         |                        |
%   i=M   |------------------------|


% I=I(first row of cropped image: last row of the cropped image, first
%column of cropped image: last column of the cropped image);
```

```
%
=========================================================================
% (3) The 3rd step is to estimate the threshold. There are two ways %to
perform this:
% (3-A) Otsu method (MATLAB built in function)

threshold=graythresh(I);

% graythresh computes a global threshold that can be used to convert
%the image 'I' to a binary image. The resultant value or level is a
%normalized intensity value that lies in the range [0, 1].
% GRAYTHRESH uses Otsu's method, which chooses the threshold to %
%minimize the intraclass variance of the threshold black and
% white pixels.

% (3-B) The second way is to create the data histogram, display it and
%choose the threshold value by visual inspection of the data histogram.
%The numbers of occurrences of the values between 0 and 255 ('counts')
%are displayed. The length of 'counts' is the same length of colormap
%in this case 256.

imhist(I)
[counts,x]=imhist(I);figure, bar(x,counts),

%=========================================================================
% (4) The 4th step is making binary using the estimated threshold
%value.

 bw=im2bw(I, threshold);

% The function is MATLAB build in function that Convert image to binary
%image by thresholding.
% The output binary image BW has values of 1 (white) for all
% pixels in the input image with luminance greater than LEVEL and 0
%(black) for all other pixels.

 figure,imagesc(bw),colormap(gray), grid on % scaled display to
%colormap range
 figure, imshow(bw), grid on, axis on       % Dispaly without scaling

%=========================================================================
% (5) The 5th step is to change the image to a square matrix in case if
%it is not, We select parts of the image that has as less as possible
% broken grains at the edge of the image. This stage is only necessary
%if we calculate the two point correlation function using function
%'xcorr2' (step 8).

     I2=bw(1:m,1:m);

% m is the number of rows and also columns that is selected from the
%image.

  figure, imagesc(I2),colormap(gray), grid on  % scaled display to
%colormap range
  figure, imshow(bw), grid on, axis on       % Dispaly without scaling

%=========================================================================
% (6) The 6th step is reversing the negative image to positive image it
%means pore space from black (0) to white (1). The indicator function
%or phase function or characteristic function is 1 for pores and 0 for
%grains.
```

```
 I3=ones(size(I2)); tes=find(bw); I3(tes)=0; %If we apply the 5th stage
%then here bw will be replaced by I2.
 figure,imagesc(I3),colormap(gray),grid on  % scaled display to
%colormap range
 figure, imshow(I3), grid on, axis on       % Dispaly without scaling

%=========================================================================
% (7) The 7th step is to calculate the one point correlation function
%that is the porosity. The denominator is the product of pixel numbers
% in both directions.


        phi=length(find(I3))/(M*N)
        % MxN is the ranke of I3.

%=========================================================================

% (8) The 8th step is to calculate the two-point correlation function.
%     We have two methods to do this.
% 8-A) First the function we have written called tpcf.m. The function
%  is run as follows:
       S2=tpcf(I3);

% The function detail is given below:
       function s2=tpcf(I3)
% This function calculate the two-point correlation function
%(that is a joint probability function) using the binary image with a
% certain pixel size.

s2(1,1)=length(find(I3))/(length(I3));
s2(1,1);
a=length(I3(:,1));

    b=length(I3(1,:));
    c=a/b;

 for m=3;
   i=1:length(I3(:,1)-m;
  end
    for n=3;
   j=1:length(I3(1,:))-n;
    end
for i=1:length(I3(:,1))-m;
for j=1:length(I3(1,:))-n;

x=I3(i,j);
save x
y=I3(i+m,j+n);
save y
%data(1:m,1:n).test=[x,y]
test=x.*y;
save test
test2=sum(test);
test3=test2/(length(I3));
save test3
%save test
s2(m,n)=sum((I3(i,j)*I3(i+m,j+n))/((a-m)*(b-n)));
 end
```

```
end
       end


% 8-B) The second method is to use the MATLAB built in function called
%  xcorr2.
       test4=xcorr2(I3);
% The only difference is that in the second method we should use two
% more step as follows:
% sub-step 1: Selection of the positive lag of the autocorrelation
function:
       I4=(test4(length(I3(:,1)):end,length(I3(1,:)):end));
       figure,imagesc(I4), grid on  % scaled display to colormap range
       figure, imshow(I4), grid on, axis on     % Dispaly without
%scaling

% sub-step 2: Normalization of the results:
       I4=I4/(length(I3));
       figure, imagesc(I4),grid on % scaled display to colormap range
       figure, imshow(I4), grid on, axis on   % Dispaly without scaling

%=========================================================================
% (9) The 9th step is a main step to convert the calculated two-point
%  correlation function from the Cartesian coordinate system to a
%radial system and then taking average along the certain radiuses.
% The reason for this is to be able to use the spatial correlation data
% derived from 2D images for 3D purposes.
% We have written a function called average.m to do this that is run as
%   follows:

      [test3]=average(I4), figure, plot(test3), grid on
% test3 is a vector that represents the mean values of two point
% correlation function along different radiuses.

function [test3]=average(I4)
% This function is planned to map the two-point correlation function
%from a Cartesian coordinate system to polar coordinate system and then
%taking average along fixed radiuses.
% The input to the function is just the normalized two-point
%correlation function (output of the 8th staep). The output is a vector
%that represents the average values of two-point correlation function
%along the fixed radiuses.

X=1:length(I4(:,1));
Y=1:length(I4(1,:));
test3=[1:length(I4(:,1))/2];
test3=test3';
test3(1)=I4(1,1);
%=====================================
[x,y]=meshgrid([1:length(I4(:,1))],[1:length(I4(1,:))]);
for k=2:300;
   l=1:2*k-1;
  v(l)=(pi*l)/(4.*(k));
  XI=k*cos(v);
  YI=k*sin(v);
    s=[XI; YI];
 Z1=interp2(x,y,I4,s(1,2:end-1),s(2,2:end-1)); % 2D interpolation has
been used.
 a=sum(Z1);
 test3(k)=(1/(2.*k+1))*sum(I4(k+1,1)+I4(1,k+1)+a+Z1(1)+Z1(end));
end
```

```
%========================================================================
% (10)to set the scale, and caluculate the slope.

FX(1)=test3(2)-test3(1)
scale=(the scale in main picture)/(number of pixels of the scale bar)
% For example scale bar is 100 micromillimeter and the length of bar in
% pixels are 80 then scale=100/80=1.25

FX(1)=FX(1)./scale

% Now we have the quantity that can be used to calculate specific
%surface area.


     FX(1) = -(specific surface area)/4


     FX(1)=-(specific surface area)/pi
```